Visual Simulation of Opal Using Voronoi Tessellation and Ewald Construction

February 2025

Soma Yokota

Academic Year 2024

Visual Simulation of Opal Using Voronoi Tessellation and Ewald Construction

A dissertation submitted
in partial fulfillment of the requirements for the degree of
Doctor of Philosophy in Engineering

Keio University
Graduate School of Science and Technology
School of Science for Open and Environmental Systems
Center for Information and Computer Science

February 2025

Soma Yokota

Dissertation Abstract

Visual Simulation of Opal Using Voronoi Tessellation and Ewald Construction

Used as a gemstone, opal exhibits an optical phenomenon known as "play of color," a type of structural color caused by the fine regular structure within the opal. Because of this optical property, opal has been used as jewelry since ancient times and has been valued as a cultural treasure from both historical and artistic perspectives. Opal is also classified as a material called colloidal crystal, and this property in particular gives it its high engineering value, with potential applications in quantum information processing and structural color displays. Thus, opal is an important material in the fields of industry, the humanities, and the natural sciences.

In contrast, few studies have focused on realistic representations of representing opal using computer graphics. Opal consists of numerous aggregates of colloids, with diameters on the scale of several hundred nanometers, resulting in an extremely complex internal structure. However, opals used for jewelry are usually several tens of millimeters in size, making their scale roughly 10^5 times larger than individual colloidal particles. This significant size disparity poses a challenge, as modeling the stacking information of each colloidal particle is impractical on current computers due to memory limitations. Thus, a method for modeling the internal structure at an appropriate scale is required. In addition, an efficient rendering approach is required for accurate tracking of the complex diffraction of visible light within the opal.

This study investigates the physical properties of opals, identifies four key factors that contribute to their visual characteristics, and proposes a method for the realistic visual simulation of opals. First, the internal structure of opal is represented using a three-dimensional Voronoi diagram, where both a signed distance function and a voxel-based approach are utilized to represent the Voronoi diagram, with a comparison between the advantages of each method. Next, spectral rendering using Monte Carlo path tracing is performed to obtain images of these models. A method inspired by Ewald construction from X-ray crystallography is also proposed to compute diffraction.

This study demonstrates that the combination of the seven parameter values enables the visual simulation of a wide variety of opals. The parameter values of real opal were applied, and it was shown that it is possible to reproduce play of color in accordance with a real opal.

Keywords

Computer graphics; visual simulation; appearance modeling; structural color; opal.

Acknowledgments

First and foremost, I would like to express my sincere gratitude to my primary advisor, Prof. Issei Fujishiro. The successful completion of this doctoral dissertation would not have been possible without his unwavering guidance and generous support. His insightful advice on formulating research plans, meticulous feedback on my writing, and precise guidance on the appropriate timing for publishing research findings greatly contributed to my ability to produce significant research outcomes, receive awards, and enhance my academic skills over the past four years in his laboratory. He also gave me the opportunity to participate in various activities, such as educational activities, internships, and student volunteer programs, which allowed me to gain a wide range of experience. Furthermore, under his supervision, I was fortunate to connect with many researchers and professionals who are active in the field of computer graphics, which provided me with meaningful opportunities for academic and professional development.

I am deeply grateful to Prof. Hideo Saito, who emphasized the importance of establishing guidelines to make the results of this research accessible to a broader range of users; Prof. Yuta Sugiura, who offered insightful discussions on the potential applications of this research, including the fabrication of artificial opals; and Prof. Kei Iwasaki, provided expert advice on the rendering aspects of this study, for their invaluable comments and guidance, which greatly contributed to improving this dissertation. Their thoughtful suggestions and expertise have been instrumental in enhancing the quality and scope of this work.

I would like to extend my gratitude to Mr. Yuichiro Okuyama, Executive Director of the Yamanashi Gem Museum; Prof. Hiroaki Imai of Department of Applied Chemistry, Faculty of Science and Technology, Keio University; and Dr. Koichi Momma, Researcher at the National Museum of Nature and Science. As experts in fields distinct from computer graphics, they graciously provided valuable reviews and insightful feedback to enhance the quality of this research.

I am also deeply grateful to Polyphony Digital Inc., where I worked part-time for over a year. In particular, I would like to thank Mr. Kentaro Suzuki and Mr. Hajime Uchimura, who mentored me throughout this period. The weekly discussions on state-of-the-art research papers at the company were intellectually stimulating and served as a strong

motivator for advancing my research. Moreover, working closely with professionals at the forefront of the gaming industry provided me with invaluable experiences.

I extend my heartfelt appreciation to all members of the Fujishiro Laboratory for their support in both daily life and research discussions. I would especially like to acknowledge Dr. Akinori Ishitobi for his continuous and constructive advice that greatly improved my research since I joined the laboratory. I am also grateful to Dr. Masaru Ohkawara for inspiring my interest in photorealistic rendering and to Shumpei Sugita for his invaluable guidance on rendering implementation. My sincere thanks also go to Yuki Nishidate for being both a supportive peer and a good friend, offering advice on research activities and future career paths. In addition, I greatly appreciate Chinatsu Yoshida for her significant support in managing team activities within the laboratory.

Lastly, I would like to express my deepest gratitude to my family. I was able to complete my graduate studies in good health thanks to their unwavering support. I am sincerely thankful for their understanding and continuous encouragement throughout my academic journey.

To all of you, I offer my heartfelt appreciation.

February 12, 2025

Contents

List of Figures

List of Tables

Chapter 1

Introduction

This chapter serves as an introduction to the dissertation, outlining its scope, objectives, and structure. **Sections 1.1** and **1.2** provide the background of the study, while **Secs. 1.3** and **1.4** outline the objectives and contributions of the study. Finally, **Sec. 1.5** presents the structure of the dissertation.

1.1 Visual Simulation

Visual simulation is one of the most fundamental and important fields in computer graphics (CG), and it aims to represent natural phenomena in a visually plausible manner. Unlike numerically accurate simulations, used primarily in engineering, visual simulation is tailored for applications in the filmmaking and gaming industries. First, it is characterized by the importance of fast feedback to the user. For example, the rendering equation proposed by Kajiya [48] represents optical phenomena as integral equations based on geometric optics. Although light inherently exhibits wave-like properties, from the perspective of obtaining visually plausible images, geometric optics offers an effective scale for approximating and reproducing optical phenomena in everyday life. This approach has become a standard in the field of CG for obtaining photorealistic images. Another defining feature of visual simulation is its emphasis on robustness. Stam's seminal work [80] sets the foundational direction for fluid simulation in CG. Fluid behavior is represented as a continuum by the Navier–Stokes equations. This paper introduces the semi-Lagrangian method for numerically updating the equation values, allowing for stable solutions, even with large time steps. This method not only provides quick user feedback, but it also maintains robustness under extreme conditions that would not occur in reality. Stam's work remains highly cited as the cornerstone of fluid simulation in CG.

With the growing interest in differentiable rendering [69], this technology has been advancing rapidly. As a result, visual simulation is expected to be applied beyond entertainment to real-world domains, such as spatial design in architecture and fabrication. With the advent of differentiable rendering, the importance of realistic rendering methods in visual simulation is intensifying.

The pursuit of rendering methods in CG that are indistinguishable from photographs requires the modeling of natural phenomena at appropriate scales, while ensuring visual plausibility. To enable computationally complex natural phenomena while satisfying the demands of visual simulation, models are often constructed using a combination of three principal approaches: physical, phenomenological, and artificial [55]. The physical approach represents phenomena using mathematical expressions derived from physical laws; the phenomenological approach relies on actual measurements to represent the model, and the artificial approach uses noise or procedural models to create repre-

sentations artificially. To illustrate the phenomenological and artificial approaches, cloth rendering serves as an example. Sattler et al. employed instrumentation to capture the bidirectional texture function of a cloth [73], representing both a data-driven and phenomenological approach. Conversely, Zhao et al. proposed a method that fits procedural fiber representations to fiber data acquired through CT scanning [102]. This method exemplifies a phenomenological approach via the utilization of real-world measurement data, as well as an artificial approach via the procedural generation of fibers.

It is important to note that the appropriate scale for modeling natural phenomena varies depending on the required application. In cloth rendering, beyond the data acquisition methods described above, determining the scale at which to represent the data is critical, and various approaches have been proposed. These include explicit modeling of fiber geometry at the yarn level [30], treating fabric as participating media [41], and abstracting fabric as a surface represented by a mesh with geometric details and approximated using a shading model [92]. Explicit modeling provides a realistic appearance, particularly when observed at close range, but it requires significant memory to store the model, and simulating its optical properties requires a high computational load. In contrast, abstract modeling reduces computational requirements and memory usage but may result in unnatural visual artifacts when viewed closely. This highlights the absence of a universal solution for approximating natural phenomena in visual simulation. Instead, different methods should be applied based on the specific requirements of the intended application.

1.2 Visual Simulation of Opal

Used as gemstones, opals exhibit a shimmering iridescent pattern within, an optical phenomenon is known as “play of color.” **Figure 1.1** shows images of an actual opal that demonstrates this phenomenon. Opals are composed of stacked colloids that resemble a polycrystalline structure, and this structure is referred to as a colloidal polycrystalline. Because a colloidal polycrystalline has optical properties that diffract visible light, research and development are being conducted in the field of materials engineering for practical applications, such as quantum information processing [51] and electrophoretic color displays [2].

Opals have been used as jewelry since ancient times and are highly valuable, not only in industrial contexts but also as cultural assets from historical and artistic viewpoints. Realistic visual simulations of opals are useful for preserving digital archives of cultural properties; consequently, the realistic visual simulation of the optical phenomena inherent to opals is important across diverse fields, including entertainment, natural science, industry, and the humanities.

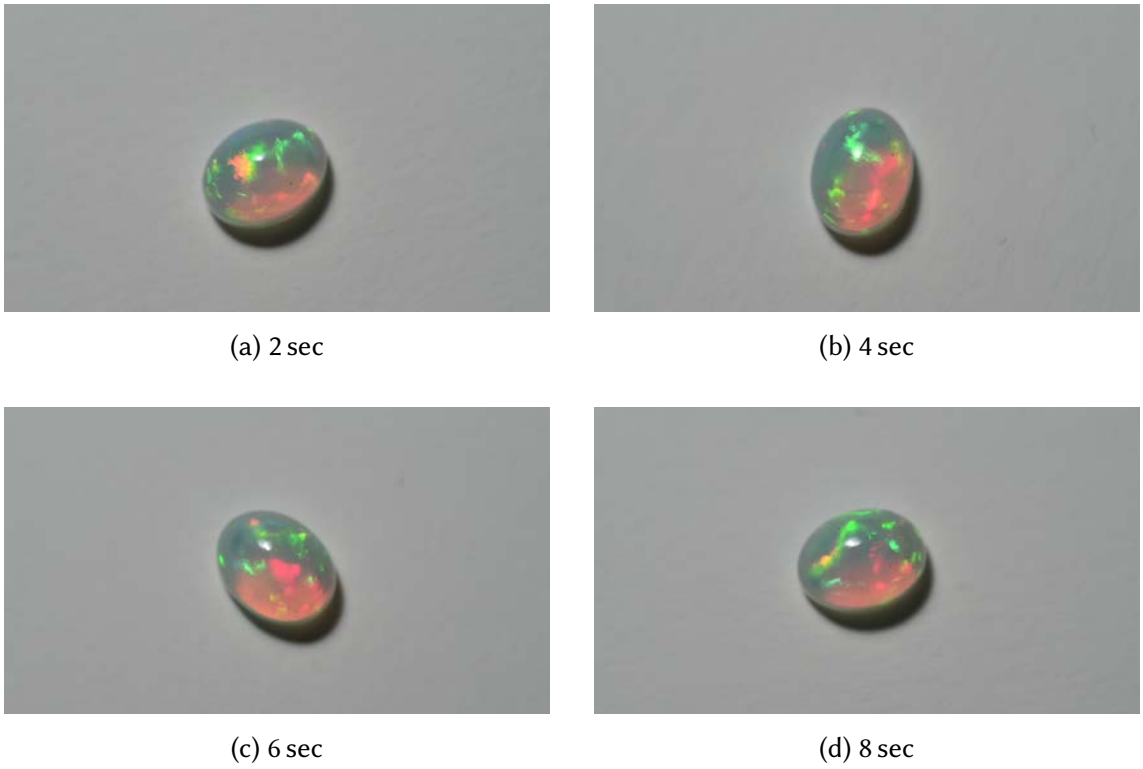

(a) 2 sec (b) 4 sec

(c) 6 sec (d) 8 sec

Fig. 1.1 A real opal. Courtesy of Yamanashi Gem Museum. The opal, placed on a sheet of paper, was illuminated from above using a spotlight. A video was captured while the pedestal holding the opal was rotated. The sample predominantly displays green play of color, but some yellow or orange can be seen from specific angles. Note that the internal pattern of the same sample changes in complexity depending on the viewpoint

On the other hand, due to the complexity of its internal structure, a method to represent opal by computer graphics has not yet been established. Opal is a material classified as amorphous, so it does not have a regular atomic arrangement. As a result, a realistic visual simulation of opal cannot be achieved by merely computing diffraction occurring at the boundary between material and air, as in Stam's method [79]. The smallest unit of an opal is a colloid with a grain size of only a few hundred nanometers. Considering that opals used in jewelry are approximately 10 mm in size, modeling the stacking arrangement of individual particles is infeasible with today's computer memory capabilities. Furthermore, the optical phenomena within opals, such as light diffraction, scattering, and absorption, introduce significant computing demands.

To address these challenges, it is essential to develop a model that simplifies the internal structure to the extent that the visual characteristics of play of color are not retained and that performs efficient optical computations.

1.3 Research Purpose and Objectives

This study aims to propose a method for a photorealistic visual simulation of opals grounded in their physical characteristics. To achieve this, the physical properties of real opals are first clarified through a combination of archival research and direct observation. Based on the information obtained, a method for representing and rendering the internal structure of opals for visual simulation is introduced.

Specifically, the complex internal structure of opal is modeled using three-dimensional (3D) Voronoi tessellation, and the output image is obtained thorough spectral rendering [14] using the path tracing method [48]. The study demonstrates that the geometric properties of the Voronoi diagram can be used to achieve highly efficient information compression to determine the complex internal structure of an opal. In addition, it is shown that the weighted Voronoi diagram enables intuitive modeling of the polycrystalline growth direction.

To represent the structural color of colloidal crystals within the internal structure models, a local illumination model is proposed. This approach enables the computation of ray diffraction directions on the fly by applying the Ewald construction used in X-ray structural analysis to the path tracing method. Furthermore, an intuitive method for modeling the base color of opal is proposed, using a combination of three physics-based parameters.

1.4 Contributions

The contributions of this study are summarized in three key points:

1. **Research and organization of physical background of opal.** The the physical characteristics necessary for the visual simulation of opals were identified and organized. This clarified the foundational elements required to represent the optical properties unique to opals.
2. **Proposal for crystallography-based internal structure model.** By employing a Voronoi diagram, the study demonstrates that the complex internal structure of opals can be represented at a scale suitable for visual simulation.
3. **Proposal for local illumination model of 3D structure of colloidal polycrystalline.** The study introduces a method to simulate light diffraction in a 3D regular structure, adapting the Ewald construction from X-ray structural analysis for use within a path tracing framework.

The first contribution was published as [M1], the second as [M1, R1, R2, R3], and the third as [M2, R4].

1.5 Dissertation Structure

The remainder of this dissertation is organized as follows:

Chapter 2: Related Work

This chapter reviews advancements in photorealistic image synthesis within CG, followed by an introduction to research in three key areas: visual simulation of gemstones, aggregate materials, and structural colors. It concludes by situating the current study within these research domains.

Chapter 3: Research Overview

This chapter describes the internal structure of real opals and the principles behind their play of color. Observations made using a digital microscope are reported, and the elements necessary for the visual simulation of opals are discussed based on these findings.

Chapter 4: Modeling

This chapter describes a method for modeling the internal structure of opals using Voronoi diagrams. Two approaches are proposed: one representing the Voronoi diagram using only sites and another storing the diagram in voxel form, with a comparison of their advantages. In addition, the chapter outlines a method for modeling the base color of an opal.

Chapter 5: Rendering

This chapter explains the method of global illumination computation employed in the study and highlights the significance of spectral rendering. It details the rendering method used to represent play of color (described in **Chap. 4**) for the internal structure model (defined in **Chap. 3**). Methods for rendering light scattering and absorption related to the base color of opals are also discussed.

Chapter 6: Results and Discussions

This chapter presents the results of visual simulations using the proposed method and confirms that play of color is realized by the internal structure model and rendering approach proposed in this study. The validity of these results and the direction of the research are discussed. Future prospects of this research are also explored.

Chapter 7: Conclusion

This chapter provides a summary and concludes the study.

Chapter 2

Related Work

This study investigates a realistic rendering method of opals using CG. To achieve this, the study reviews the development of realistic image synthesis methods in CG and then reviews how materials related to opals have been simulated.

Section 2.1 introduces techniques for obtaining realistic images in CG. **Sections 2.2**, **2.3**, and **2.4** review related works from the perspective of three of opal's characteristics: as a gemstone, as an aggregate material, and as having structural color, in that order. Further, **Sec. 2.5** places the proposed method within the context of prior studies.

2.1 Approaches to Realistic Image Synthesis

CG involves defining a shape on a computer and then rendering it to obtain an output image. Realistic images are achieved by performing global illumination computations, which simulate the propagation of light within a scene according to physical laws. The radiosity method [28, 66] computes global illumination by analyzing the energy distribution of light emitted by light sources using a thermodynamic framework. Kajiya [48] unified previously attempted theories for global illumination by proposing the rendering equation, an integral equation that models optical phenomena using geometric optics. In the same work, based on ray tracing using the Monte Carlo method [11], Kajiya proposed the path tracing method, which computes global illumination effects by tracing rays with the Monte Carlo method. Other notable techniques include the Metropolis light transport method [87], which employs Markov chain Monte Carlo sampling for path generation, and photon mapping [44], where photons are emitted from light sources, tracked, and later collected from the viewpoint to render the image.

More recently, advancements in radiance field representations have been used for generating realistic images. These methods include representing radiance fields with multilayer perceptrons [60] or using sets of 3D Gaussians and spherical harmonics [50]. Such approaches enable rendering of realistic images from a specific viewpoint when provided with real-world image datasets. However, because the focus of this study is on visual simulation, these methods for generating novel view synthesis and 3D reconstructions fall outside its scope.

Polygons are the most commonly used primitive in CG for defining shapes. However, because objects in the real world have various shapes at various scales, representing all shapes explicitly with polygonal meshes is not always optimal. In general, there are a variety of representation formats in CG, depending on the scale of the object to be represented. For example, bump mapping [8] uses textures to represent an uneven surface and is suitable for reproducing unevenness on a scale of 0.1 to several tens of millimeters. Finer-scale irregularities are often represented statistically, as in the bidirectional

reflectance distribution function (BRDF) [65]. For example, microfacet theory [86] models the scattering distribution of light on a set of small irregular surfaces with specular reflection properties, within the constraints of the geometric optics. There is also microflake theory [41], which describes the distribution of small objects in space in terms of volume. In the visual simulation of opal, it is necessary to represent the shape at an appropriate scale based on these previous studies.

2.2 Visual Simulation of Gemstones

As introduced in **Chap. 1**, the distinct play of color observed in opals makes them a popular choice as gemstones. However, the realistic visual simulation of gemstones has been a longstanding research challenge in CG.

When rendering single-crystal gemstones, dispersion [84] and polarization [94] play crucial roles due to their visual impact. For instance, Guy and Soler [33] interactively simulated single-crystal gemstones in consideration of these phenomena, as well as of absorption and birefringence. Though this method was applied to relatively simple facet-cut shapes, Hui et al. [38] extended the approach to incorporate more complex geometries. Even further, some studies have been able to reproduce the optical phenomena observed in specific minerals, including asterism or chatoyancy [100], birefringence in uniaxial crystals like calcite [90], aventurescence [89] found in sunstone and aventurine, and labradorescence [91] in labradorite.

Regarding opal simulation, Imura et al. [40] attempted to render opals; however, despite successfully reproducing play of color, the physical basis for modeling and rendering remains ambiguous in the paper. In addition, the gaps in this opal model are represented as being tens of micrometers in size, whereas the actual gaps in real opals measure several hundred nanometers, leading to some deviations from the real structure. Meanwhile, Tabuchi and Kawai [83] modeled the internal structure of opals using hand-drawn vector images. This study takes an artificial approach to the internal structure, but while the rendering results achieved appear visually plausible, the method lacks physical grounding.

2.3 Rendering Aggregate Materials

Opal is formed by the aggregation of numerous colloidal grains of a visible size. In general, explicitly modeling each grain of an aggregate demands substantial memory, and the complex paths of rays traveling through the aggregate further complicate rendering. To address these challenges, research has focused on strategies to enhance efficiency.

For example, Soulié et al. [78] attempted to reproduce granite using the 3D Voronoi diagram, and Meng et al. [58] modeled tens of millions of particles at three different scales and rendered them using explicit path tracing and approximate computations, depending on visibility. Such an approach demonstrates that rendering objects of the same scale can be optimized by combining the explicit intersection of agglomerates with statistical path construction methods, tailored to the number of ray bounces. This combination balances computational accuracy and efficiency. Müller et al. [63] expanded this method to a model capable of rendering different particle distributions in different spaces.

2.4 Structural Color in Computer Graphics

Play of color is classified as a kind of structural color. As such, this section presents studies on the visual simulation of structural color, categorized according to the optical phenomenon responsible. Structural colors arise from the interference of light, necessitating the use of wave optics for accurate computations. However, in CG, methods for rendering structural colors rely on local illumination models that operate within the framework of the rendering equation. These models avoid the computationally intensive electromagnetic field analysis of the entire scene, providing a more practical approach while achieving visually plausible results.

2.4.1 Diffraction due to Microscopic Irregularities on the Object Surface

The diffraction of light on the fine, uneven structure at the scale of visible light, such as those found on the recording surface of a compact disc, produces structural color.

He et al. [34] and Stam [79] computed diffracted light using the Beckmann–Kirchhoff equation. Thereafter, Cuypers et al. [12] extended Stam's theory to propose a wave-based BRDF utilizing the Wigner distribution function. Meanwhile, Wu and Zheng [97] integrated the Wigner distribution function into microfacet theory, resulting in a BRDF capable of computing light diffraction, absorption, and attenuation simultaneously. Further, Dhillon et al. [15] developed a method of interactively reproducing the diffraction of organisms using a measured model, and Toisoul and Ghosh [85] proposed an efficient data-driven method for rendering diffraction. Finally, Holzschush and Pacanowski [36] presented a method to compute diffraction due to microstructures on microfacets.

2.4.2 Thin-film Interference

On the surface and inside thin films with a thickness comparable to the wavelength of visible light, such as soap bubbles, repeated reflections and refractions cause light wave interference.

Smits and Meyer [77] introduced an optical model for thin-film interference in CG. Subsequently, Gondek et al. [27] proposed a BRDF to represent thin-film interference for spectral rendering. Icart and Arqués [39] attempted to integrate thin-film interference theory into a diffraction model, whereas Belcour and Barla [4] proposed a method for the computational RGB rendering of multiple reflections in a thin film on microfacets. Although the accuracy of this model degrades with coarser microfacets, Kneiphof et al. [53] initiated successful improvements.

2.4.3 Other Structural Colors

Various structural colors observed in nature often arise from the interaction of diffraction and thin-film interference caused by microstructures on the surfaces of objects. In addition, structural colors can also result from 3D microstructures.

Nagata et al. [64] proposed a method for multilayer thin-film interference in pearl, while Sun [82] introduced a model that considers both diffraction by microstructures and interference by multilayer thin films to reproduce the structural colors found on insects. Guillen et al. [31] presented a generic model to reproduce pearlescent materials, and Benamira and Sumanta [5] focused on diffraction-aware hair rendering. Further, Huang et al. [37] developed a model to compute the structural color of the feathers on pigeon necks, and Guo et al. [32] proposed a light-scattering model that pre-computes and considers diffraction and interference by nearby particles in participating media. Finally, Xia et al. [99] reproduced Quetelet scattering, which is the interference between light scattered by particles and light reflected on a water surface. In 2024, a method was introduced for computing Bragg reflections in one-dimensional (1D) photonic crystals [22], such as multilayer thin films. This method accounts for such factors as the layer thickness, refractive index, and surface roughness.

2.5 Summary of Key Differences

In this study, a method focusing on opals is proposed, diverging from a comprehensive gemstone representation approach, as in Guy et al. [33]. Similar to Weidlich and Wilkie [89], the approach in this study explicitly models the internal structure of a gem.

However, while aventurescence occurs near the surface of gemstones, play of color occurs deep inside opal, so it is necessary to define the internal structure in 3D.

Because opal has fewer clusters than granular materials, each cluster is explicitly rendered individually, instead of applying statistical volume rendering. The microscopic structure of opal resembles that described by Guo et al. [32] in that neighboring particles diffract. However, the distinct microscopic regularity of opal results in sharp diffraction peaks, like specular reflection. Consequently, diffraction intensities are computed online rather than via the look-up of pre-computed results, as in Guo et al. [32].

Chapter 3

Research Overview

The objective of this chapter is to cover the physical properties of real opals comprehensibly.

Section 3.1 provides a classification of opals and identifies the specific types of opals covered by this study. **Section 3.2** describes the internal structure of real opals, and **Sec. 3.3** explains the principle of play of color in opals. Subsequently, **Sec. 3.4** reports the results of observing an opal using a digital microscope. Finally, **Sec. 3.5** summarizes the key findings of this chapter and discusses the essential elements required for the visual simulation of opals.

3.1 Classification of Opal and Research Subject

Opals are classified to clarify the specific type of opal considered in this study. The classification result is shown in **Fig. 3.1**. The chemical composition of opal is $\mathrm{SiO_2}{\cdot}n\mathrm{H_2O}$, which consists of silica containing water. According to [47], opals are categorized into three main types: opal-A (A: amorphous), opal-CT (CT: cristobalite-tridymite), and opal-C (C: cristobalite). Opal-A is an aggregate of amorphous silica spheres and is generally used as a gemstone. Opal-CT was previously believed to contain both cristobalite and tridymite, but recent research by Fröhlich [23] has shown that it is actually a mixture of amorphous silica and tridymite. Opal-C contains poorly crystalline cristobalite.

In addition, opal-A is further classified into opal-AG (AG: amorphous-gel) and opal-AN (AN: amorphous-network) [29]. Opal-AG, which forms through a slow agglomeration process from a solution, exhibits play of color. Opals exhibiting play of color are referred to as precious opals [46] and are highly prized as gemstones. Australia, Brazil, and Ethiopia are renowned for their opal production. In contrast, opal-AN forms through the rapid cooling of high-temperature silica fluid and does not exhibit play of color. Opals

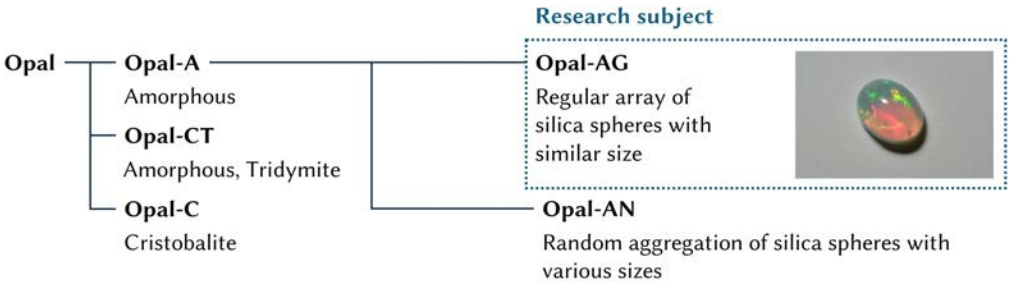

Fig. 3.1 Classification of opals and the subject of this study. Because there are opals with various properties other than Opal-AG, it is important not to confuse these properties when constructing a visual simulation model. The present study is based on Opal-AG

that do not exhibit play of color are referred to as common opals [46], while those with a milky white appearance are prized as hyalites. Lee et al. [56] found that opal-AG contains a regular arrangement of silica spheres with diameters of less than 400 nm, whereas opal-AN consists of randomly aggregated silica spheres of varying sizes, typically less than 5 nm in diameter.

In this study, the visual simulation focuses on opal-AN, modeling its internal structure and optical phenomena to represent the play of color characteristic of opal. Unless otherwise specified, opal-AG will be referred to simply as 'opal' in this dissertation.

3.2 Internal Structure of Real Opals

Macroscopically, opal is an amorphous quasi-mineral primarily composed of silicon dioxide. **Figure 3.2** presents images of real opals, the smallest unit of which is a silica sphere (**Fig. 3.3a**) with a particle diameter of 400 nm or less [46]. Due to their size, silica spheres in opal are classified as colloids, amorphous spheres that lack a regular atomic arrangement. Opals also contain impurities [25] within the silica spheres and in the gaps between them, so the scattering and absorption of light due to these impurities determine the opal's base color, which is primarily white (**Fig. 3.2a**), with black [57] and red [75] being the next-most well-known. Opals with a black base color are referred to as black opals (**Fig. 3.2b**) and those with a reddish base color are called fire opals (**Fig. 3.2c**). Black opal consists of silica spheres where some Si^{4+} are replaced by Al^{3+}, while fire opal contains Fe^{3+} instead.

Silica spheres are aligned inside an opal, forming a face-centered cubic (fcc) lattice or hexagonal close-packed (hcp) structure. The term "crystal" traditionally refers to the arrangement of atoms and molecules, and the arrangement of colloids similar to a crystal

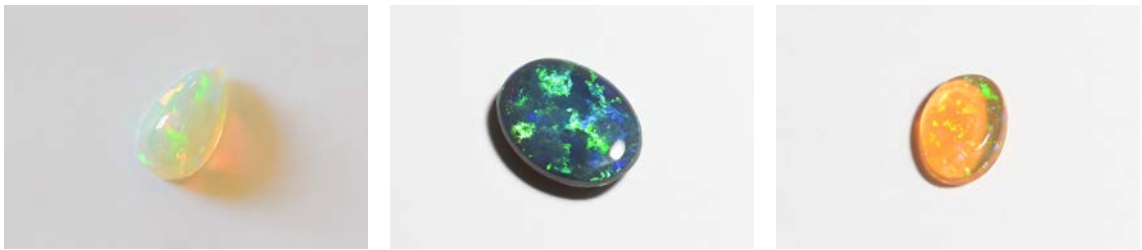

(a) White opal (b) Black opal (c) Fire opal

Fig. 3.2 Photographs of real opals, which show play of color. Base color is typically white (a), while color variations include black (b) and red (c). These color variations result from the absorption and scattering of light by impurities present in the opal. Black opal contains aluminum ions, whereas fire opal contains iron ions

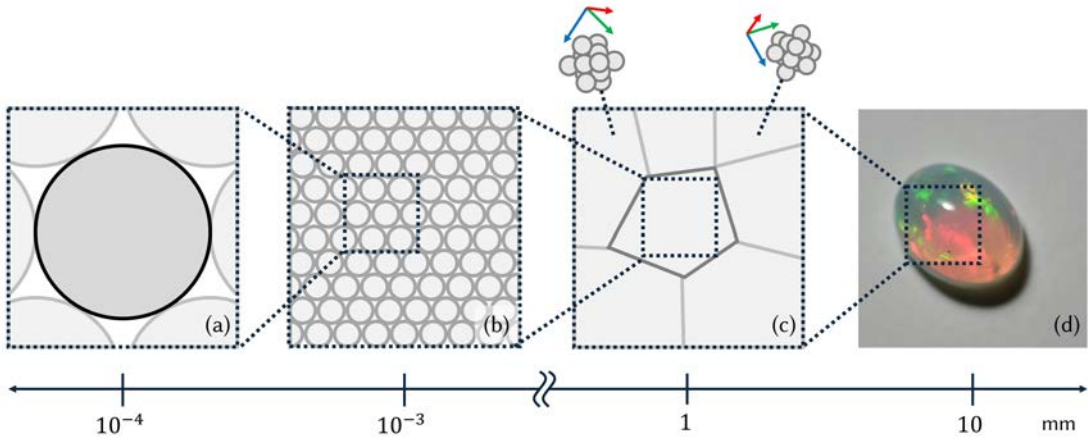

Fig. 3.3 Internal structure of opal. The smallest unit of an opal is a silica sphere (a) with a diameter of several hundred nanometers, and impurities are contained within the silica spheres and in the gaps between them. Many silica spheres stack to form a colloidal crystal (b). These colloidal crystals randomly organize into colloidal polycrystalline structures (c), collectively constituting an opal (d)

structure is called a colloidal crystal (**Fig. 3.3b**). The tone of the play of color arises from the 3D diffraction of light due to the colloidal crystal structure.

Colloidal crystals, aggregates of silica spheres, form a polycrystalline structure over extended distances (**Fig. 3.3c**), known as a colloidal polycrystalline structure. The individual colloidal crystal structures forming colloidal polycrystalline structures are termed colloidal crystal grains. As such, the play of color observed in opals is not simply a shift in structural color; rather, it is characterized by a complex varying pattern dependent on the direction of light sources and the viewpoint. Meanwhile, the pattern of the play of color is attributed to the colloidal polycrystalline structure.

3.3 Principle of Play of Color Among Opals

The short-range regular structure of an opal is responsible for the coloring in its play of color, while the long-range random structure contributes to the overall pattern. When focusing on a particular grain, it has a colloidal crystal structure, where colloids of the same size are aligned. Although colloidal crystals in opals have been known to mimic an fcc or an hcp structure, for simplicity, it is assumed that all silica spheres exhibit an fcc structure. A schematic diagram of fcc is shown in **Fig. 3.4a**, where the colloids constituting the opal are approximately the size of visible light and the regular arrangement in the colloidal crystal structure causes the diffraction of visible light, resulting in the appearance of structural color. When light enters the colloidal crystal from the air, the condition

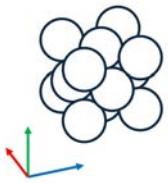

(a) fcc structure

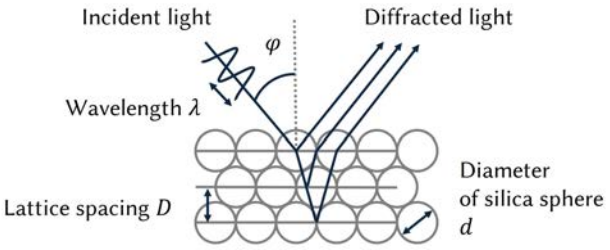

(b) Parameters of the Bragg–Snell condition

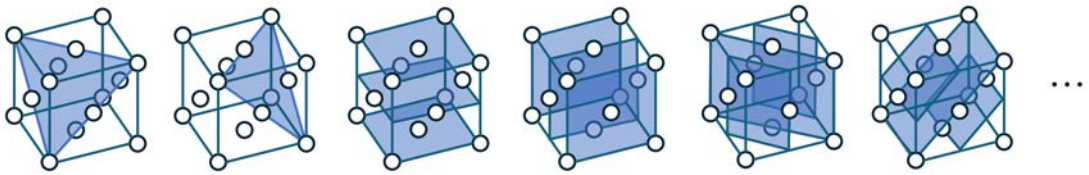

(c) Examples of diffraction planes in fcc structure

Fig. 3.4 Diffraction via the periodic structure within an opal. A colloidal crystal with a face-centered cubic (fcc) structure (a) diffracts visible light due to its periodic structure (b). The diffraction mechanism is similar to that of multilayer reflection, but opal is characterized by the presence of many diffraction planes in three-dimensional directions (c)

for the wavelength λ of diffraction is known as the Bragg–Snell condition:

$$m\lambda = 2D\left(n^2 - \sin^2\theta\right)^{\frac{1}{2}}, \tag{3.1}$$

where m denotes the diffraction order, D the lattice spacing, n the average refractive index of the colloidal crystal, and θ the incidence angle. In the case of an fcc structure, the relationship between D and the diameter of a silica sphere d, illustrated in **Fig. 3.4b**, is given by:

$$D = \sqrt{\frac{2}{3}}d.$$

Because colloidal crystals are 3D microstructures, there are multiple methods of forming a lattice plane in a single colloidal crystal (**Fig. 3.4c**). Opal exhibits a colloidal polycrystalline structure, with each grain having a distinct crystal lattice tilt. Consequently, the normal of the diffraction plane varies from region to region, resulting in complex patterns within a single opal.

3.4 Observation of Opals Using a Digital Microscope

When modeling the internal structure of opals, it is necessary to determine the sizes of colloidal grains. However, to the best of current knowledge, no reports exist with measurements of colloidal crystal grain sizes in natural opals. Therefore, colloidal grain sizes in real opals were observed using a Leica DVM6 digital microscope.

The results are presented in **Fig. 3.5**, where the sizes were found to be around 1–3 mm.

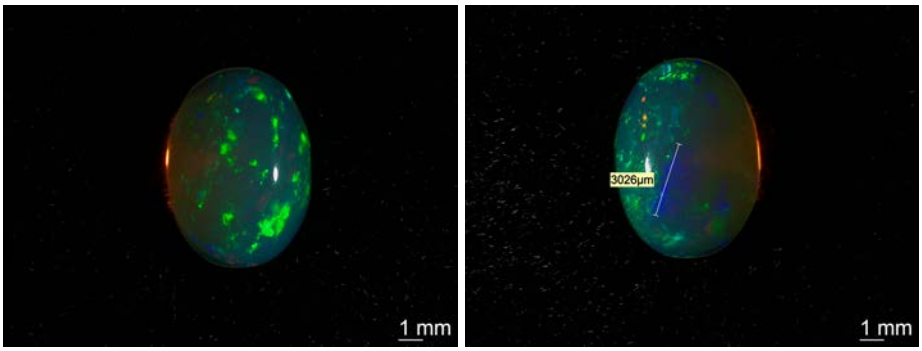

(a) Ethiopian opal

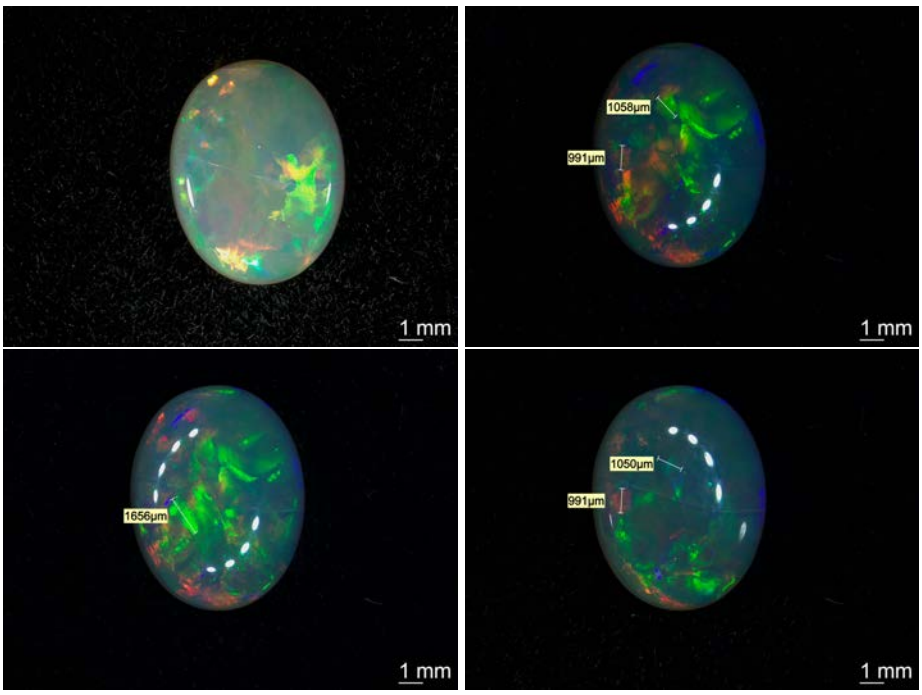

(b) Australian opal

Fig. 3.5 Observation of opals using a digital microscope. Grain size is around 1 mm to 3 mm

3.5 Research Direction

This chapter detailed the physical properties of opals based on findings from a literature review and observation. In summary, opals consist of aggregates of silica spheres, which have a regular structure on short-range scales and a random structure on long-range scales. The primary optical property of interest in opals is play of color, wherein the short-range regular structure determines the color and the long-range random structure influences the observed pattern. Another distinguishing feature of opals is their base color, which is influenced by impurities within the material.

To represent the visual characteristics of opals accurately, the following three elements must be addressed:

1. **Modeling the stacking structure of silica spheres.** The stacking arrangement of silica spheres determines the pattern of play of color. Therefore, it is necessary to model the stacking structure appropriately.

2. **Light diffraction modeling for colloidal crystal grains.** The color of play of color is caused by the diffraction of light when light enters the colloidal crystal grains. A model to determine the diffraction direction and intensity of the incident light is required.

3. **Base color representation.** The base color is governed by impurities in the opal. Consequently, it is necessary to define the spatial distribution of these impurities and implement a model to evaluate their optical properties.

The following sections will outline the modeling strategies employed to address each of these elements.

3.5.1 Internal Structure for Representing Play of Color

The fundamental structural unit of an opal is a silica sphere, which has a diameter of several hundred nanometers. However, opals used as gemstones typically measure several centimeters in size. Accurate modeling of this stacking structure is impractical, at least in the context of visual simulation, given current computational limitations. Consequently, it is necessary to propose a model that abstracts the stacking structure while preserving the visual properties responsible for play of color.

Focusing on the short-range arrangement of silica spheres, specifically within colloidal grains, the silica spheres are regularly aligned. Thus, this direction can be represented by defining only the basis vectors that determine the orientation of the colloidal grains,

effectively recovering the direction of silica sphere alignment. Conversely, the random stacking structure of the colloidal grains must be retained because it determines the pattern of play of color. As noted in **Sec. 3.4**, The scale of colloidal grains is approximately several millimeters. This is a scale that can be modeled on a computer, even compared to the size of an opal. Therefore, the internal structure of the opal is determined at the colloidal grain level to reproduce play of color.

This study addresses this issue in **Secs. 4.1–4.4**.

3.5.2 Diffraction Model for the Periodic Structure

As described in **Sec. 3.3**, the color of play of color arises from the diffraction of incident light on the colloidal grains, which exhibit a regular internal structure. To simulate play of color, it is essential to develop a model capable of determining the diffraction direction and intensity of the outgoing light.

For colloidal aggregates with a size of several hundred nanometers, one approach to computing the scattering distribution of outgoing light involves precomputing a scattering distribution function, storing it in a table, and referencing it during rendering to determine the diffraction direction, as demonstrated in Guo et al. [32]. However, diffraction from aggregates with a regular structure is expected to have a highly sharply peaked scattering distribution function, which occurs when the conditions described in **Eq. (3.1)** are satisfied. In such cases, the resolution of the table must be high, and it is also inefficient in terms of searching for the outgoing direction of light. To address these issues, this study proposes a method to determine whether the conditions of **Eq. (3.1)** are satisfied on the fly and to determine the outgoing direction of light.

This study addresses this issue as discussed in **Sec. 5.3**.

3.5.3 Representation of Base Color

Impurities within silica spheres and in the gaps between them cannot be modeled explicitly due to their microscopic size, as discussed in **Sec. 3.5.1**. Usually, substances of such small dimensions are typically represented on such a scale as participating media in visual simulation.

In this study, impurities are likewise treated as participating media, with their distribution defined and statistically processed using techniques of volume rendering. This study addresses this issue as discussed in **Secs. 4.5** and **5.4**.

Chapter 4

Modeling

This chapter proposes a method for modeling the internal structure of opals and describes how to represent the proposed model on a computer.

Opals are commercially valuable gemstones, but it is challenging to access details of their production methods. In this study, the synthesis process of opals is described with reference to a report on the synthesis of synthetic opals [21]. According to this report, the synthesis of opals can be outlined in three major steps:

1. **Synthesis of silica spheres.** Silica spheres of uniform size are chemically synthesized. Artificial opals are produced using solutions containing these spheres.

2. **Formation of colloidal grains through aggregation.** The solution is left under gravity or in an artificial environment, such as a centrifuge. Silica spheres aggregate in the solution to form numerous colloidal grains. These colloidal grains settle and stack due to gravity.

3. **Grain growth through sintering.** The sedimented grains are heated to increase their strength. During this process, some colloidal grains fuse with adjacent grains.

This study models the internal structure of opals at the colloidal grain level by mimicking these three steps. Specifically, this study focuses on the fact that the formation process of opal closely resembles the Voronoi diagram-drawing algorithm and approximates the internal structure using the Voronoi tessellation. The Voronoi tessellation is weighted to represent the growth direction of colloidal grains. In addition, the percolation of the graph constructed by the sites of the Voronoi diagram is computed to simulate the sintering process. A schematic diagram of the opal modeling method proposed in this chapter is presented in **Fig. 4.2**.

Section 4.1 describes the definition of a Voronoi tessellation, the drawing method of a Voronoi diagram, and its relationship to the opal generation process. **Section 4.2** introduces percolation theory and explains its application in mimicking the sintering process of opals. Based on the contents of **Secs. 4.1** and **4.2**, **Sec. 4.3** describes the internal structural model of the opal proposed in this study. **Section 4.4** compares two methods for representing the internal structure of opals on a computer: one storing only sites and the other using voxel-based representation. The advantages of each method are discussed. **Section 4.5** outlines a method for modeling the base color of opals, while **Sec. 4.6** describes a method for defining the external outline of an opal. **Section 4.7** summarizes the contents of this chapter and organizes the parameters that can be adjusted in the proposed model and the corresponding internal structure elements.

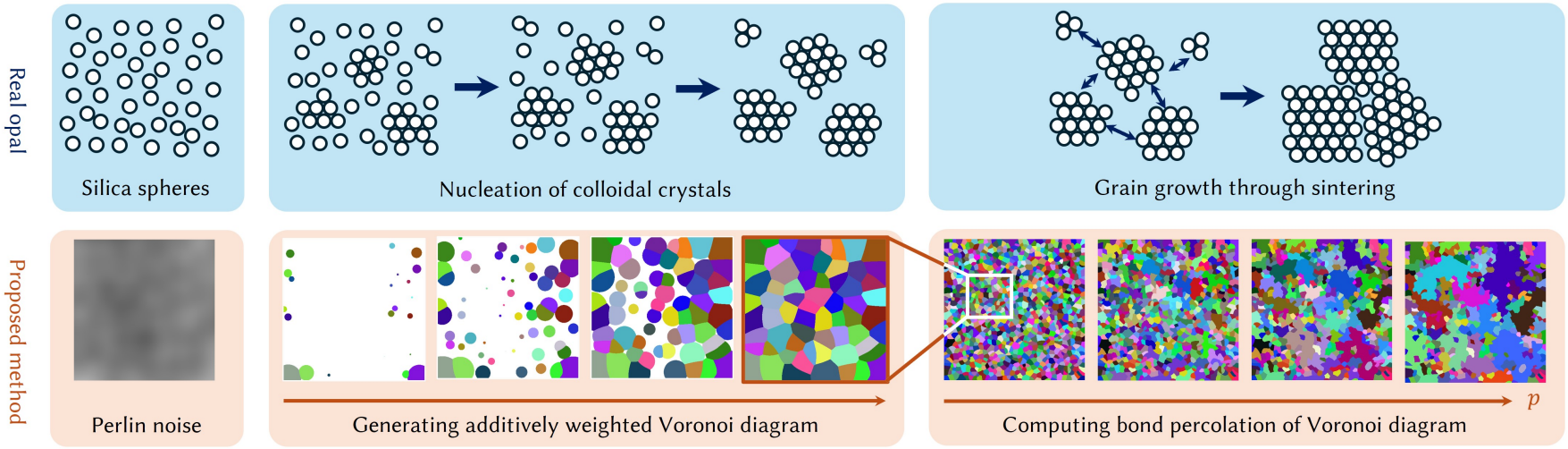

Fig. 4.1 The process of modeling the internal structure of an opal using the proposed method. For simplicity, the figure is presented on a two-dimensional (2D) plane. Initially, the concentration field of the silica spheres is represented using Perlin noise. Subsequently, the colloidal polycrystalline structure formed through nucleation is represented by an additively weighted Voronoi diagram, weighted by Perlin noise. Finally, the bonding of adjacent grains through sintering is represented by bond percolation within the network formed by the sites of the Voronoi diagram

4.1 Voronoi Tessellation

This section defines Voronoi tessellation and explains how to draw a Voronoi diagram and an additively weighted Voronoi diagram. The relationship between Voronoi tessellation and colloidal aggregation is also explained.

4.1.1 Definition of Voronoi Tessellation and Voronoi Diagram

According to Aurenhammer [1], a Voronoi diagram is defined as follows. Let S be a set of points along the plane, where $p, q \in S$. The leading domain of p with respect to q, denoted as $dom(p, q)$, is the set of points in the plane that is closer to p than to q or is equidistant from both. Formally, $dom(p, q)$ can be expressed as:

$$dom(p, q) = \{x \in \mathbf{R}^2 \mid \delta(x, p) \leq \delta(x, q)\}, \tag{4.1}$$

where $\delta(\mathrm{x}, \mathrm{p})$ represents the Euclidean distance from point x to p. For a given $p, q \in S$, $dom(p, q)$ is a half-plane bounded by the perpendicular bisector of p and q. The domain of a specific point $p \in S$, referred to as $reg(p)$, is defined as:

$$reg(p) = \bigcap_{q \in S - \{p\}} dom(p, q). \tag{4.2}$$

The regions $reg(p)$ form a polygonal partition of the plane, which is called a Voronoi tessellation. Each partitioned region is referred to as a Voronoi region or Voronoi cell, while the boundaries of these regions are called Voronoi boundaries. Voronoi tessellations can be extended to n-dimensional spaces. A Voronoi diagram on a 2D plane is shown in **Fig. 4.2**. Note that the distance field shown in **Fig. 4.2b** is visualized in black color as it gets closer to the sites.

A notable property of Voronoi diagrams is that each Voronoi region is convex. In a Voronoi diagram, the Voronoi boundary corresponds to segments of the perpendicular bisectors of the two sites.

4.1.2 Weighted Voronoi Diagram

Voronoi diagrams can exhibit various properties depending on the definition of $\delta(x, p)$ in **Eq. (4.1)**. For instance, an additively weighted Voronoi diagram [1] modifies $\delta(x, p)$ by incorporating a weight $w(p) \in \mathbf{R}$ associated with each site p. The weighted distance function $\delta_a(x, p)$ is defined as:

$$\delta_a(x, p) = \delta(x, p) - w(p). \tag{4.3}$$

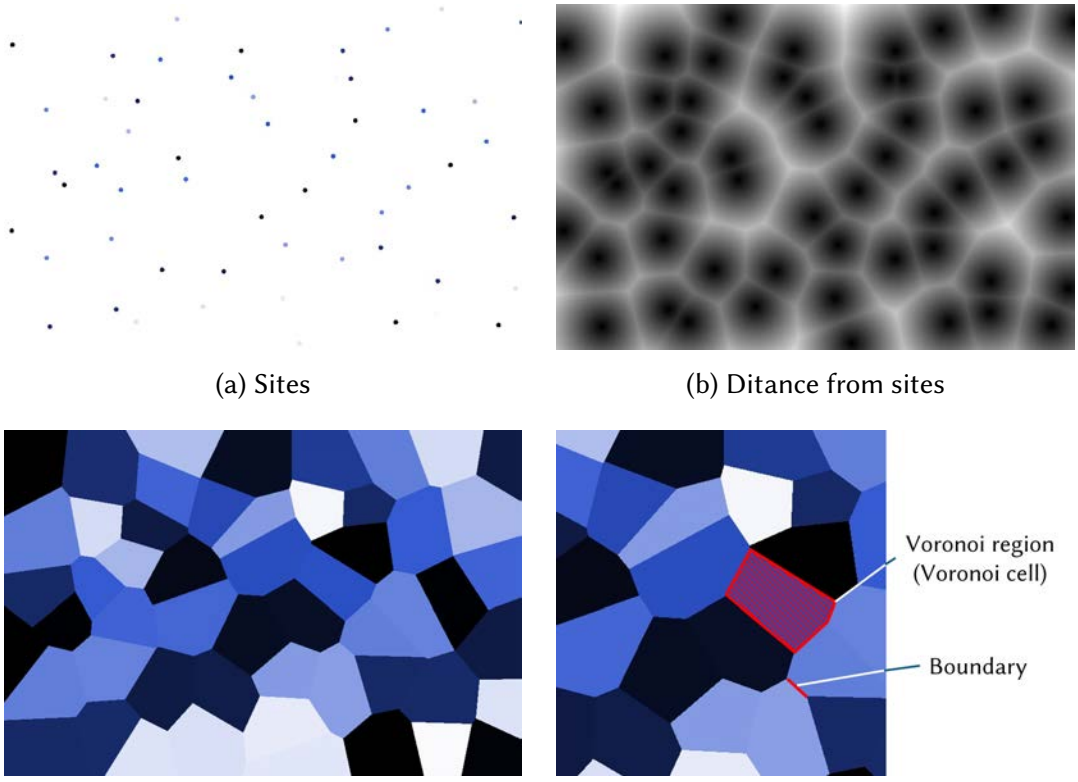

(a) Sites (b) Ditance from sites

(c) Voronoi diagram (d) Voronoi region and boundary

Fig. 4.2 A 2D Voronoi diagram. A Voronoi diagram (c) is constructed as follows: (a) given a set of sites, (b) the distance field from these sites is computed, and (c) the Voronoi diagram is obtained by partitioning the space based on the closest site. This process of dividing the space is known as Voronoi tessellation. (d) Each partitioned region is referred to as a Voronoi region or Voronoi cell

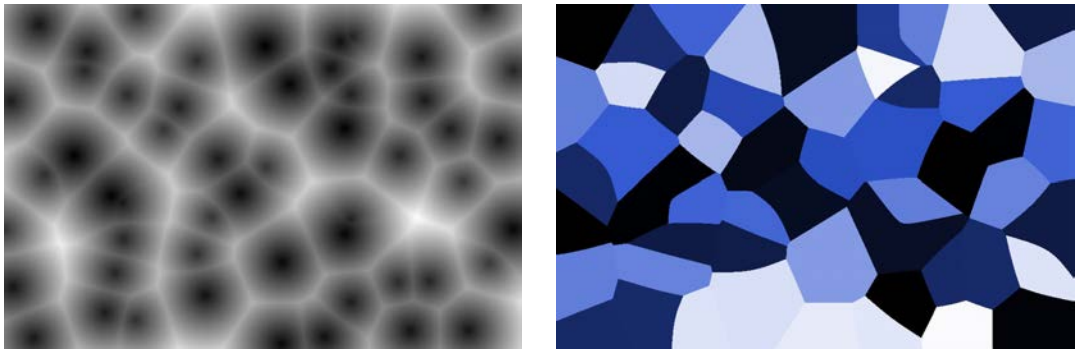

(a) Ditance from sites (b) Voronoi diagram

Fig. 4.3 The visualization of a distance field using additively weighted distances and the corresponding 2D Voronoi diagram. The boundaries are characterized by a hyperbolic surface

Figure 4.3 shows the additively weighted distance field and additively weighted Voronoi diagram on a two-dimensional (2D) plane.

The Voronoi boundary of an additively weighted Voronoi diagram is known to be hyperbolic in the 2D case and a bimodal hyperbolic surface in the 3D case. Refer to **Appendix A.1** for the definition and appearance of other Voronoi diagrams.

4.1.3 Creation of Voronoi Diagram

This section introduces the method for drawing Voronoi diagrams, specifically the wavefront method, named for the way waves appear to radiate outward from the site. It is often used to explain the concept of Voronoi diagrams because it is intuitively easy to understand. The method for constructing a Voronoi diagram using the wavefront method involves the following steps:

1. **Initialize the wavefront.** Place the sites in space and generate circular waves from each point in the 2D case or spherical waves in the 3D case.

2. **Wavefront expansion.** The wavefronts generated from each site expand at a constant velocity. Intuitively, this can be seen as a circular wave spreading out from the site. The area covered by each wavefront corresponds to the region of influence for each site.

3. **Stopping the wavefront.** When a wavefront from one site collides with a wavefront from another, the expansion stops at the point of collision. This collision point forms the Voronoi boundary.

4. **End condition.** The construction of the Voronoi diagram is complete when the waves have expanded throughout the entire space and all regions have been determined.

Figure 4.4 illustrates the process of plotting a Voronoi diagram using the wavefront method. **Algorithm 4.1** presents a pseudo-algorithm for constructing a discrete Voronoi diagram using this approach. The wavefront method can also be extended to additively weighted Voronoi diagrams, as shown in **Fig. 4.5**. In the context of the wavefront method, additive weights intuitively represent differences in the timing of wave propagation from the sites.

Although the wavefront method provides an intuitive and straightforward approach to constructing Voronoi diagrams, it is computationally expensive when applied to the construction of discrete Voronoi diagrams. For practical applications, the jump flooding algorithm [72] is employed, as it allows for efficient computation on a GPU.

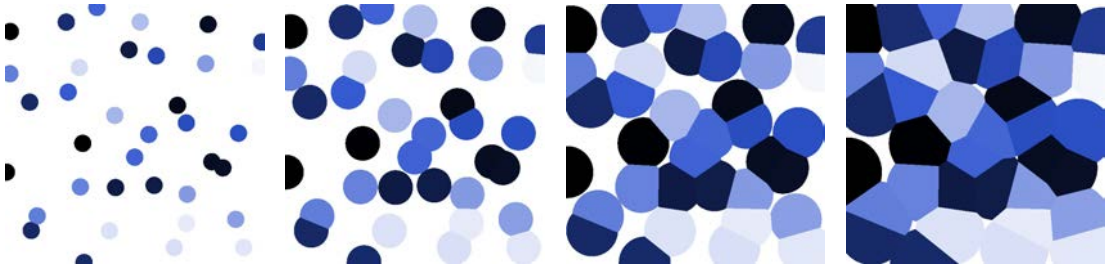

(a) (b) (c) (d)

Fig. 4.4 The process of constructing a Voronoi diagram using the wavefront method. Wavefronts are expanded in the order of (a) to (d)

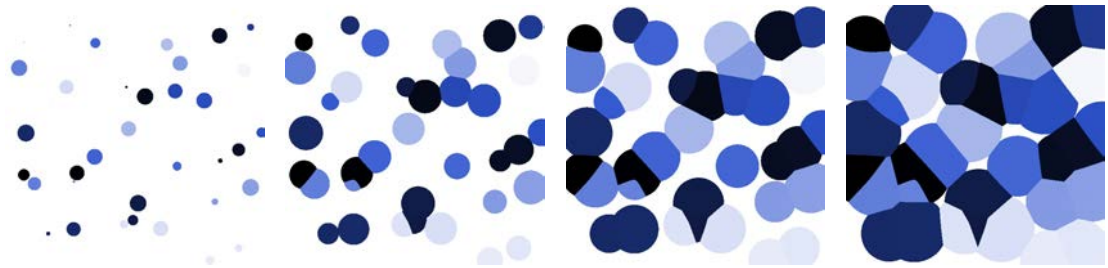

(a) (b) (c) (d)

Fig. 4.5 The process of drawing an additively weighted Voronoi diagram using the wavefront method. The wavefronts are expanded in the order of (a) to (d). When additively weighted, the expansion speed is the same for all wavefronts, but the timing at which the wavefronts begin to expand differs depending on their weights

4.1.4 Similarity Between Colloidal Agglomeration and Voronoi Diagram Drawing Algorithms

The wavefront method for drawing Voronoi diagrams involves generating wavefronts from each site and designating the regions nearest each point as respective domains in sequence. Similarly, in the natural formation of opals, colloidal grains are created as silica spheres in solution aggregate to form a nucleus, which subsequently incorporates surrounding silica spheres. This similarity forms the basis for adopting Voronoi diagrams to model the colloidal grains of opals in this study. In the proposed internal structure model, each Voronoi region corresponds to a colloidal grain. Notably, Voronoi diagrams are utilized in materials engineering to represent the polycrystalline structures of metals [70]. Furthermore, visual simulations employing Voronoi diagrams to approximate polycrystalline structures have also been reported [78].

The process of constructing an additively weighted Voronoi diagram using the wave-

Algorithm 4.1 Compute the wavefront method

Require: `grid` (2D array initialized with `UNASSIGNED`), `sites` (list of site positions and IDs)

Ensure: `grid` with each cell labeled by the nearest ID

```
Initialize an empty queue
for each site in sites do
    Set grid[site.x][site.y] = site.id
    Add site to queue
end for
while
     do  cell = Dequeue(queue)
    for each neighbor of cell do
        if grid[site.x][site.y] == UNASSIGNED then
            set grid[site.x][site.y] = cell.id
            Enqueue(queue, neighbor)
        end if
    end for
end while
return grid
```

front method, as depicted in **Fig. 4.5**, illustrates that additive weights serve as parameters that adjust the timing of wavefront expansion. In the context of colloidal grain formation, where the timing of nucleation can vary based on solution concentration and gravitational effects, these additive weights are employed as parameters to represent the direction of grain growth. **Figure 4.6** demonstrates how additively weighted Voronoi diagrams are generated using vertically and concentrically weighted sites.

4.2 Percolation Theory and Sintering Process

Broadbent and Hammersley [9] first proposed a model called Bernoulli percolation, and since then, percolation theory has been studied primarily in the fields of mathematics and physics. Concerning the history of the development of percolation models, see a thorough survey by Duminil-Copin [18]. Percolation is a model that explores the properties of a graph by removing edges or nodes probabilistically, where the model for removing edges is known as bond percolation, and the model for removing nodes is referred to as site percolation. This concept can be applied to problems concerning material conductivity and information propagation.

(a) Weight (b) Growth of the Voronoi region with respect to the weights of (a)

(c) Weight (d) Growth of the Voronoi region with respect to the weights of (c)

Fig. 4.6 Additively weighted Voronoi diagrams created with (a) vertically weighted sites and concentrically weighted sites using the wavefront method. In (b), the Voronoi region expands from the bottom to the top, while in (d), it grows from the outside toward the center

In this study, the Bernoulli percolation model, a type of bond percolation, was employed to approximate colloidal grain growth, and this model randomly determines edge existence probabilities following a Bernoulli distribution. Implementation involves assigning a uniformly random value in $[0, 1]$ to each graph edge, removing edges when their values exceed the threshold $p \in [0, 1]$, and retaining edges when they are below the threshold. An example of Bernoulli percolation on an orthogonal grid is illustrated in **Fig. 4.2**, computed on the graph comprising the sites of a Voronoi diagram to represent the merging of adjacent grains according to grain growth (**Fig. 4.2**c bottom). The graph formed by the sites can be easily obtained by considering a Delaunay triangulation, which is the dual of the Voronoi diagram. In the graph obtained after the percolation computation, the adjacent nodes are considered a single grain bounded by grain growth.

4.3 Modeling Internal Structure of Opal

Based on the contents of **Secs. 4.1** and **4.2**, the internal structure model of opals proposed in this study is presented. **Table 4.1** summarizes the correspondence between real opals and the proposed internal structure model. The procedure for generating the model is outlined in the following sequence: arrangement of the sites, assignment of weights to the sites, definition of grain size, and specification of the orientation of the lattice planes within each grain.

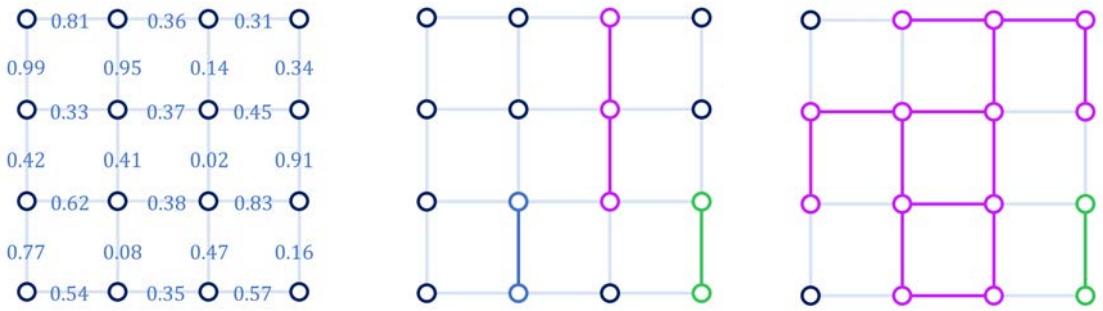

(a) Initial state (b) $p = 0.25$ (c) $p = 0.5$

Fig. 4.7 Examples of Bernoulli percolation on a 4×4 grid. First, the edges of the graph are assigned values [0, 1] using uniformly random numbers (a). Then, edges with a value greater than the threshold p are removed. The results for p, set to 0.25 and 0.5, are shown in (b) and (c), respectively

Table 4.1 Correspondence between real opal and the proposed internal structure model. Representation of the physical properties and formation process of opals at a computable scale for enabling visual simulation

A real opal	The proposed method
Silica sphere	No explicit modeling (using grain size and average refractive index as constants)
Colloidal grain	Voronoi region in a 3D Voronoi diagram
Tilt of a colloidal grain	Quaternion
Concentration distribution of colloidal solution	Perlin noise
Colloidal grain formation	3D Voronoi tessellation
Direction of colloidal grain deposition	Additive weights of Voronoi diagram
Binding of colloidal grains by sintering	Bernoulli percolation

4.3.1 Internal Structure Model

In this study, the internal structure of an opal is modeled using a Voronoi diagram, where each Voronoi region corresponds to a colloidal grain. The silica spheres comprising the colloidal grains are not explicitly represented; instead, only the inclination of the grains is preserved for each Voronoi region. This approach is justified because the diffrac-

tion equation for colloidal grains in **Eq. (3.1)** requires the parameter D, which is derived from the grain diameter d in **Eq. (3.2)**, and the angle of incidence θ, which can be determined based on the grain tilt and direction of incident light. In addition, the diffraction of light depends solely on the average refractive index n of the colloidal crystal, which remains consistent across the structure. Because the grain sizes of silica spheres in opals are typically uniform and the average refractive index is constant, these parameters are sufficient and can be treated as constants. Therefore, the model conserves only the grain tilt for each colloidal grain, expressed in this study using quaternions to represent 3D rotations.

The formation process of colloidal grains is simulated using a 3D Voronoi tessellation. Meanwhile, the process of colloidal sedimentation and deposition and the growth of opal are represented using the additive weights of the Voronoi diagram, as shown in **Fig. 4.6**. This process is modeled by incorporating additive weights in the Voronoi diagram to simulate the vertical settling and deposition of colloids. Finally, the partial binding of colloidal grains through sintering is represented using Bernoulli percolation.

4.3.2 Generation of Internal Structure Model

A method is proposed to generate the internal structure of an opal based on its formation process.

(1) Field initialization. A colloidal solution concentration field is defined within a 3D space representing the opal. In this method, the concentration distribution of the colloidal solution is assumed to follow Perlin noise [68], which is used for initialization. As shown in **Fig. 4.8**, Perlin noise is used to represent the concentration distribution of the solution in this study, due to its continuous variation with randomness. However, simplex noise or power noise, both of which exhibit similar characteristics, can be used as alternatives.

(2) Placement of sites. Sites are placed in the field using Poisson disk sampling [10]. Poisson disk sampling is a technique that ensures sampled points are no closer than a specified radius r to each other while maintaining randomness. This approach allows partial control over the size of the colloidal grains by adjusting r.

(3) Assignment of weights to sites. Weights are assigned to the placed sites using methods such as a signed distance field. Smaller weights correspond to earlier initiation times for the growth of the Voronoi regions. When modeling a real opal, the weights must satisfy the condition:

$$|w(p_i) - w(p_j)| < r,$$

for all sites, where $w(p_i)$ represents the weight at a site p_i and r is the sampling radius used in Poisson disk sampling, derived from **Eq. (4.3)**.

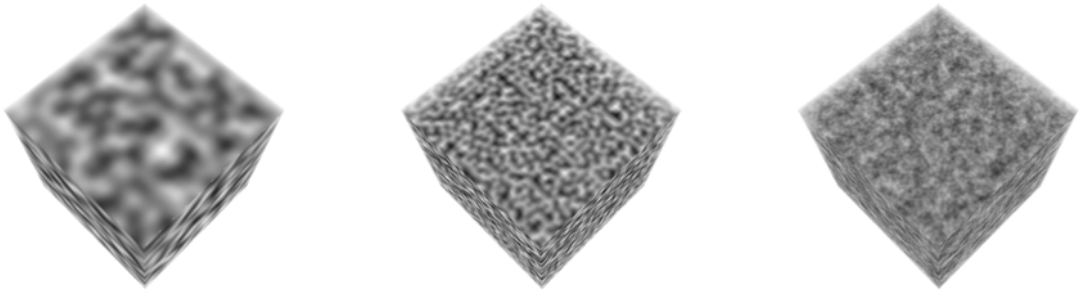

(a) (b) (c)

Fig. 4.8 Visualization of Perlin noise. Perlin noise exhibits continuous variation with randomness (a). By modifying the scale (b) and applying layering (c), variations can be introduced to the pattern, making it widely used in computer graphics modeling

(4) Specification of grain size and average refractive index. The grain size of the silica spheres and the average refractive index of the colloidal crystals are specified. The silica spheres forming the opal that exhibits the play of color typically range in size from 100 to 300 nm. The average refractive index n is computed using the following equation:

$$n = fn_{\mathrm{s}} + (1 - f)n_{\mathrm{w}},$$

where n_{s} is the refractive index of silica spheres, n_{w} is the refractive index of water, and f is the filling factor of the colloidal crystal. The colloidal crystal forms a face-centered cubic (fcc) structure, which is known to have a filling factor of approximately 74%, with the remaining voids filled with water.

(5) Determination of the lattice plane tilt in each grain. The orientation of uniformly random grains is generated by Shoemake's algorithm [74] and stored as quaternions.

(6) Voronoi tessellation. Voronoi tessellation is performed based on the sites and their weights, generating an additively weighted Voronoi diagram.

(7) Computation of percolation. To compute percolation, a Delaunay triangulation is constructed based on the Voronoi diagram, and each edge is assigned a value in $[0, 1]$ using a uniformly generated random number. Thereafter, the threshold is set appropriately, and the percolation process is applied to the network of sites.

4.4 Data Structure to Represent Opal

This section introduces two data structures for representing the generated data: one that stores only the sites and reconstructs the Voronoi diagram dynamically during rendering and another that represents the internal structure using voxels and a codebook.

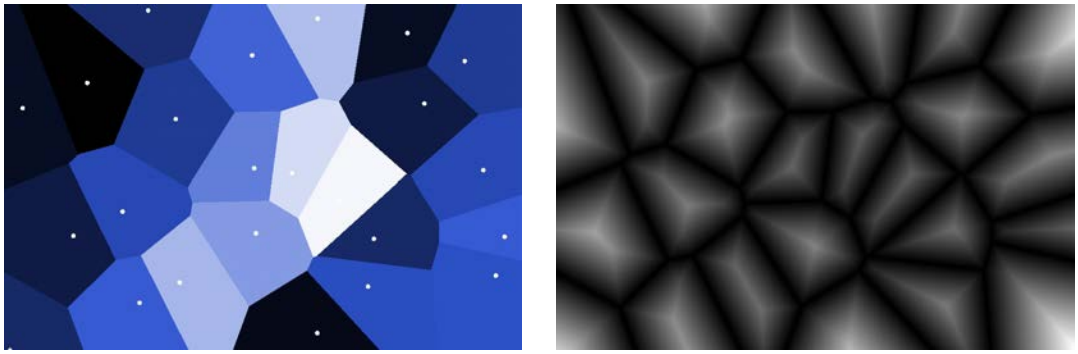

(a) Voronoi diagram (b) Distance from boundaries

Fig. 4.9 A distance field derived from the Voronoi boundary, generated based on the positional information of the sites. When the Voronoi boundary is obtained through ray marching, the distance field must have a value of zero precisely at the Voronoi boundary

4.4.1 Method for Storing Only Sites

In a 3D Voronoi diagram, the Voronoi boundary is a segment of the perpendicular bisector between two sites. By combining planar distance functions to define a distance field with a zero value at the Voronoi boundary, sphere tracing can be employed to determine intersections at the Voronoi boundary. For more details on sphere tracing, refer to **Appendix A.2**.

At a point $\boldsymbol{x}$ in 3D space, let $\boldsymbol{p_0}$ represent the coordinate of the site nearest $\boldsymbol{x}$, and let $\boldsymbol{p}$ denote a site whose Voronoi region shares a boundary with the Voronoi region dominated by $\boldsymbol{p_0}$. The distance function $sdf_{\text{plane}}(\boldsymbol{x}, \boldsymbol{p_0}, \boldsymbol{p})$ describing the plane forming the Voronoi boundary can be defined as follows:

$$\begin{aligned} sdf_{\text{plane}}(\boldsymbol{x}, \boldsymbol{p_0}, \boldsymbol{p}) &= \frac{(\boldsymbol{p_0} - \boldsymbol{p}) \cdot (\boldsymbol{x} - \boldsymbol{m})}{|\boldsymbol{p_0} - \boldsymbol{p}|}, \\ \boldsymbol{m} &= \frac{\boldsymbol{p_0} + \boldsymbol{p}}{2}. \end{aligned}$$

If this computation is performed for all p and the resulting field is constructed using their minimum values, a distance field that defines the Voronoi boundary is obtained, as illustrated in **Fig. 4.9**(b). It is important to note that the distance field required for sphere tracing is zero at the surface, differing from the distance field shown in **Fig. 4.2**(b), where it is zero at the sites.

For the Voronoi boundary in an additively weighted Voronoi diagram, hyperbolic surfaces and their intersections can be determined based on the locations and weights of the sites following the method proposed by Wood et al [95]. If the Euclidean distance between two sites is $2c$ and the difference in their weights is $2a$, the distance t from the

origin of the ray $\boldsymbol{x}$ to the hyperbolic surface can be computed as a solution to the quadratic equation:

$$\boldsymbol{v}^T\boldsymbol{Q}\boldsymbol{v}t^2 + 2\boldsymbol{v}^T\boldsymbol{Q}\boldsymbol{x}t + \boldsymbol{x}\boldsymbol{Q}\boldsymbol{x} = 0, \tag{4.4}$$

where $\boldsymbol{v}$ is the ray's direction vector and the matrix $\boldsymbol{Q}$ is defined as:

$$\boldsymbol{Q} = \begin{pmatrix} a^2 - c^2 & 0 & 0 & 0 \\ 0 & a^2 & 0 & 0 \\ 0 & 0 & a^2 & 0 \\ 0 & 0 & 0 & a^2(c^2 - a^2) \end{pmatrix}. \tag{4.5}$$

Let D be the discriminant from **Eq. (4.4)**. If $D < 0$, there is no intersection. If $D = 0$, the intersection distance is given by t if $t > 0$; otherwise, no intersection is assumed. In cases where two values of t satisfy this condition, the smaller t represents the intersection distance.

These methods are memory-efficient because the entire Voronoi diagram can be reconstructed solely from the positions and weights of the sites. Consequently, the required memory usage increases linearly with the number of sites. However, a notable drawback of these methods is the frequent memory access required to search the neighborhood of the sites, which can lead to performance overhead.

4.4.2 Method for Using Voxels

The implicit method reconstructs the Voronoi diagram on the fly based on the positional information and weights of the sites, requiring computation for each queried point. In contrast, the explicit method using voxels retrieves the current Voronoi diagram and boundaries directly from the voxel data. As such, this study employs the explicit method.

Because the proposed model maintains a consistent crystal tilt within the same Voronoi region, a codebook is used to minimize memory usage, as illustrated in **Fig. 4.10**. After representing the internal structure following the procedure described in **Sec. 4.3.1**, only the Voronoi region IDs are stored in the voxel data. Subsequently, a codebook is created to map each ID to its corresponding grain tilt. When retrieving the grain tilt, the information from the codebook linked to the voxel-stored ID is accessed. To enhance spatial locality during access, the solid textures containing the IDs are reorganized into a 1D array using Morton ordering [61].

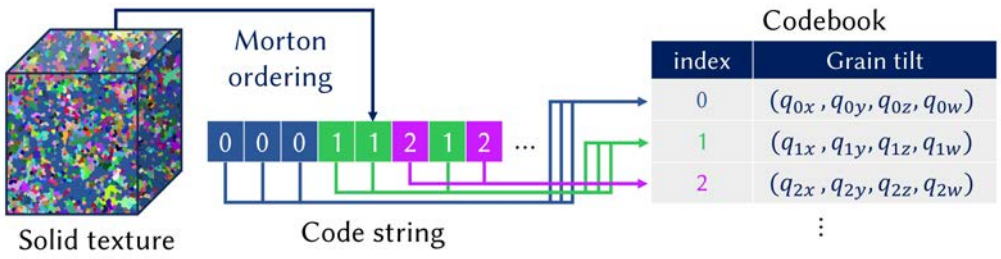

Fig. 4.10 Data structure representing the internal structure. A solid texture depicting the colloidal polycrystalline structure is represented by code string and a codebook

4.5 Modeling the Base Color

To represent the base color of opal, it is essential to analyze the phenomena of light absorption and scattering that occur within the opal. As described in **Sec. 3.2**, opals consist of silica spheres in which Si^{4+} is partially substituted with impurities, such as Al^{3+} and Fe^{3+}[26]. For instance, an increased concentration of Fe^{3+} causes the opal's base color to appear browner due to light absorption by Fe^{3+}. Impurities in the interstitial spaces of colloidal crystals contribute to both light absorption and scattering, while colloidal defects primarily cause light scattering.

In this study, the absorption and scattering of light within opals are represented using three parameters: the absorption coefficient σ_{a}, the Rayleigh scattering coefficient $\sigma_{\mathrm{s,\,r}}$, and the Mie scattering coefficient $\sigma_{\mathrm{s,\,m}}$.

The absorption coefficient σ_{a} accounts for light absorption by substituting ions or impurities within the colloidal crystal gaps. When light with an initial spectral radiance L_λ at a specific wavelength λ travels a distance t through a medium with an absorption coefficient $\sigma_{\mathrm{a},\lambda}$, the resulting spectral radiance L'_λ is given by:

$$L'_\lambda = L_\lambda \exp(-\sigma_{\mathrm{a},\lambda} t). \tag{4.6}$$

Absorption coefficients for various materials are readily available in research and public databases. However, the data cannot be used directly because the sampling interval in the wavelength direction is not standardized according to the measurement method. Therefore, the given absorption coefficient data are used by resampling using cubic spline interpolation.

The Rayleigh scattering coefficient models scattering caused by impurities in the gaps of colloidal crystals. Rayleigh scattering occurs when the particle size is significantly smaller than the wavelength of light, resulting in a scattering intensity that is highly

wavelength-dependent. The scattering coefficient for Rayleigh scattering $\sigma_{\mathrm{s,\,r},\lambda}$ at wavelength λ is expressed in the following equation:

$$\sigma_{\mathrm{s,\,r},\lambda} \propto \frac{1}{\lambda^4}. \tag{4.7}$$

Although $\sigma_{\mathrm{s,\,r},\lambda}$ can be computed from the number of particles per unit volume, in this study, the user specifies the scattering coefficient $\sigma_{\mathrm{s,\,r},\lambda=400}$ for $\lambda = 400$ nanometers, and $\sigma_{\mathrm{s,\,r},\lambda}$ are obtained at rendering by the following equation:

$$\sigma_{\mathrm{s,\,r},\lambda} = \sigma_{\mathrm{s,\,r},\lambda=400} \cdot \left(\frac{400}{\lambda}\right)^4. \tag{4.8}$$

The Mie scattering coefficient $\sigma_{\mathrm{s,\,m}}$ represents scattering by colloidal defects where the particle size is comparable to the wavelength of light. Unlike Rayleigh scattering, Mie scattering is not wavelength-dependent. Both scattering phenomena can be described under Lorenz-Mie theory. However, while the scattering distribution function for Rayleigh scattering is straightforward, Mie scattering involves complex approximations [7, 35, 17, 43], and no universally accepted formulation exists. In this study, the scattering coefficients for Rayleigh and Mie scattering are treated separately, with each type of scattering modeled as an independent medium.

For most opals, the medium's properties are assumed uniform, and the parameters σ_{a}, $\sigma_{\mathrm{s,\,r}}$, and $\sigma_{\mathrm{s,\,m}}$ are treated as constants. To introduce spatial variation in medium properties, these coefficients can be embedded into the voxels of the internal structure data and rendered using such techniques as Woodcock tracing [96].

4.6 Definition of External Shape

The external shape of the opal is defined using either a polygonal mesh or a patch of hyper-cubic Bézier surfaces [6]. A hyper-cubic Bézier surface $\boldsymbol{S}(u, v)$ is constructed using Bernstein basis functions:

$$\begin{aligned} B_i^3(u) &= \binom{3}{i} u^i (1-u)^{3-i}, \\ B_j^3(v) &= \binom{3}{j} v^j (1-v)^{3-j}, \end{aligned} \tag{4.9}$$

where i and j are indices, and $u, v \in [0, 1]$. The surface is determined by 16 control points $\boldsymbol{P}_{00}, \boldsymbol{P}_{01}, ..., \boldsymbol{P}_{33}$ and is expressed as:

$$\boldsymbol{S}(u, v) = \sum_{i=0}^{3} \sum_{j=0}^{3} \boldsymbol{P}_{ij} B_i^3(u) B_j^3(v). \tag{4.10}$$

In this study, the external shape of the opal is represented using eight bi-cubic Bézier surface patches. The positions of the endpoints of these patches are carefully adjusted to ensure differentiability at the boundaries between adjacent patches, maintaining a smooth and continuous surface.

4.7 Summary

The modeling method of the opal proposed in this chapter is summarized. First, the external shape of the opal is modeled using Bézier patches or polygon meshes. Subsequently, the following seven parameters are specified, and the internal structure of the opal is modeled by combining these parameters:

1. **Grain size of silica spheres constituting the opal:** d [nm]**.** The grain size of the silica spheres forming the opal is specified as a constant value. It is known that these spheres produce red at approximately 350 nm, green at around 250 nm, and blue at around 210 nm.

2. **Number of sites in the Voronoi diagram:** num_{s}**.** The number of sites, denoted as num_{s}, specifies the number of colloidal grains within the opal and is given as a constant integer. For an opal of the same volume, increasing the number of sites results in a finer pattern.

3. **Weight field of the Voronoi diagram:** W**.** The weight field W defines the timing of nucleation for colloidal grains and is represented as a 3D scalar field. The gradient of this field indicates the direction of crystal growth.

4. **Percolation threshold:** p**.** This parameter describes the likelihood of adjacent colloidal grains joining through sintering. It is specified as a constant value between 0 and 1, where higher threshold values increase the probability of grain combination.

5. **Absorption coefficient of impurities:** $\sigma_{\mathrm{a}}[\mathrm{m}^{-1}]$**.** This parameter influences the base of the opal. If the absorption coefficient is assumed uniform across the opal, it is defined as a 1D array of values for each wavelength. If it varies spatially, it is expressed as a 3D vector field. Because determining the distribution of absorption coefficients for impurities requires specialized knowledge, these values are obtained from a database.

6. **Scattering coefficient of Rayleigh scattering by impurities:** $\sigma_{\mathrm{s},r,\lambda=400}[\mathrm{m}^{-1}]$**.** This coefficient, specified at $\lambda = 400$nm, represents Rayleigh scattering caused by impurities in the gaps between colloidal grains. If the coefficient is uniform throughout

the opal, it is given as a constant; if it varies spatially, it is expressed as a 3D scalar field. Larger coefficients indicate stronger wavelength-dependent scattering, resulting in a murkier base color.

7. **Scattering coefficient of Mie scattering by impurities:** $\sigma_{\mathrm{s,\,m}}[\mathrm{m}^{-1}]$**.** This parameter reflects the degree of turbidity in the base color. When the scattering coefficient is uniform across the opal, it is defined as a constant. If spatial variation exists, it is expressed as a 3D scalar field. Higher values suggest more pronounced wavelength-independent scattering, contributing to a murkier appearance.

Chapter 5

Rendering

This study conducts a global illumination computation using the opal model defined in **Chap. 4** to achieve realistic visual simulation results. In this chapter, a global illumination model is selected for rendering, and a local illumination model is proposed to represent the optical properties of colloidal grains. In addition, a method for rendering the base color is discussed.

Section 5.1 introduces the path tracing method, and **Sec. 5.2** explains spectral rendering. **Sections 5.3** and **5.4** propose a local illumination model to capture the optical properties of opals. **Section 5.5** presents a method for utilizing RGB environment maps in spectral space, and **Sec. 5.6** discusses the importance sampling of wavelengths in spectral rendering. Finally, **Sec. 5.7** summarizes the contents of this chapter.

5.1 Path Tracing

The rendering equation [48] serves as the foundation for the global illumination computation:

$$L_{\mathrm{o}}(\boldsymbol{x}, \vec{\omega_{\mathrm{o}}}) = L_{\mathrm{e}}(\boldsymbol{x}, \vec{\omega_{\mathrm{o}}}) + L_{\mathrm{s}}(\boldsymbol{x}, \vec{\omega_{\mathrm{o}}}),$$

where $\boldsymbol{x}$ represents the position on the object surface in the model, $\vec{\omega_{\mathrm{o}}}$ is the direction of light emission, L_{o} is the emitted radiance, L_{e} is the self-emitted radiance, and L_{s} denotes the sum of reflected and transmitted radiance. The rendering equation can be expressed as an integral over the spherical surface $\mathcal{S}^2$, incorporating the bidirectional scattering distribution function (BSDF, f_{s}), which characterizes the local illumination model at the object surface:

$$L_{\mathrm{o}}(\boldsymbol{x}, \vec{\omega_{\mathrm{o}}}) = L_{\mathrm{e}}(\boldsymbol{x}, \vec{\omega_{\mathrm{o}}}) + \int_{\mathcal{S}^2} f_{\mathrm{s}}(\boldsymbol{x}, \vec{\omega_{\mathrm{i}}}, \vec{\omega_{\mathrm{o}}}) L_{\mathrm{i}}(\boldsymbol{x}, \vec{\omega_{\mathrm{i}}}) \left|\vec{\omega_{\mathrm{i}}} \cdot \vec{n}\right| \, d\omega_{\mathrm{i}}.$$

Here, $\vec{n}$ is the surface normal, and $\vec{\omega_{\mathrm{i}}}$ is the direction of incident light. This equation expresses radiance using an integral term and can be expanded as a Neumann series to include successive reflections. The path tracing method [48], a widely used Monte Carlo (MC) approach, is employed to evaluate this series. Details on the MC method, numerical computation of integrals using MC, and importance sampling in MC can be found in **Appendices A.3.1**, **A.3.2**, and **A.3.3**, respectively.

In the path tracing method, a ray is traced starting from the camera, following its path until it reaches a light source. In practical applications, an upper limit is set for the maximum number of reflections or transmissions. This process constructs a path with a finite number of reflections and transmissions. In this study, the number of reflections or transmissions of rays is referred to as the "bounces," while the maximum permissible number of bounces is termed the "total maximum bounces."

5.2 Spectral Rendering

Spectral rendering [14] is a method used to solve the rendering equations. In spectral rendering, the rendering equation is computed for each wavelength λ:

$$L_{\mathrm{o},\lambda}(\boldsymbol{x}, \vec{\omega_{\mathrm{o}}}, \lambda) = L_{\mathrm{e},\lambda}(\boldsymbol{x}, \vec{\omega_{\mathrm{o}}}, \lambda) + \int_{\mathcal{S}^2} f_{\mathrm{s},\lambda}(\boldsymbol{x}, \vec{\omega_{\mathrm{i}}}, \vec{\omega_{\mathrm{o}}}, \lambda) L_{\mathrm{i},\lambda}(\boldsymbol{x}, \vec{\omega_{\mathrm{i}}}, \lambda)(\vec{\omega_{\mathrm{i}}}, \vec{n}) d\omega_{\mathrm{i}}.$$

The term $L_{\mathrm{o},\lambda}(\boldsymbol{x}, \vec{\omega_{\mathrm{o}}}, \lambda)$, obtained by solving this equation, represents the spectral radiance—the radiance at a specific wavelength λ. To obtain an RGB image, the acquired spectral radiance distribution must be converted from spectral space to RGB space. This conversion is typically performed via the XYZ color space, and this study follows the same procedure. First, the spectral radiance $L_{\mathrm{o}}(\lambda)$ is transformed into the XYZ color system by multiplying with the XYZ color matching functions $\bar{x}$, $\bar{y}$, and $\bar{z}$, and then integrating over the wavelength range from λ_{min} to λ_{max}:

$$\begin{aligned}
X &= \frac{1}{\int_{\lambda_{\mathrm{min}}}^{\lambda_{\mathrm{max}}} \bar{y}(\lambda) d\lambda} \int_{\lambda_{\mathrm{min}}}^{\lambda_{\mathrm{max}}} \bar{x}(\lambda) L_{\mathrm{o}}(\lambda) d\lambda, \\
Y &= \frac{1}{\int_{\lambda_{\mathrm{min}}}^{\lambda_{\mathrm{max}}} \bar{y}(\lambda) d\lambda} \int_{\lambda_{\mathrm{min}}}^{\lambda_{\mathrm{max}}} \bar{y}(\lambda) L_{\mathrm{o}}(\lambda) d\lambda, \\
Z &= \frac{1}{\int_{\lambda_{\mathrm{min}}}^{\lambda_{\mathrm{max}}} \bar{y}(\lambda) d\lambda} \int_{\lambda_{\mathrm{min}}}^{\lambda_{\mathrm{max}}} \bar{z}(\lambda) L_{\mathrm{o}}(\lambda) d\lambda.
\end{aligned}$$

The resulting XYZ values are then converted to RGB values to obtain the final image. In this study, the conversion was applied to the D65 sRGB color space:

$$\begin{pmatrix} R \\ G \\ B \end{pmatrix} = \begin{pmatrix} 3.2409 & -1.5374 & -4.9861 \times 10^{-1} \\ -9.6924 \times 10^{-1} & 1.8760 & 4.1555 \times 10^{-2} \\ 5.5630 \times 10^{-2} & -2.0398 \times 10^{-1} & 1.0570 \end{pmatrix} \begin{pmatrix} X \\ Y \\ Z \end{pmatrix}.$$

Spectral rendering is well-suited for computing wavelength-dependent optical phenomena because it traces a path for each wavelength. This method was adopted for rendering the opal in this study due to its ability to handle wavelength-dependent effects, such as diffraction in colloidal crystals and Rayleigh scattering by fine particles.

Recent studies [4, 53] have explored rendering structural colors directly in RGB space. For example, **Fig. 5.1** shows results from implementing the method proposed by Belcour and Barla to compute thin-film interference in RGB space. These results demonstrate that structural coloring due to thin-film interference can be accurately observed and that wavelength-dependent optical phenomena can be computed without using spectral rendering.

Fig. 5.1 Thin-film interference computed with RGB rendering using Belcour and Barla's method [4]. In some cases, wavelength-dependent optical phenomena can be rendered without employing spectral rendering

However, it is known that when RGB rendering is used, errors in luminance occur as the number of bounces increases, compared to spectral rendering [20]. To verify this, a simple comparison experiment was conducted. For further details, refer to **Appendix A.4**. Due to the complex structure of the opal, the subject of this study, and the large number of reflections expected within it, rendering in RGB space was not attempted.

5.3 Rendering Play of Color

As demonstrated in **Sec. 3.3**, when light enters a colloidal crystal, it diffracts in a specific direction due to its periodic structure. This study adapts X-ray diffraction (XRD) theory, commonly used for the structural analysis of crystals, to the context of colloidal crystals. This adaptation enables the integration of the theory into the path tracing framework.

5.3.1 Ewald Construction

When a ray penetrates a colloidal crystal, multiple diffraction directions are considered, as depicted in **Fig. 3.4**c. To identify these directions efficiently, the Ewald construction, a technique rooted in XRD theory, was employed.

A point in the crystal with identical surroundings is referred to as a lattice point $\boldsymbol{R}$, whose expression can be represented by:

$$\boldsymbol{R} = l\boldsymbol{a} + m\boldsymbol{b} + n\boldsymbol{c},$$

where $\boldsymbol{a}$, $\boldsymbol{b}$, and $\boldsymbol{c}$ denote the basis vectors, and l, m, and $n \in \mathbf{Z}$. The basis vectors in fcc can be expressed by:

$$\boldsymbol{a} = \frac{d}{\sqrt{2}}(1,1,0),\ \boldsymbol{b} = \frac{d}{\sqrt{2}}(0,1,1),\ \boldsymbol{c} = \frac{d}{\sqrt{2}}(1,0,1),$$

where d denotes the diameter of the particles (**Fig. 5.2**a).

The reciprocal lattice fundamental vectors $\boldsymbol{a}^*$, $\boldsymbol{b}^*$, and $\boldsymbol{c}^*$ are defined as follows for the basis vectors:

$$\boldsymbol{a}^* = \frac{\boldsymbol{b}\times\boldsymbol{c}}{\boldsymbol{a}\cdot\boldsymbol{b}\times\boldsymbol{c}},\ \boldsymbol{b}^* = \frac{\boldsymbol{c}\times\boldsymbol{a}}{\boldsymbol{b}\cdot\boldsymbol{c}\times\boldsymbol{a}},\ \boldsymbol{c}^* = \frac{\boldsymbol{a}\times\boldsymbol{b}}{\boldsymbol{c}\cdot\boldsymbol{a}\times\boldsymbol{b}}.$$

Using the reciprocal basis vectors and $h, k,$ and $l \in \mathbf{Z}$, the reciprocal lattice vector $\boldsymbol{G}$ is expressed as:

$$\boldsymbol{G}_{hkl} = h\boldsymbol{a}^* + k\boldsymbol{b}^* + l\boldsymbol{c}^*.$$

The absolute value of the reciprocal lattice vector is related to the lattice spacing D_{hkl} of the lattice plane passing through $\boldsymbol{a}/h$, $\boldsymbol{b}/k$, and $\boldsymbol{c}/l$, as follows:

$$|\boldsymbol{G}_{hkl}| = \frac{1}{D_{hkl}}. \tag{5.1}$$

Next, the scattering vector $\boldsymbol{q}$ is defined as the vector that directs the wave vector of the incident wave $\boldsymbol{k}_0$ to the wave vector of the scattered wave $\boldsymbol{k}$ (**Fig. 5.2**b):

$$\boldsymbol{q} = \boldsymbol{k} - \boldsymbol{k}_0. \tag{5.2}$$

Note that the magnitude of the wave vector is $1/\lambda$. In XRD, it is known that crystal diffraction reaches its maximum [52] when:

$$\boldsymbol{q} = \boldsymbol{G}_{hkl}. \tag{5.3}$$

If the particles constituting the crystal are stacked in the $\boldsymbol{a}$, $\boldsymbol{b}$, and $\boldsymbol{c}$ directions with N_a, N_b, and N_c layers, respectively, it is known that in XRD, the scattering intensity I of the light incident on this crystal can be expressed as follows using the atomic scattering factor f:

$$I(\boldsymbol{q}) = |f(\boldsymbol{q})|^2\ |L_a(\boldsymbol{q})|^2\ |L_b(\boldsymbol{q})|^2\ |L_c(\boldsymbol{q})|^2.$$

Note that the individual terms $L_a(\boldsymbol{q})$, $L_b(\boldsymbol{q})$, and $L_c(\boldsymbol{q})$ can be written as:

$$\begin{aligned}
|L_a(\boldsymbol{q})|^2 &= \frac{\sin^2 N_a(\boldsymbol{q}\cdot\boldsymbol{a})\,\pi}{\sin^2(\boldsymbol{q}\cdot\boldsymbol{a})\,\pi},\\
|L_b(\boldsymbol{q})|^2 &= \frac{\sin^2 N_b(\boldsymbol{q}\cdot\boldsymbol{b})\,\pi}{\sin^2(\boldsymbol{q}\cdot\boldsymbol{b})\,\pi},\\
|L_b(\boldsymbol{q})|^2 &= \frac{\sin^2 N_c(\boldsymbol{q}\cdot\boldsymbol{c})\,\pi}{\sin^2(\boldsymbol{q}\cdot\boldsymbol{c})\,\pi}.
\end{aligned} \tag{5.4}$$

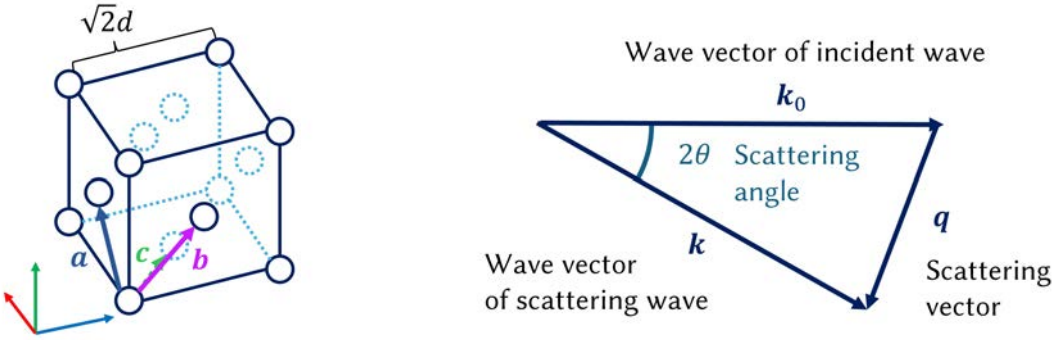

(a) (b)

Fig. 5.2 Vectors used in X-ray diffraction (XRD) theory. The basis vectors define the structure of a lattice and are used to describe the crystal structure (a). The scattering vector is defined as the vector that directs the wave vector $\boldsymbol{k}_0$ of the incident wave to the wave vector $\boldsymbol{k}$ of the scattered wave (b). The angle between $\boldsymbol{k}_0$ and $\boldsymbol{k}$ is referred to as the scattering angle, denoted by 2θ

The function expressed in the form $\sin^2 Nx/\sin^2 x$, as in **Eq. (5.4)**, is called the Laue function, and it exhibits a sharp peak as N increases. **Figure 5.3** shows the difference in the shape of the Laue function depending on the number of crystal layers. As the number of crystal layers increases, the spread of scattering intensity around the reciprocal lattice point becomes narrower, and the scattering peak can be regarded as a sharp node.

The Ewald construction [19] is an efficient method for identifying reciprocal lattice points that satisfy the conditions of **Eq. (5.3)** (**Fig. 5.4**a). Initially, the starting point of $\boldsymbol{q}$ is placed at the origin of the reciprocal lattice. Subsequently, in accordance with the definition of scattering vectors, $\boldsymbol{q}$ is drawn as a vector toward the origin of the reciprocal lattice, and $\boldsymbol{k}$ is represented as a vector that shares its starting point with $\boldsymbol{k}_0$ and its end point with $\boldsymbol{q}$. Then, a sphere is drawn with origin $-\boldsymbol{k}$ and radius $1/\lambda$, called the Ewald sphere. Because the wave vector has a magnitude $1/\lambda$, any point on the Ewald sphere surface can be the endpoint of $\boldsymbol{q}$. The diffraction maximum occurs when the conditions of **Eq. (5.3)** are satisfied, i.e., when a reciprocal lattice point exists on the surface of the Ewald sphere.

A sphere of radius $2/\lambda$ centered at the origin of the reciprocal lattice is referred to as a limiting sphere, and the geometrical properties of the Ewald sphere guarantee that the reciprocal points giving the diffraction maxima are within the limiting sphere. Therefore, the reciprocal lattice points satisfying **Eq. (5.3)** can only be found on the Ewald sphere surface among the reciprocal lattice points within the limiting sphere.

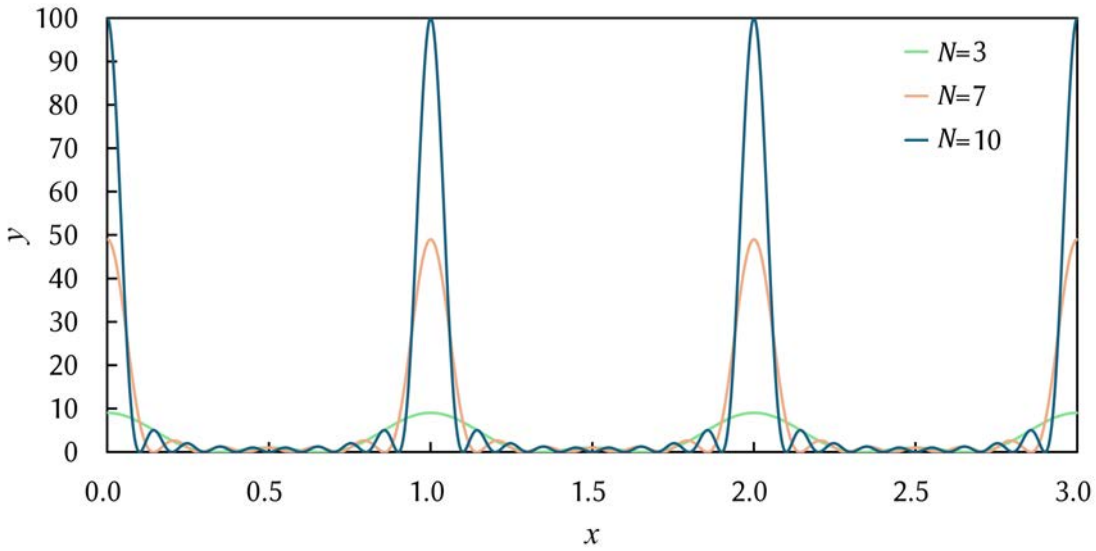

Fig. 5.3 Change in the shape of the Laue function as the number of layers N changes. The Laue function changes to a sharp-peaked shape as the number of layers increases

5.3.2 Computation of Diffraction

The Ewald sphere is used in path tracing to simulate the diffraction of light within colloidal crystals. In X-ray structure analysis, $\boldsymbol{k}_0$ and $\boldsymbol{k}$ are given, allowing analysis of the crystal's internal structure using **Eqs. (5.2)** and **(5.3)**.

In contrast, because the direction of the incident light $\boldsymbol{\omega}_\mathrm{i}$ of a ray toward a colloidal crystal and the internal structure of a colloidal crystal is already given, the outgoing direction $\boldsymbol{\omega}_\mathrm{o}$ of the ray is determined based on the conditions specified in **Eqs. (5.2)** and **(5.3)**. The wave vector $\boldsymbol{k}_0$ of the incident ray is derived from the given $\boldsymbol{\omega}_\mathrm{i}$, and whether the sum with the reciprocal lattice vector $\boldsymbol{G}_{hkl}$ exists on the Ewald sphere surface will determine whether the incident ray diffracts.

The wave vector $\boldsymbol{k}_0$ is derived from the given $\boldsymbol{\omega}_\mathrm{i}$ and the sum involving the reciprocal lattice vector $\boldsymbol{G}_{hkl}$ is evaluated to determine whether it lies on the Ewald sphere surface. This assessment establishes whether the incident ray diffracts. First, note that the wavelength is multiplied by $1/n_\mathrm{eff}$ because the colloidal crystal travels in a medium with an effective refractive index of n_eff. **Equation (5.2)** is reformulated with $\boldsymbol{\omega}_\mathrm{i}$ and $\boldsymbol{\omega}_\mathrm{o}$ to produce:

$$\boldsymbol{q} = \frac{n_\mathrm{eff}}{\lambda}\boldsymbol{\omega}_\mathrm{o} - \frac{n_\mathrm{eff}}{\lambda}\boldsymbol{\omega}_\mathrm{i}. \tag{5.5}$$

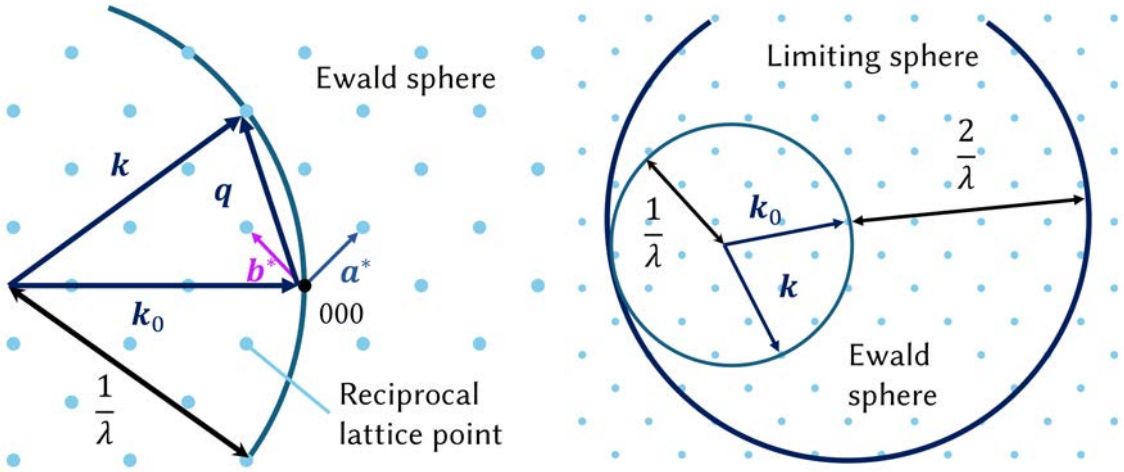

(a) Ewald sphere (b) Limiting sphere

Fig. 5.4 The Ewald construction. If a sphere of radius $1/\lambda$ is drawn in lattice space with the starting point of the wave vector at its center, the reciprocal lattice points with diffraction maxima always exist on the sphere surface (a). If a sphere of radius $2/\lambda$ is drawn with the origin at its center, the observable diffraction maxima are restricted to reciprocal lattice points that lie within this sphere (b)

Substituting **Eq. (5.3)** for **Eq. (5.5)**, the following expression is obtained:

$$\boldsymbol{G}_{hkl} = \frac{n_{\text{eff}}}{\lambda}\boldsymbol{\omega}_{\text{o}} - \frac{n_{\text{eff}}}{\lambda}\boldsymbol{\omega}_{\text{i}}, \tag{5.6}$$

$$\boldsymbol{\omega}_{\text{o}} = \boldsymbol{\omega}_{\text{i}} + \frac{\lambda}{n_{\text{eff}}}\boldsymbol{G}_{hkl}. \tag{5.7}$$

Incident light diffracts when $\boldsymbol{\omega}_{\text{o}}$, computed by **Eq. (5.7)**, satisfies the following:

$$|\boldsymbol{\omega}_{\text{o}}| = 1 \tag{5.8}$$

and its direction is $\boldsymbol{\omega}_{\text{o}}$.

In spectral rendering, because λ is limited to the visible light spectrum and the diameter of colloidal particles d is fixed when searching for the diffraction direction using **Eq. (5.7)**, it is practical to limit the number of $\boldsymbol{G}_{hkl}$ values by employing a limiting sphere. Because the range of the spectrum treated in this study is 360–830 nm, $\boldsymbol{G}_{hkl}$ values of 15 and 59 are considered sufficient when the opal grain size is 250 nm and 350 nm, respectively. In cases in which there exist multiple potential $\boldsymbol{\omega}_{\text{o}}$ values that satisfy **Eq. (5.8)**, one of the diffraction directions is stochastically selected at random, according to the magnitude of the Fresnel reflectance computed using half of the scattering angle θ.

Computing the absolute value of **Eq. (5.6)** and incorporating **Eq. (5.1)**, the following expression is obtained:

$$\frac{1}{D_{hkl}} = 2\frac{n_{\text{eff}}}{\lambda}\left(1 - \sin^2\theta\right)^{\frac{1}{2}}, \tag{5.9}$$

where θ is half of the scattering angle (**Fig. 5.2**b). If the angle of incidence of light entering a medium with an effective refractive index of n_{eff} from air is φ, Snell's law holds:

$$\sin \varphi = n_{\text{eff}} \sin \theta. \tag{5.10}$$

Derived from **Eqs. (5.9)** and **(5.10)** is none other than **Eq. (3.1)**.

5.3.3 Advantages of Using Ewald Construction

The primary advantage of using **Eq. (5.7)** with Ewald construction, as opposed to Bragg-Snell's law **Eq. (5.7)**, is that it requires less spatial computation. There are at most 59 possible directions in which visible light can diffract due to the regular structure within the opal. To determine whether light diffracts from these potential directions using Bragg-Snell's law, it is necessary to retain information on the lattice spacing D and the face normals of the diffracted surfaces for each diffraction candidate. In contrast, Ewald construction represents the candidate directions, i.e., reciprocal lattice points, as the sum of integer multiples of the reciprocal lattice basis vectors. Therefore, only the three reciprocal fundamental vectors are needed for the computational purpose, regardless of the number of diffraction candidates.

In a previous study [83], the Bragg-Snell law was used to compute the number of diffraction candidates. In this study, by employing Ewald construction, the problem is simplified to finding the intersection of a lattice point and a sphere in reciprocal lattice space, thus allowing all diffraction direction candidates to be treated efficiently.

5.4 Light Scattering/Absorption

Computation for the participating media is carried out using volume rendering. **Section 5.4.1** provides an overview of the volume rendering equations. The specific steps required to solve these equations are detailed as follows: **Sec. 5.4.2** discusses the sampling of distances, **Sec. 5.4.3** explains the determination of the media's behavior, and **Sec. 5.4.4** covers the sampling of phase functions.

5.4.1 Volume Rendering

The optical effects of the participating media, which contribute to the base color of the opal, can be determined by solving the volume rendering equation. The volume rendering

equation for the interval s is expressed as follows [45]:

$$L(\boldsymbol{x}, \vec{\omega}) = \int_0^s e^{-\tau(\boldsymbol{x}, \boldsymbol{x}')} \sigma_{\mathrm{a}} L_{\mathrm{e}}(\boldsymbol{x}')\, d\boldsymbol{x}' + \int_0^s e^{-\tau(\boldsymbol{x}, \boldsymbol{x}')} \sigma_{\mathrm{s}} \int_{\mathcal{S}^2} p(\boldsymbol{x}', \vec{\omega_{\mathrm{in}}}, \vec{\omega_{\mathrm{o}}}) L_{\mathrm{e}}(\boldsymbol{x}', \vec{\omega_{\mathrm{i}}})\, \omega_{\mathrm{i}} d\boldsymbol{x}' + e^{-\tau(\boldsymbol{x}, \boldsymbol{x} + s\vec{\omega_{\mathrm{o}}})} L(\boldsymbol{x} + s\,\vec{\omega_{\mathrm{o}}}, \vec{\omega_{\mathrm{o}}}),$$

where σ_{s} is the scattering coefficient, σ_{a} is the absorption coefficient, $\sigma_{\mathrm{e}} = \sigma_{\mathrm{s}} + \sigma_{\mathrm{a}}$ is the extinction coefficient, $\boldsymbol{x}'$ represents the incident position, and $p(\boldsymbol{x}', \vec{\omega_{\mathrm{in}}}, \vec{\omega_{\mathrm{o}}})$ is the phase function. $\tau(\boldsymbol{x}, \boldsymbol{x}')$ is the optical depth, which can be expressed as:

$$\tau(\boldsymbol{x}, \boldsymbol{x}') = \int_{\boldsymbol{x}}^{\boldsymbol{x}'} \sigma_{\mathrm{e}}(t)\, dt.$$

To compute the volume rendering equations using the path tracing method, paths are constructed by sampling the distance t through the participating media, determining the behavior of the media using the scattering coefficient σ_{s} and the absorption coefficient σ_{a}, and determining the ray direction based on the phase function p.

5.4.2 Sampling the Distance Through the Participating Media

This study uses woodcock tracing [96] to perform volume rendering of the participating media. First, the extinction coefficient σ_{e} is obtained using the scattering coefficients $\sigma_{\mathrm{s,\,r}}$ for Rayleigh scattering, $\sigma_{\mathrm{s,\,m}}$ for Mie scattering, and σ_{a} for absorption, as defined in **Sec. 4.5**:

$$\sigma_{\mathrm{e}} = \sigma_{\mathrm{s,\,r}} + \sigma_{\mathrm{s,\,m}} + \sigma_{\mathrm{a}}.$$

Using the extinction coefficient σ_{e} and a uniform random number $\xi \in [0, 1)$, the distance t to the interaction point is sampled:

$$t = -\frac{\ln(1 - \xi)}{\sigma_{\mathrm{e}}}.$$

5.4.3 Determining the Behavior of the Media

Next, the behavior of the media at the interaction point is determined. First, the scattering albedos $\mathit{\Lambda}_{\mathrm{r}}, \mathit{\Lambda}_{\mathrm{m}}$ for Rayleigh and Mie scattering are computed:

$$\mathit{\Lambda}_{\mathrm{r}} = \frac{\sigma_{\mathrm{s,\,r}}}{\sigma_{\mathrm{e}}},$$
$$\mathit{\Lambda}_{\mathrm{m}} = \frac{\sigma_{\mathrm{s,\,m}}}{\sigma_{\mathrm{e}}}.$$

Then, using uniform random numbers $\xi \in [0, 1)$, the interaction is processed as follows:

- Rayleigh scattering if $\xi \in [0, \Lambda_{\mathrm{r}})$,
- Mie Scattering if $\xi \in [\Lambda_{\mathrm{r}}, \Lambda_{\mathrm{r}} + \Lambda_{\mathrm{m}})$,
- Absorption if $\xi \in [\Lambda_{\mathrm{r}} + \Lambda_{\mathrm{m}}, 1)$.

In the case of scattering, the next ray direction is determined by sampling the phase function, as discussed in the next section. In the case of absorption, ray tracing is terminated, and the ray radiance is set to zero.

5.4.4 Sampling of Phase Function

When scattering occurs, the direction of the next ray is determined by sampling the phase function. The phase function is sampled using importance sampling.
(1) In the case of Rayleigh scattering. The Rayleigh scattering phase function $p_{\mathrm{R}}(\theta)$ can be expressed as follows, where the spherical coordinates (θ, ϕ) in the ray direction $\vec{\omega}$ define the zenith direction:

$$p_{\mathrm{R}}(\theta) = \frac{1}{4\pi}\frac{3}{4}\left(1 + \cos^2\theta\right).$$

When sampling the Rayleigh scattering phase function, Frisvad's method [24] for importance sampling is employed. Assuming uniform random numbers $\xi_1, \xi_2 \in [0, 1)$, importance sampling is performed as follows:

$$u = -\left[2\left(2\xi_1 - 1\right) + \left\{4\left(2\xi_1 - 1\right)^2 + 1\right\}^{\frac{1}{2}}\right]^{\frac{1}{3}},$$
$$(\theta, \phi) = \left(\cos^{-1}\left(\frac{u-1}{u}\right), 2\pi\xi_2\right).$$

The necessary information to determine the next direction of travel is the sine and cosine of θ and ϕ. Therefore, instead of computing the inverse cosine of θ, the following approach is used:

$$\cos\theta = \frac{u-1}{u}, \sin\theta = \sqrt{1 - \cos^2\theta},$$
$$\vec{\omega} = \left(\sin\theta\cos\phi, \sin\theta\sin\phi, \cos\theta\right).$$

(2) In the case of Mie scattering. The phase function of Mie scattering exhibits a complex shape that depends on the particle diameter. As a result, in CG, it is often approximated by simpler functions during computations. Models used to approximate Mie scattering include Schlick's phase function [7]:

$$p(\theta) = \frac{1 - k^2}{4\pi(1 + k\cos\theta)^2},$$

Henyey-Greenstein's function [35]:

$$p(\theta) = \frac{1}{4\pi} \frac{1 - g^2}{(1 + g^2 - 2g\cos\theta)^{2/3}},$$

and Draine's function [17]:

$$p(\theta) = \frac{1}{4\pi} \frac{1 - g^2}{(1 + g^2 - 2g\cos\theta)^{2/3}} \frac{1 + \alpha\cos^2\theta}{1 + \alpha(1 + 2g^2)/3},$$

where k, g, and α are parameters that define the shape of the phase function. Jendersie and d'Eon proposed a method to approximate phase functions more accurately than those methods by combining the Draine and Henyey-Greenstein functions [43]. However, this method was developed for the phase function of water particles in air, which differs from the phase function of silica spheres addressed in this study. In the present work, the scattering distribution is pre-computed using Python's PyMieScatt package [81], stored as a look-up table, and used as a reference for rendering.

5.5 Upsampling of RGB Environment Map

Light sources used in spectral rendering must be defined in terms of their spectral distributions. However, creating an environment map from measured data requires specialized equipment to capture ambient light, and using such data as an environmental map demands significant memory. To address this, the environment maps captured as RGB images are upsampled in the wavelength direction at runtime and used as a light source in this study.

While methods such as those by Meng et al. [59], Otsu et al. [67], and Jakob and Hanika [42] are commonly used to upsample from RGB color space to spectral space, this study adopts the classical approach of Smits [76] due to the minimal computational overhead it requires during rendering. It is important to note that this method is applied to texture upsampling rather than light source upsampling.

5.6 Importance Sampling of Wavelengths

Spectral rendering samples wavelengths randomly and converges more slowly than conventional path tracing. Several methods have been proposed to address this challenge. For example, Wilkie et al. [93] introduced an efficient method for spectral rendering, particularly for the volume rendering of participating media, by constructing paths of appropriate wavelengths and computing the contributions of all wavelengths using multiple importance sampling.

However, this approach is not well-suited for phenomena whose direction of reflection is uniquely determined for each wavelength, such as light refraction, and similarly, the diffraction of light by colloidal crystal grains studied in this research also forms paths where the contribution of specific wavelengths is dominant.

Consequently, the proposed method performs importance sampling of wavelengths along the spectral distribution of the environment map. First, the RGB environment map is upsampled into spectral space using Smits' method [76] to obtain the spectral distribution. This distribution is then normalized over the visible light range and used as the probability density function for importance sampling of wavelengths. While the inverse transform method is a potential approach for focused sampling, it requires $O(\log n)$ computations for sampling when there are n wavelength channels. For this reason, the proposed method used Walker's aliasing method [88] for importance sampling. This method allows for efficient sampling of n channels in $O(1)$ time using an alias table (in **Fig. 5.5**) and two uniform random numbers. However, this method is ineffective for boundaries described as "Dirac interfaces," as discussed in that paper, i.e., boundaries where sampling is highly wavelength-dependent, such as in light refraction. This study did not employ this method because the boundary between air and opal is a Dirac interface, causing wavelength-dependent refraction of light and because the diffraction of light by colloidal grains forms light paths where the contribution of a particular wavelength dominates.

5.7 Summary

In this study, spectral rendering via path tracing is employed to generate images of opals. The light source is represented by an upsampled environment map.

Due to the sharp peaks in diffraction caused by light interacting with colloidal grains, the diffraction direction is computed dynamically. This involved determining a point on a sphere based on the Ewald construction, adapted from XRD theory, within the visible wavelength range. The base color of the opal is modeled using volume rendering of the participating media, implemented through Woodcock tracing.

Inside the opal, the first step is to determine the intersections of the ray with the Voronoi boundaries and the intersection of the ray with the involved medium. The material properties are then computed at the nearest intersection point. If the intersection occurs at a Voronoi boundary, light diffraction is computed. If the intersection occurs within the involved medium, Mie scattering, Rayleigh scattering, or light absorption is stochastically selected and computed.

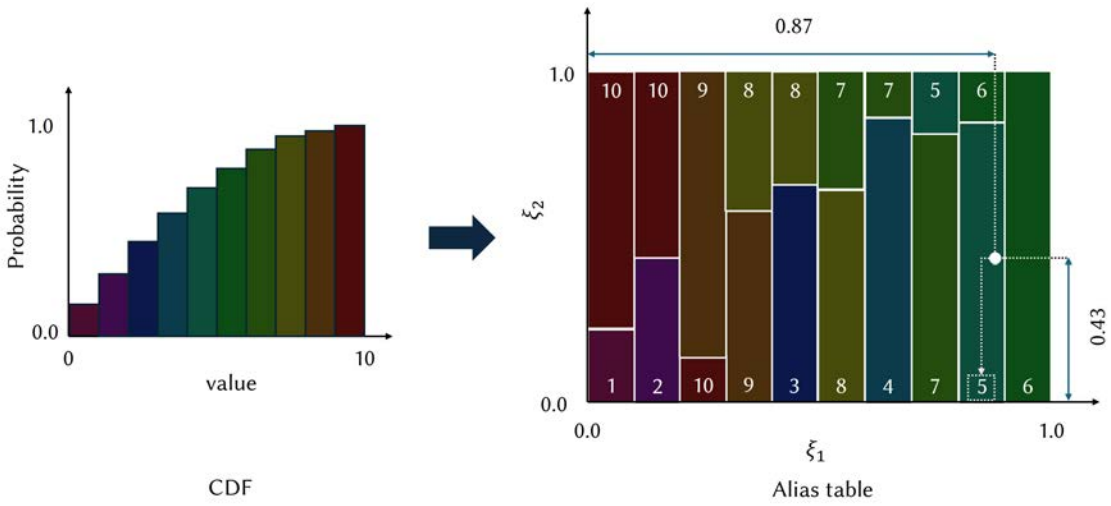

Fig. 5.5 Example of importance sampling using the Alias table. When one wants to obtain values according to a certain probability density function, the inverse transform method is generally used. In contrast, the Alias method creates an Alias table once, and thereafter, the values can be obtained by $O(1)$ using two independent uniform random numbers $\xi_1, \xi_2 \in [0, 1)$. In the case $\xi_1 = 0.87, \xi_2 = 0.43$, 5 is chosen by referring to the Alias table, as shown in the figure

Chapter 6

Results and Discussions

This chapter presents the results of the study and examines the validity and applicability of the proposed methodology. **Section 6.1** outlines the study's findings, while **Sec. 6.2** provides a detailed discussion.

The proposed method was implemented in C $++$ and CUDA and executed on a computer with an Intel Core i9-10000X, 128GB of RAM, and an NVIDIA GeForce RTX 3070 graphics card. The resolution of the solid texture is 512^3. Refer to **Table 6.1** for the other parameter values used in the modeling of each example. Note that num_s denotes the number of sites of the additively weighted Voronoi diagram initially placed and $num_{\boldsymbol{G}}$ the number of reciprocal grid points. Spectral rendering was performed using 48 color channels sampled at 10 nm intervals from 360 nm to 830 nm. The maximum number of bounces was set to 64. Each example was rendered with 4,096 samples per pixel and a resolution of $1,440 \times 1,080$. The lighting environment was modeled using an environment map sourced from a dancing_hall_4k.exr image available under the CC0 license on Poly Haven [101]. This map was upsampled from an RGB color space to a spectral space to serve as a light source.

Table 6.1 Parameters and running time of the visual simulation of each image, where num_{s} denotes the number of sites of the additively weighted Voronoi diagram initially placed, p the probability of the existence of edges when computing bond percolation, num_{c} the number of clusters at the end of modeling, t_{m} the running time of modeling, d the diameter of the silica sphere, $num_{\boldsymbol{G}}$ the number of reciprocal grid points $\boldsymbol{G}_{hkl}$ in the limiting sphere, and t_{r} the running time of rendering. The resolution of each image is $1,440 \times 1,080$, and the maximum bounce of each path is 64, sampled in $4,096$ spp

Fig.	num_{s}	p	num_{c}	t_{m} [sec]	d [nm]	$num_{\boldsymbol{G}}$	t_{r} [min]
6.1 (a)							32.42
6.1 (b)							32.37
6.1 (c)	27,000	0.32	8,567	17.18	280	27	32.28
6.1 (d)							32.30
6.1 (e)							32.25
6.2 (a)	27,000	0.22	9,989	17.51	210	15	27.17
6.2 (b)	27,000	0.22	9,907	17.45	250	15	28.68
6.2 (c)	27,000	0.22	10,056	17.57	350	59	43.28
6.3 (a)	262,144	0.26	66,643	20.69	250	15	4.827
6.3 (b)	27,000	0.12	21,018	16.86	260	27	10.87

6.1 Results

This section presents the execution results of this study; **Section 6.1.1** presents the rendering results and **Sec. 6.1.2** reports the execution time.

6.1.1 Representation of Opal

Figure 6.1 empirically proves the plausibility of the visual simulation with the proposed method, rotating the display stand in increments of 5°. As the stand is rotated, the color and pattern inside the opal change, and it can be confirmed that the opal represents play of color.

Figure 6.2 shows the results of a visual simulation by changing the grain size of the silica spheres. According to Gao et al. [26], colloidal crystals show blue, green, and red color effects when the silica sphere is 207 nm, 249 nm, and 350 nm, respectively. The visual simulation results are consistent with the report.

Figure 6.3 shows the results of reproducing black opal and fire opal using Al^{3+} and Fe^{3+} ions, respectively, as absorption coefficients for their base color. The opal was modeled based on **Figs. 3.2**b and **3.2**c, and the results indicate that the base color of opals is visually plausible.

6.1.2 Performance

Table 6.1 summarizes the runtime required to obtain the results of the visual simulation. Modeling took approximately 17–21 seconds, whereas rendering required about 11–43 minutes. The case in **Fig. 6.3**a for fire opal using Al^{3+} deserves special attention: the num_{s} initially placed is 10 times greater than in the other cases, though t_{m} is not much different. Conversely, t_{r} is scaled to $num_{\boldsymbol{G}}$, but it is significantly reduced because $\sigma_{\mathrm{a},\lambda}$ is large. This suggests that ray iterations are more likely to be terminated in preliminary stages.

6.2 Discussions

Based on the results, this section discusses the validity, applicability, and limitations of the methodology.

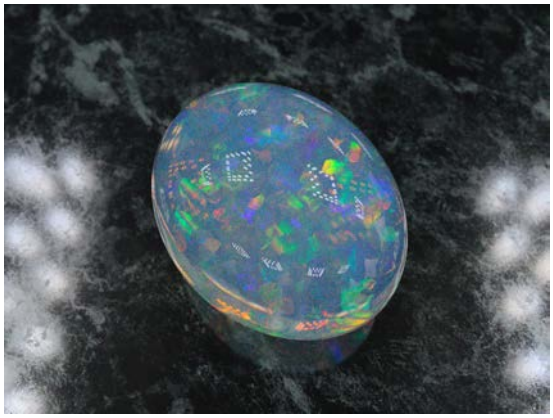

(a) 0°

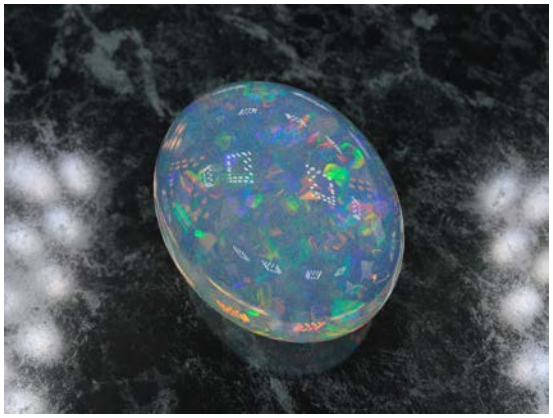

(b) 5°

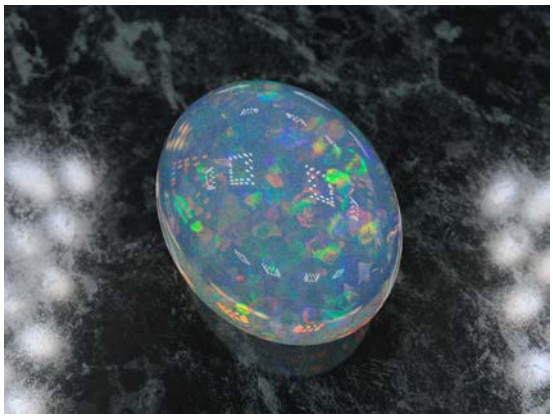

(c) 10°

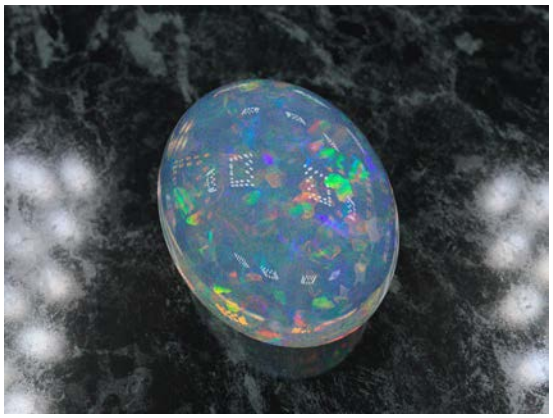

(d) 15°

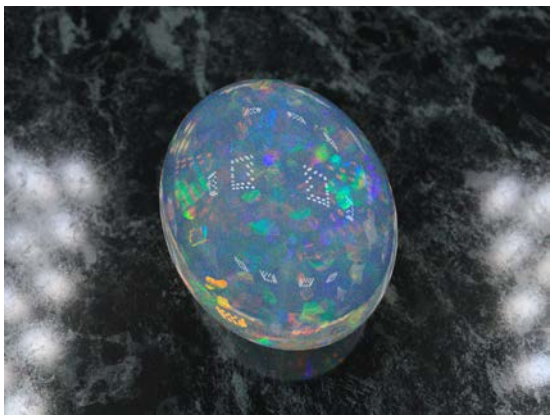

(e) 20°

Fig. 6.1 Results of visual simulation of opal with the proposed method. The display stand was rotated by 5°. The color and pattern of the opal changed as the stand was rotated

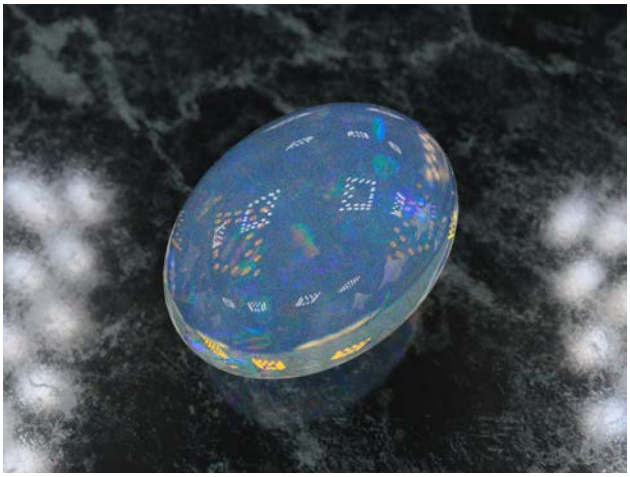

(a) 210 nm

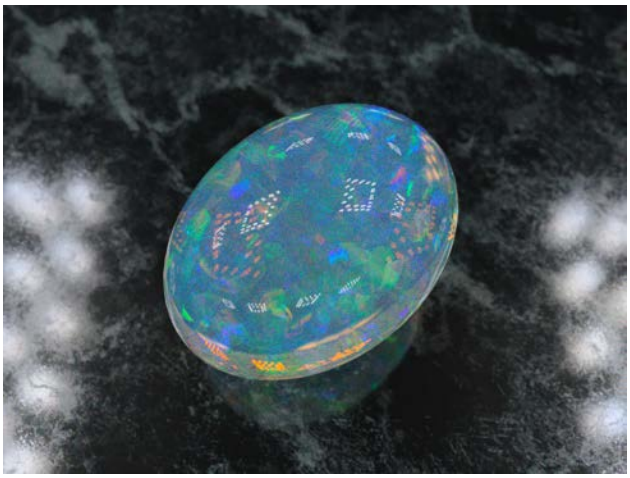

(b) 250 nm

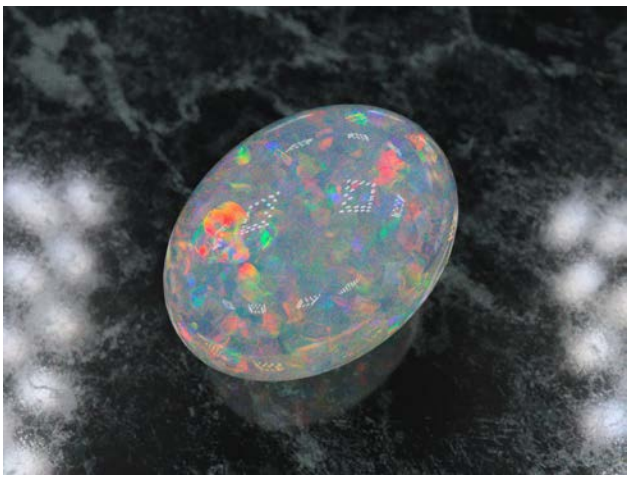

(c) 350 nm

Fig. 6.2 The color change of the emitted play of color: Blue at 210 nm, green at 250 nm, and red at 350 nm, and this agrees with the report by Gao et al. [26]

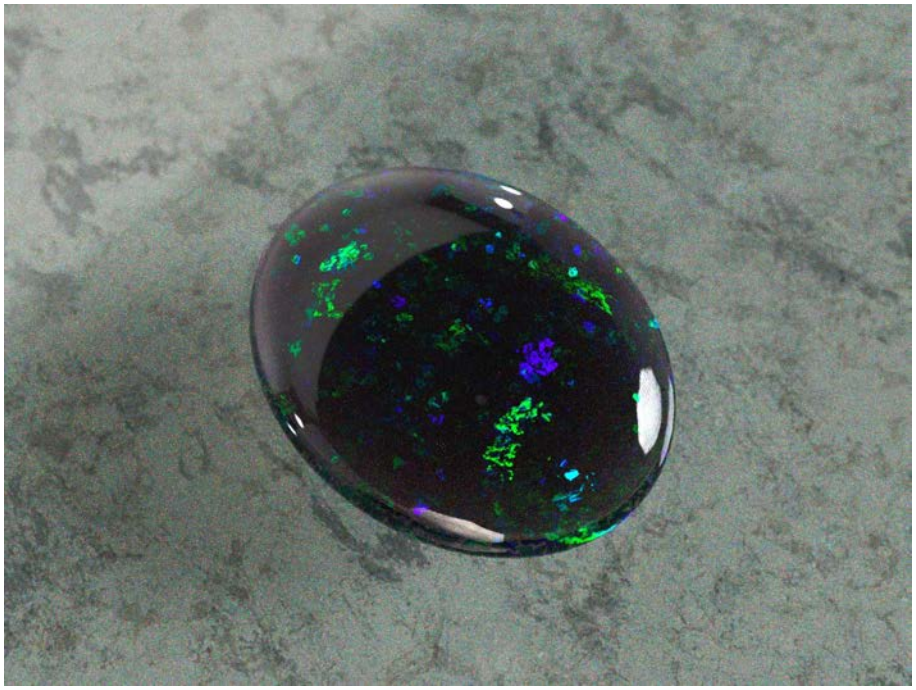

(a) Black opal

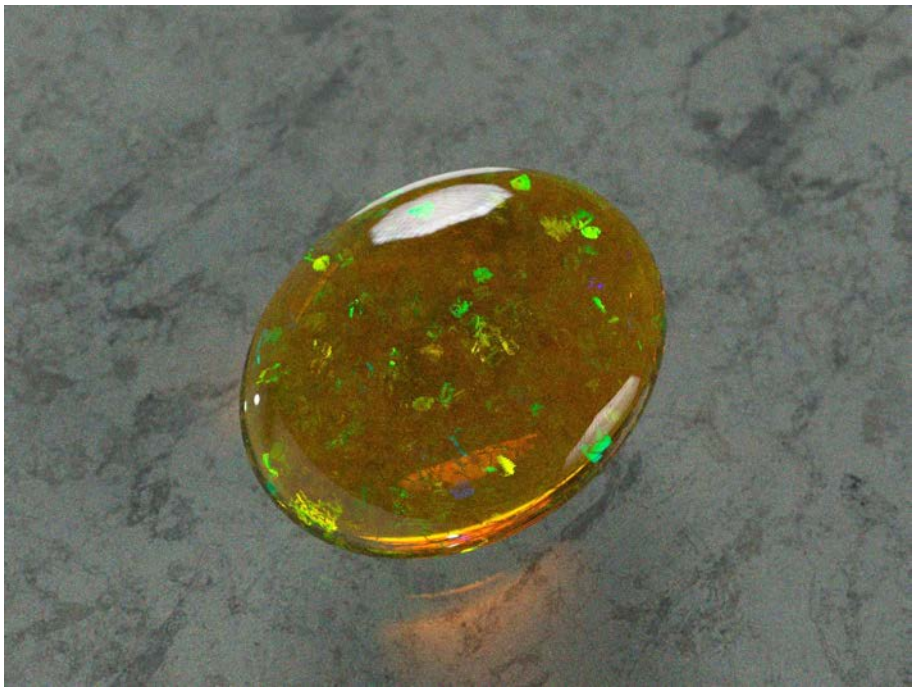

(b) Fire opal

Fig. 6.3 Representation of black opal and fire opal. Figs. 3.2b and 3.2c were used as reference. The absorption coefficients of Al^{3+} ions for black opal and Fe^{3+} ions for fire opal were used

6.2.1 Internal Structure Model

In this study, weighted Voronoi tessellation was employed to reproduce the internal structure of opals. While Voronoi tessellation is considered effective in approximating the process of opal formation, it tends to generate simpler patterns compared to real opals. Because fine fluctuations are observed at the grain boundaries of real opals, incorporating these fine irregularities into the Voronoi boundaries may enable the reproduction of more realistic patterns.

A Bernoulli percolation model was employed to approximate colloidal polycrystalline grain growth from the viewpoint of computational efficiency. However, real grain growth entails complex parameters, such as temperature, pressure, and grain boundary energy [71], suggesting the potential re-examination of using a Bernoulli distribution to determine edge existence probability. In the field of materials engineering, studies have been conducted to simulate the self-organization of colloidal crystals [16], although the computational scale is currently limited. Advancements in these studies will enhance the accuracy of internal structure modeling.

Each opal has an inherent complex internal structure, and identifying the internal structure of a real opal requires the microscopic observation of irreversible cut surfaces. Consequently, it is difficult to verify the validity of the internal structure against real opals. To assess quantitatively the effectiveness of the method, further detailed investigations would be imperative through collaboration with experts in the fields of crystallography and materials engineering.

6.2.2 Computational Model of Diffraction

In this study, the diffraction direction of incident light on a colloidal crystal is computed online using the Ewald construction, providing an effective approach for materials that exhibit sharp diffraction peaks, potentially due to crystal structures. However, as indicated in Table 6.1, the computational time required for rendering increases linearly with the number of reciprocal grid points in the limiting sphere, leading to decreased efficiency. For materials with numerous or a wide spread of diffraction peaks, it is more efficient to research pre-computed results.

In this study, although all internal structures were assumed fcc for simplicity, it is known that a part of the internal structure of real opal is replaced by hcp. Accounting for this effect would enable the computation of a more accurate diffraction.

6.2.3 Improved Efficiency of Global Illumination Computation

This study used Monte Carlo path tracing, which takes longer to converge while requiring less memory at runtime. The goal of this study is the reproduction of the internal structure of opals and the proposal of a local illumination model within the opal; therefore, the optimization of global illumination computations is not addressed.

However, reducing runtime is a goal, potentially achievable by incorporating photon mapping [44], path guiding [62], or more efficient spectral rendering techniques [93].

6.2.4 Evaluation of the Validity of This Study

Visual simulation results are often validated by comparing them with results from an alternative approach, such as by comparing theoretical values when a measurement-based model is used or, conversely, by confirming that a theoretically constructed model agrees with measured values of the actual object. In many cases, the validity of the model is verified by comparing it with the results of an approach other than that used in the study. Considering the model proposed in this study, the model of the internal structure is based on noise-based artificial modeling, the spectrum of the base color is a phenomenological model, as it uses values directly from a database, and the optical computation is a physical model derived from XRC theory.

As shown in **Sec. 6.2.1**, it is difficult to obtain the internal structure of an opal through measurement or simulation. The validation of this study is limited to the reproduction of characteristic optical phenomena, as described in **Sec. 6.1.1**. A user study following the method of Nagata et al. [64] could further reinforce the plausibility of the rendering results.

6.2.5 Guidelines for Modeling

As described in **Sec. 4.7**, seven parameters are used to model opals in this study. However, rendering with this method takes several tens of minutes per image, and thus, it takes time to obtain feedback. Therefore, guidelines are provided for adjusting the parameters proposed in this study to achieve the desired opal model.

Of the seven parameters, one is related to the color of the play of color, three to the pattern of the play of color, and three to the base color. First, the color of the play of color can be adjusted by modifying the particle size of the silica spheres, d. As shown in **Eq. (3.1)**, by determining the grain size, it is possible to identify the color with the longest wavelength among the play of color emitted by the opal. If the composition of

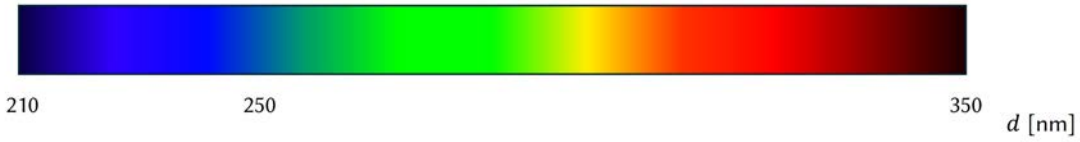

Fig. 6.4 The relationship between colloidal grain size and the color change emitted by the colloidal grains is depicted. Using Bragg-Snell's law, the correspondence between colloidal grain size and the color with the longest wavelength among the play of colors emitted by the colloidal grains can be computed. When modeling real opals on a computer in this study, if the colloidal grain size information is unknown, this correspondence can be inferred from this relationship

the actual opal is already known, the grain size can be directly used; otherwise, it can be adjusted visually, as shown in **Fig. 6.4**, as the grain size and the color of the play of color are mapped by **Eq. (3.1)**.

Next, the parameters related to the pattern include the number of sites in the Voronoi diagram num_{s}, the weight field of the Voronoi diagram W, and the percolation threshold p. The number of sites in the Voronoi diagram is estimated from the size of the colloidal crystal grains and the volume of the opal by observing a real opal. The weight field W of the Voronoi diagram is a parameter related to the timing of the nucleation of colloidal grains on the opal and consequently determines the sizes of the bends at the Voronoi boundary. To determine the timing of colloidal grain nucleation accurately, complex computations must be performed on the colloidal motion in solution, which, in this study, is weighted using appropriate Perlin noise. Finally, the percolation threshold p represents the ease with which neighboring grains are connected by sintering: at $p = 0$, no grains are connected to the surrounding grains, and at $p = 1$, they are fully connected. The percolation model has a critical point, beyond which the system's behavior changes and infinite clusters form. Based on the findings of this study, plausible results are often obtained for values of $0 < p < 0.3$. **Figure 6.5** illustrates the internal structure when the percolation threshold is varied, while the number of sites and the weight field of the Voronoi diagram remain fixed.

Finally, three parameters are related to the base color: the absorption coefficient σ_{a} of impurities, the scattering coefficient $\sigma_{\mathrm{s,\,r}}$ for Rayleigh scattering, and the scattering coefficient $\sigma_{\mathrm{s,\,m}}$ for Mie scattering. Because estimating the absorption coefficient spectra is challenging, a publicly available database of ion absorption spectra from research institutes is directly used.

The influence of these parameters can be confirmed not through spectral rendering using the path tracing method employed in this study, but through simple volume rendering,

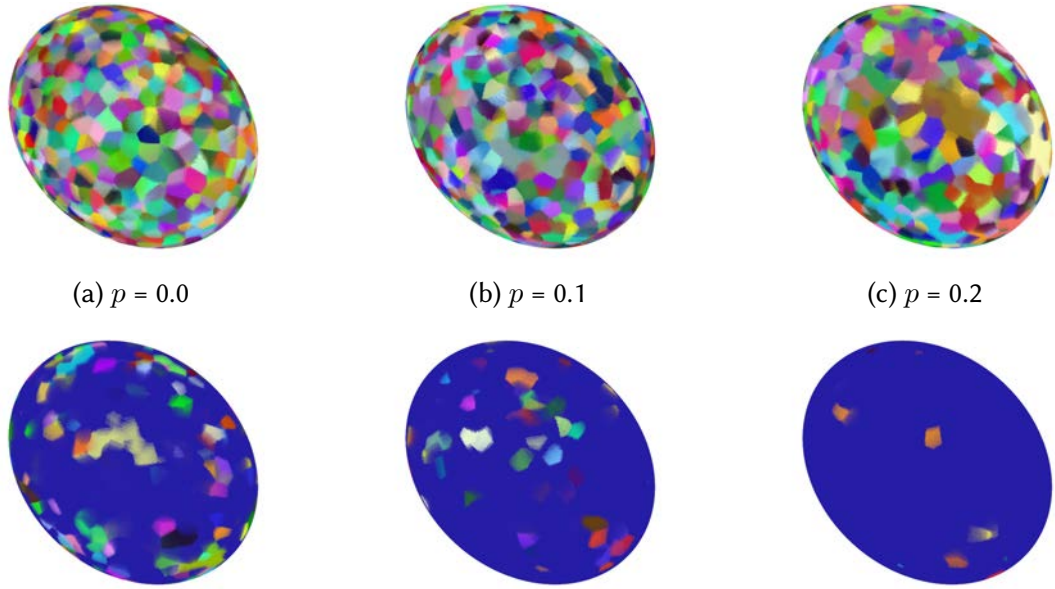

(a) p = 0.0 (b) p = 0.1 (c) p = 0.2

(d) p = 0.3 (e) p = 0.4 (f) p = 0.5

Fig. 6.5 Change in internal structure as the percolation threshold p is varied. The percolation threshold was increased from 0.0 to 0.5, while the number of sites num_s and the weight field W in the Voronoi diagram were kept fixed. As the threshold increases, the sizes of the clusters change. The Bernoulli percolation on the 3D Voronoi diagram proposed in this study reaches a critical point for values of p between 0.2 and 0.3, and for higher values, the formation of infinitely many clusters becomes apparent

as demonstrated in the application shown in **Fig. 6.6**. The application obtained rendering results by assigning the same color to areas within a solid texture that represents the opal's internal structure, and then performing volume raycasting on it (**Fig. 6.6** a). The intersections of the ray with the opal's exterior were determined, and the voxels the ray passed inside the opal were obtained using Bresenham's line algorithm. For the visualization of Perlin noise, the intersection points of the rays with the axis-aligned bounding box surrounding the opal were determined, and Perlin noise values were obtained and rendered as the rays advanced by small intervals within the section where the rays intersected the bounding box (**Fig. 6.6** b). Therefore, when modeling real opals using this study, the combination of parameter values can be narrowed down by first determining the pattern via pre-visualization and then determining the color by computing high-load path tracing.

6.2.6 Applicability of the Proposed Method

Guy et al.'s method [33] has been applied to the design of the external shape of single-crystal gemstones. While this study endeavors to apply the method to texture design using

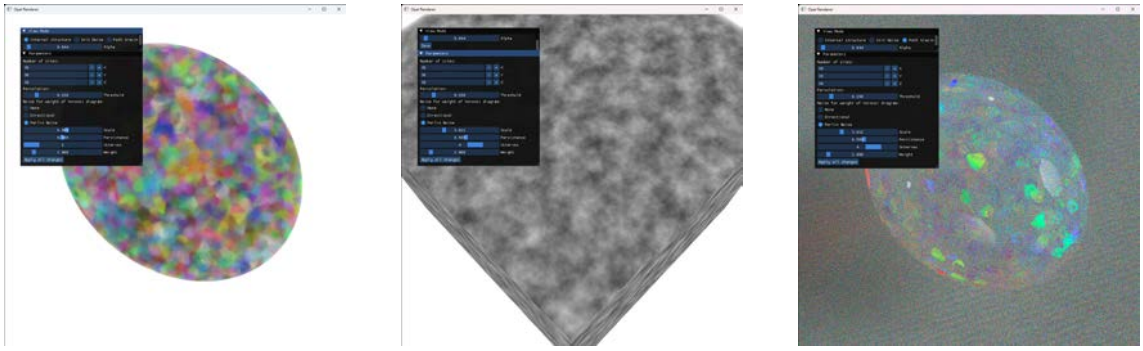

(a) (b) (c)

Fig. 6.6 An example of an environment for modeling using the proposed method. The parameters of the opal's internal structure can be interactively adjusted efficiently through a simple volume ray-casting before rendering the output image with the path tracing method. The application in the figure uses simple volume ray-casting to model the internal structure interactively (a) and then it transfers the information to the path tracer to obtain the final image (c). The addition of weight field visualization (b) enables the intuitive manipulation of parameter values

CAD, enabling external shapes to be defined with Bézier patches, it is difficult to achieve this at the current frame rate. A fundamental review of the rendering method is thus necessary to enable interactive, physically-based rendering for jewelry design. Although designing jewelry interactively using this research is challenging, it may serve as a pre-rendering tool for jewelry design. For example, **Fig. 6.7** shows the result of rendering an opal combined with a ring base using the proposed method.

Adopting a physically motivated approach to modeling opals is anticipated to enhance the applicability and impact of this research significantly. This research may also prove useful for the fabrication of synthetic opals. Because opals are valuable as gemstones, synthetic opals are manufactured at the product level. In the process of creating synthetic opals, some companies create brightly colored synthetic opals with blue or pink base colors, which do not occur naturally, by pouring dye into the gaps between the colloidal crystals during the fixing process [54]. In addition, because this research is based on physically motivated modeling, it may be possible to simulate the finished product using the size of the colloidal crystal grains, the absorption spectrum of the dye, and other factors. **Figure 6.8** shows the results of rendering synthetic opals using the absorption spectra of light blue and pink dyes. This research is not limited to modeling the internal structure of a synthetic opal but can also be used to simulate changes in appearance due to the external shape, as the external shape can be freely defined using polygons and Bézier patches. **Figure 6.9** shows a rendering of an opal with the Bézier patches of the *Utah teapot* as the external shape. However, when applying these research results to the

Fig. 6.7 The result of rendering an opal modeled using the proposed method on a ring base. This research may be applied as a pre-rendering tool for jewelry design

fabrication of synthetic opals, some correspondence between the actual manufacturing environment and the parameters of these research results will be necessary, particularly for those related to the pattern of the play of color.

As a more challenging application that takes advantage of the fact that this research employs physics-based modeling, it is intriguing to estimate the internal structure of real opals using the proposed method. Many pairs of internal structure models and their rendering results can be generated, enabling the exploration of the feasibility of utilizing these datasets as training data for machine learning to estimate the internal structure of real opals. Furthermore, given that research on optimization using differentiable Voronoi diagrams [98] has been conducted, combining this research with differentiable rendering may allow for the estimation of internal structures as well.

(a) Result using light blue dye data

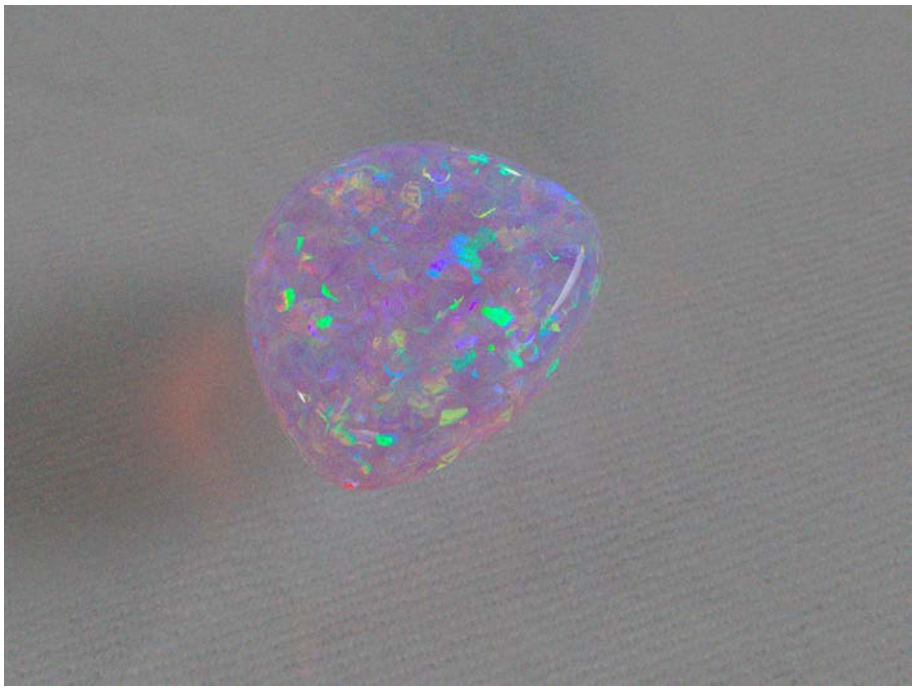

(b) Result using pink dye data

Fig. 6.8 Rendering of synthetic opals using the absorption spectrum of dye. Some synthetic opals can be created in colors that do not occur in nature by pouring dye into the gaps between the colloidal crystal grains during the fixing process

(a) Result using light blue dye data

(b) Result using pink dye data

Fig. 6.9 Rendering of a synthetic opal with the external shape of the *Utah teapot*. The teapot was modeled to fit into a cube with each side measuring 2 cm. This research is not limited to modeling the internal structure of the synthetic opal but can also be used to simulate the effect of the external shape on its appearance

Chapter 7

Conclusion

This study proposed a method for achieving a realistic visual simulation of opals. First, the physical properties of opals were investigated, and the essential elements for visual simulation were identified. The investigation revealed that modeling the 3D stacking structure of silica spheres, developing a model to compute light diffraction for colloidal grains, and reproducing the base color are necessary. Based on these findings, a modeling method for the internal structure of opals was proposed. The internal structure was expressed in terms of colloidal grains using weighted Voronoi tessellation and the Bernoulli percolation model. The base color of the opal was reproduced by computing the absorption and scattering of impurities within the opal. Finally, a method for modeling opals was proposed, involving the adjustment of seven parameters: one for the color of the play of color, three for the pattern, and three for the base color. In Addition, a computation method for determining the direction in which visible light diffracts from colloidal crystals was proposed using Ewald construction. By utilizing Ewald construction, the problem of determining whether the Bragg-Snell condition is satisfied is replaced with the simpler task of finding lattice points on a sphere.

The results obtained through spectral rendering using the path tracing method show that both the color and pattern inside the opal change when the viewpoint and light source are altered. The results of varying the parameters of the grain size of the silica spheres that constitute the opal are consistent with play of color observed in real opals, demonstrating the plausibility of the diffraction model. Furthermore, by controlling the parameters of the base color, opals with characteristic base colors, such as fire opals and black opals, were successfully represented, showcasing the feasibility of visual simulation for opals in general.

The time required for rendering remains a bottleneck in this research, and designing the appearance of gemstones interactively using the proposed method is challenging. However, the realistic visual simulation results provided by this study may be useful as pre-rendering tools for jewelry design and as aids in the production of synthetic opals. It is hoped that the elements necessary for the visual simulation of opals, the internal structure model, and the diffraction calculation model proposed in this dissertation will be further developed and contribute to the growth of the jewelry industry in the future.

Publications

Main publications

[M1] Soma Yokota, Shumpei Sugita, and Issei Fujishiro, "Modeling of opal using 3D Voronoi tessellation for simulating play of color" (in Japanese), *The Journal of the Institute of Image Electronics Engineers of Japan,* vol. 52, no. 1, pp. 174–182, January 2023. URL : https://www.iieej.org/journal/iieej-vol-52-no-1/

[M2] Soma Yokota and Issei Fujishiro, "Visual simulation of opal using bond percolation through the weighted Voronoi diagram and the Ewald construction," *The Visual Computer,* vol. 40, no. 7 (Special Issue of CG International 2024), pp. 5005–5016, July 2024. DOI: 10.1007/s00371-024-03504-1

Reference publications

[R1] Soma Yokota, Shumpei Sugita, and Issei Fujishiro, "Modeling of opal using 3D Voronoi tessellation for simulating play of color" (in Japanese), in *Proceedings of Media Computing Conference 2022*, pp. S10-3:1–S10-3:6, September 2022, **Young Researcher Award**

[R2] Soma Yokota, Shumpei Sugita, and Issei Fujishiro, "Visual simulation of opal using 3D Voronoi diagram—Reproduction of play of color—" (in Japanese), in *Proceedings of Visual Computing 2022*, pp. 17:1–17:6, October 2022, **CGVI Best Presentation Award, CGVI Student Presetntation Award, Polyphony Digital Award**

[R3] Soma Yokota and Issei Fujishiro, "Modeling of internal structure of opal using 3D additively weighted Voronoi tessellation" (in Japanese), in *Proceedings of Visual Computing Workshop 2022*, presentation number 8, November 2022

[R4] Soma Yokota and Issei Fujishiro, “Visual simulation of opal—Representation of sintering and efficient search of diffracted ray direction—” (in Japanese), in *Proceedings of SIG Technical Reports*, vol. 2023-CG-193, pp. 11:1–11:6, March 2024, **Best Presentation Award, IPSJ Yamashita SIG Research Award**

References

[1] Franz Aurenhammer, “Voronoi diagrams—A survey of a fundamental geometric data structure,” *ACM Computing Surveys*, vol. 23, no. 3, pp. 345–405, September 1991. DOI: 10.1145/116873.116880

[2] Guangyang Bao, Wenyuan Yu, Qianqian Fu, and Jianping Ge, “Low-voltage and wide-tuning-range SiO_2/aniline electrically responsive photonic crystal fabricated by solvent assisted charge separation,” *Journal of Materrials Chemmistry C*, vol. 11, no. 10, pp. 3513–3520, February 2023. DOI: 10.1039/D2TC05499J

[3] Róbert Bán and Gábor Valasek, “Automatic step size relaxation in sphere tracing,” in *Eurographics 2023—Short Papers*, Vahid Babaei and Melina Skouras, Eds., pp. 57–60, May 2023. DOI: 10.2312/egs.20231014

[4] Laurent Belcour and Pascal Barla, “A practical extension to microfacet theory for the modeling of varying iridescence,” *ACM Transactions on Graphics*, vol. 36, no. 4, pp. 65:1–65:14, July 2017. DOI: 10.1145/3072959.3073620

[5] Alexis Benamira and Sumanta Pattanaik, “A combined scattering and diffraction model for elliptical hair rendering,” *Computer Graphics Forum*, vol. 40, no. 4, pp. 163–175, July 2021. DOI: 10.1111/cgf.14349

[6] Pierre Bézier, *Numerical Control: Mathematics and Applications*. London, John Wiley & Sons, Ltd., 1972.

[7] Philippe Blasi, Bertrand Le Saec, and Christophe Schlick, “A rendering algorithm for discrete volume density objects,” *Computer Graphics Forum*, vol. 12, no. 3, pp. 201–210, August 1993. DOI: 10.1111/1467-8659.1230201

[8] James F. Blinn, “Simulation of wrinkled surfaces,” *ACM SIGGRAPH Computer Graphics*, vol. 12, no. 3, pp. 286–292, August 1978. DOI: 10.1145/965139.507101

[9] Simon. R. Broadbent and Jhon. M. Hammersley, “Percolation processes: I. Crystals and mazes,” *Mathematical Proceedings of the Cambridge Philosophical Society*, vol. 53, no. 3, pp. 629–641, 1957. DOI: 10.1017/S0305004100032680

[10] Robert L. Cook, “Stochastic sampling in computer graphics,” *ACM Transactions on Graphics*, vol. 5, no. 1, pp. 51–72, January 1986. DOI: 10.1145/7529.8927

[11] Robert L. Cook, Thomas Porter, and Loren Carpenter, “Distributed ray tracing,” *ACM SIGGRAPH Computer Graphics*, vol. 18, no. 3, pp. 137–145, January 1984. DOI: 10.1145/964965.808590

[12] Tom Cuypers, Tom Haber, Philippe Bekaert, Se Baek Oh, and Ramesh Raskar, “Reflectance model for diffraction,” *ACM Transactions on Graphics*, vol. 31, no. 5, pp. 122:1–122:11, September 2012. DOI: 10.1145/2231816.2231820

[13] Colour Developers, “Colour—Open source colour science Python package,” 2023. URL: https://www.colour-science.org/

[14] Kate Devlin, Alan Chalmers, Alexander Wilkie, and Werner Purgathofer, “Tone reproduction and physically based spectral rendering,” in *Eurographics 2002—STARs*, September 2002. DOI: 10.2312/egst.20021054

[15] Daljit Singh Dhillon, Jeremie Teyssier, Michael Single, Iaroslav Gaponenko, Michel Milinkovitch, and Matthias Zwicker, “Interactive diffraction from biological nanostructures,” in *Eurographics 2014—Posters*, pp. 9–10, 2014. DOI: 10.2312/egp.20141064

[16] Marjolein Dijkstra and Erik Luijten, “From predictive modelling to machine learning and reverse engineering of colloidal self-assembly,” *Nature Materials*, vol. 20, no. 6, pp. 762–773, Jun 2021. DOI: 10.1038/s41563-021-01014-2

[17] Bruce T. Draine, “Scattering by interstellar dust grains. I. Optical and ultraviolet,” *The Astrophysical Journal*, vol. 598, no. 2, pp. 1017–1025, December 2003. DOI: 10.1086/379118

[18] Hugo Duminil-Copin, “Sixty years of percolation,” in *Proceedings of the International Congress of Mathematicians (ICM 2018)*, pp. 2829–2856, 2018.

[19] Paul P. Ewald, “Die berechnung optischer und elektrostatischer gitterpotentiale,” *Annalen der Physik*, vol. 369, no. 3, pp. 253–287, 1921. DOI: 10.1002/andp.19213690304

[20] Luca Fascione, Johannes Hanika, Marcos Fajardo, Per Christensen, Brent Burley, and Brian Green, “Path tracing in production—Part 1: Production renderers,” in *ACM SIGGRAPH 2017 Courses*, ser. SIGGRAPH ’17, pp. 13:1–13:39, July 2017. DOI: 10.1145/3084873.3084904

[21] S.V. Filin, A.I. Puzynin, and V.N. Samoilov, "Some aspects of precious opal synthesis," *The Australian Gemmologist*, vol. 21, no. 7, pp. 278–282, 2002.

[22] Gary Fourneau, Romain Pacanowski, and Pascal Barla, "Interactive exploration of vivid material iridescence based on bragg mirrors," *Computer Graphics Forum*, vol. 43, no. 2, p. e15017, April 2024. DOI: 10.1111/cgf.15017

[23] François Fröhlich, "The opal-CT nanostructure," *Journal of Non-Crystalline Solids*, vol. 533, no. 1, p. 119938, April 2020. DOI: 10.1016/j.jnoncrysol.2020.119938

[24] Jeppe Revall Frisvad, "Importance sampling the Rayleigh phase function," *Journal of the Optical Society of America A*, vol. 28, no. 12, pp. 2436–2441, December 2011. DOI: 10.1364/JOSAA.28.002436

[25] Eloïse Gaillou, Aurélien Delaunay, Benjamin Rondeau, Martine Bouhnik-le-Coz, Emmanuel Fritsch, Guy Cornen, and Christophe Monnier, "The geochemistry of gem opals as evidence of their origin," *Ore Geology Reviews*, vol. 34, no. 1, pp. 113–126, 2008. DOI: 10.1016/j.oregeorev.2007.07.004

[26] Weihong Gao, Muriel Rigout, and Huw Owens, "Facile control of silica nanoparticles using a novel solvent varying method for the fabrication of artificial opal photonic crystals," *Journal of Nanoparticle Research*, vol. 18, no. 12, p. 387, December 2016. DOI: 10.1007/s11051-016-3691-8

[27] Jay S. Gondek, Gary W. Meyer, and Jonathan G. Newman, "Wavelength dependent reflectance functions," in *Proceedings of the 21st Annual Conference on Computer Graphics and Interactive Techniques*, ser. SIGGRAPH '94, pp. 213–220, July 1994. DOI: 10.1145/192161.192202

[28] Cindy M. Goral, Kenneth E. Torrance, Donald P. Greenberg, and Bennett Battaile, "Modeling the interaction of light between diffuse surfaces," *ACM SIGGRAPH Computer Graphics*, vol. 18, no. 3, pp. 213–222, January 1984. DOI: 10.1145/964965.808601

[29] Heribert Graetsch, O.W. Flörke, H. Graetsch, B. Martin, K. Röller, and R. Wirth, "Nomenclature of micro- and non-crystalline silica minerals, based on structure and microstructure," *Neues Jahrbuch für Mineralogie—Abhandlungen*, vol. 163, pp. 19–42, January 1991.

[30] Eduard Gröller, René T. Rau, and Wolfgang Strasser, "Modeling and visualization of knitwear," *IEEE Transactions on Visualization and Computer Graphics*, vol. 1, no. 4, pp. 302–310, 1995. DOI: 10.1109/2945.485617

[31] Ibón Guillén, Julio Marco, Diego Gutierrez, Wenzel Jakob, and Adrian Jarabo, "A general framework for pearlescent materials," *ACM Transactions on Graphics*, vol. 39, no. 6, pp. 253:1–253:15, November 2020. DOI: 10.1145/3414685.3417782

[32] Yu Guo, Adrian Jarabo, and Shuang Zhao, "Beyond Mie theory: Systematic computation of bulk scattering parameters based on microphysical wave optics," *ACM Transactions on Graphics*, vol. 40, no. 6, pp. 285:1–285:12, December 2021. DOI: 10.1145/3478513.3480543

[33] Stephane Guy and Cyril Soler, "Graphics gems revisited: Fast and physically-based rendering of gemstones," *ACM Transactions on Graphics*, vol. 23, no. 3, pp. 231–238, August 2004. DOI: 10.1145/1015706.1015708

[34] Xiao D. He, Kenneth E. Torrance, François X. Sillion, and Donald P. Greenberg, "A comprehensive physical model for light reflection," in *Proceedings of the 18th Annual Conference on Computer Graphics and Interactive Techniques*, ser. SIGGRAPH '91, pp. 175–186, July 1991. DOI: 10.1145/122718.122738

[35] Luis G. Henyey and Jesse L. Greenstein, "Diffuse radiation in the galaxy," *The Astrophysical Journal*, vol. 93, pp. 70–83, January 1941. DOI: 10.1086/144246

[36] Nicolas Holzschuch and Romain Pacanowski, "A two-scale microfacet reflectance model combining reflection and diffraction," *ACM Transactions on Graphics*, vol. 36, no. 4, pp. 66:1–66:12, July 2017. DOI: 10.1145/3072959.3073621

[37] Weizhen Huang, Sebastian Merzbach, Clara Callenberg, Doekele Stavenga, and Matthias Hullin, "Rendering iridescent rock dove neck feathers," in *ACM SIGGRAPH 2022 Conference Proceedings*, ser. SIGGRAPH '22, pp. 43:1–43:8, July 2022. DOI: 10.1145/3528233.3530749

[38] K. C. Hui, A. H. C. Lee, and Y. H. Lai, "Accelerating refractive rendering of transparent objects," *Computer Graphics Forum*, vol. 26, no. 1, pp. 24–33, March 2007. DOI: 10.1111/j.1467-8659.2007.00936.x

[39] Isabelle Icart and Didier Arqués, "An illumination model for a system of isotropic substrate- isotropic thin film with identical rough boundaries," in *Eurographics Workshop on Rendering*, pp. 261–272, June 1999. DOI: 10.2312/EGWR/EGWR99/261-272

[40] Masataka Imura, Takaaki Abe, Ichiroh Kanaya, Yoshihiro Yasumuro, Yoshitsugu Manabe, and Kunihiro Chihara, "Rendering of 'play of color' using stratified model based on amorphous structure of opal," in *Proceedings of the Seventh International Conference on Digital Image Computing: Techniques and Applications, DICTA 2003*, pp. 349–358, January 2003.

[41] Wenzel Jakob, Adam Arbree, Jonathan T. Moon, Kavita Bala, and Steve Marschner, "A radiative transfer framework for rendering materials with anisotropic structure," *ACM Transactions on Graphics*, vol. 29, no. 4, July 2010. DOI: 10.1145/1778765.1778790

[42] Wenzel Jakob and Johannes Hanika, "A low-dimensional function space for efficient spectral upsampling," *Computer Graphics Forum*, vol. 38, no. 2, pp. 147–155, January 2019. DOI: 10.1111/cgf.13626

[43] Johannes Jendersie and Eugene d'Eon, "An approximate Mie scattering function for fog and cloud rendering," in *SIGGRAPH 2023 Talks*, August 2023. DOI: 10.1145/3587421.3595409

[44] Henrik Wann Jensen, "Global illumination using photon maps," in *Rendering Techniques '96*, pp. 21–30, June 1996. DOI: 10.1007/978-3-7091-7484-5_3

[45] ——, *Realistic Image Synthesis Using Photon Mapping*. Natick, MA, USA, A. K. Peters, Ltd., 2001.

[46] J. B. Jones, Jhon V. Sanders, and E. R. Segnit, "Structure of opal," *Nature*, vol. 204, no. 4962, pp. 990–991, December 1964. DOI: 10.1038/204990a0

[47] J. B. Jones and E. R. Segnit, "The nature of opal I. Nomenclature and constituent phases," *Journal of the Geological Society of Australia*, vol. 18, no. 1, pp. 57–68, 1971. DOI: 10.1080/00167617108728743

[48] James T. Kajiya, "The rendering equation," *ACM SIGGRAPH Computer Graphics*, vol. 20, no. 4, pp. 143–150, August 1986. DOI: 10.1145/15886.15902

[49] Benjamin Keinert, Henry Schäfer, Johann Korndörfer, Urs Ganse, and Marc Stamminger, "Enhanced sphere tracing," in *Smart Tools and Apps for Graphics—Eurographics Italian Chapter Conference*, Andrea Giachetti, Ed., 2014. DOI: 10.2312/stag.20141233

[50] Bernhard Kerbl, Georgios Kopanas, Thomas Leimkuehler, and George Drettakis, "3D Gaussian splatting for real-time radiance field rendering," *ACM Transactions on Graphics*, vol. 42, no. 4, pp. 139:1–139:14, July 2023. DOI: 10.1145/3592433

[51] Je-Hyung Kim, Christopher J. K. Richardson, Richard P. Leavitt, and Edo Waks, "Quantum dots in photonic crystals for integrated quantum photonics," in *Active Photonic Platforms IX*, GS Subramania and S Foteinopoulou, Eds., vol. 10345, pp. 1 034 526:1–1 034 526:6, August 2017, Conference on Active Photonic Platforms IX, San Diego, CA, AUG 06-10, 2017. DOI: 10.1117/12.2269172

[52] Charles Kittel, *Introduction to Solid State Physics, 8th Edition*. Hoboken, NJ, USA, John Wiley & Sons, Incorporated, 2004.

[53] Tom Kneiphof, Tim Golla, and Reinhard Klein, "Real-time image-based lighting of microfacet BRDFs with varying iridescence," *Computer Graphics Forum*, vol. 38, no. 4, pp. 77–85, July 2019. DOI: 10.1111/cgf.13772

[54] Kyocera Corporation, *Kyoto Opal*, February 2011, Accessed on February 12, 2025. URL: https://www.kyocera.co.jp/prdct/kyotoopal/index.html

[55] Fujishiro Lab., *RM: Reality Modeling*, May 2021, Accessed on February 12, 2025. URL: https://fj.ics.keio.ac.jp/en/rm-reality-modeling

[56] Seungyeol Lee, Huifang Xu, and Hongwu Xu, "Reexamination of the structure of opal-A: A combined study of synchrotron x-ray diffraction and pair distribution function analysis," *American Mineralogist*, vol. 107, no. 7, pp. 1353–1360, July 2022. DOI: 10.2138/am-2022-8017

[57] G. D. McOrist and A. Smallwood, "Trace elements in precious and common opals using neutron activation analysis," *Journal of Radioanalytical and Nuclear Chemistry*, vol. 223, no. 1-2, pp. 9–15, September 1997. DOI: 10.1007/BF02223356

[58] Johannes Meng, Marios Papas, Ralf Habel, Carsten Dachsbacher, Steve Marschner, Markus Gross, and Wojciech Jarosz, "Multi-scale modeling and rendering of granular materials," *ACM Transactions on Graphics*, vol. 34, no. 4, pp. 49:1–49:13, July 2015. DOI: 10.1145/2766949

[59] Johannes Meng, Florian Simon, Johannes Hanika, and Carsten Dachsbacher, "Physically meaningful rendering using tristimulus colours," *Computer Graphics Forum*, vol. 34, no. 4, pp. 31–40, July 2015. DOI: 10.1111/cgf.12676

[60] Ben Mildenhall, Pratul P. Srinivasan, Matthew Tancik, Jonathan T. Barron, Ravi Ramamoorthi, and Ren Ng, "NeRF: Representing scenes as neural radiance fields for view synthesis," March 2020. URL: https://arxiv.org/abs/2003.08934

[61] Guy M. Morton, "A computer oriented geodetic data base and a new technique in file sequencing," International Business Machines Co., Tech. Rep., 1966.

[62] Thomas Müller, Markus Gross, and Jan Novák, "Practical path guiding for efficient light-transport simulation," *Computer Graphics Forum (Proceedings of EGSR)*, vol. 36, no. 4, pp. 91–100, June 2017. DOI: 10.1111/cgf.13227

[63] Thomas Müller, Marios Papas, Markus Gross, Wojciech Jarosz, and Jan Novák, "Efficient rendering of heterogeneous polydisperse granular media," *ACM Transactions on Graphics*, vol. 35, no. 6, pp. 168:1–168:14, dec 2016. DOI: 10.1145/2980179.2982429

[64] Noriko Nagata, Toshimasa Dobashi, Yoshitsugu Manabe, Teruo Usami, and Seiji Inokuchi, "Modeling and visualization for a pearl-quality evaluation simulator," *IEEE Transactions on Visualization and Computer Graphics*, vol. 3, no. 4, pp. 307–315, October 1997. DOI: 10.1109/2945.646234

[65] F. E. Nicodemus, J. C. Richmond, J. J. Hsia, I. W. Ginsberg, and T. Limperis, *Geometrical considerations and nomenclature for reflectance*. Boston, MA, USA, Jones and Bartlett Publishers, Inc., 1992, pp. 94–145.

[66] Tomoyuki Nishita and Eihachiro Nakamae, "Continuous tone representation of three-dimensional objects taking account of shadows and interreflection," *ACM SIGGRAPH Computer Graphics*, vol. 19, no. 3, pp. 23–30, July 1985. URL: https://doi.org/10.1145/325165.325169. DOI: 10.1145/325165.325169

[67] Hisanari Otsu, Masafumi Yamamoto, and Toshiya Hachisuka, "Reproducing spectral reflectances from tristimulus colours," *Computer Graphics Forum*, vol. 37, no. 6, pp. 370–381, March 2018. DOI: 10.1111/cgf.13332

[68] Ken Perlin, "Improving noise," *ACM Transactions on Graphics*, vol. 21, no. 3, pp. 681–682, July 2002. URL: https://doi.org/10.1145/566654.566636. DOI: 10.1145/566654.566636

[69] Matt Pharr, Wenzel Jakob, and Greg Humphreys, *Physically Based Rendering: From Theory to Implementation*, 3rd ed. San Francisco, CA, USA, Morgan Kaufmann Publishers Inc., 2016.

[70] Alberto Pimpinelli, Levent Tumbek, and Adolf Winkler, "Scaling and exponent equalities in island nucleation: Novel results and application to organic films," *The Journal of Physical Chemistry Letters*, vol. 5, no. 6, pp. 995–998, March 2014. DOI: 10.1021/jz500282t

[71] Gregory S. Rohrer, "Grain boundary energy anisotropy: A review," *Journal of Materials Science*, vol. 46, no. 18, pp. 5881–5895, September 2011. DOI: 10.1007/s10853-011-5677-3

[72] Guodong Rong and Tiow-Seng Tan, "Jump flooding in GPU with applications to Voronoi diagram and distance transform," in *Proceedings of the 2006 Symposium on Interactive 3D Graphics and Games*, ser. I3D '06, pp. 109–116, 2006. DOI: 10.1145/1111411.1111431

[73] Mirko Sattler, Ralf Sarlette, and Reinhard Klein, "Efficient and realistic visualization of cloth," in *Proceedings of the 14th Eurographics Workshop on Rendering*, pp. 167–177, June 2003. DOI: 10.2312/EGWR/EGWR03/167-177

[74] Ken Shoemake, "III.6–Uniform random rotations," in *Graphics Gems III (IBM Version)*, DAVID KIRK, Ed. San Francisco, CA, USA, Morgan Kaufmann Publishers Inc., 1992, pp. 124–132.

[75] Martina Simoni, Franca Caucia, Ilaria Adamo, and Pietro Galinetto, "New occurrence of fire opal from Bemia, Madagascar," *Gems & Gemology*, vol. 46, no. 2, pp. 114–121, 2010. DOI: 10.5741/GEMS.46.2.114

[76] Brian Smits, "An RGB-to-spectrum conversion for reflectances," *Journal of Graphics Tools*, vol. 4, no. 4, pp. 11–22, December 1999. DOI: 10.1080/10867651.1999.10487511

[77] Brian E. Smits and Gary W. Meyer, *Newton's Colors: Simulating Interference Phenomena in Realistic Image Synthesis*. Berlin, Heidelberg, Springer Berlin Heidelberg, 1992, pp. 185–194.

[78] Romain Soulié, Stéphane Mérillou, Olivier Terraz, and Djamchid Ghazanfarpour, "Modeling and rendering of heterogeneous granular materials: Granite application," *Computer Graphics Forum*, vol. 26, no. 1, pp. 66–79, March 2007. DOI: 10.1111/j.1467-8659.2007.00949.x

[79] Jos Stam, "Diffraction shaders," in *Proceedings of the 26th Annual Conference on Computer Graphics and Interactive Techniques*, ser. SIGGRAPH '99, pp. 101–110, July 1999. DOI: 10.1145/311535.311546

[80] ——, "Stable fluids," in *Proceedings of the 26th Annual Conference on Computer Graphics and Interactive Techniques*, ser. SIGGRAPH '99, pp. 121–128, 1999. DOI: 10.1145/311535.311548

[81] Benjamin J. Sumlin, William R. Heinson, and Rajan K. Chakrabarty, "Retrieving the aerosol complex refractive index using PyMieScatt: A Mie computational package with visualization capabilities," *Journal of Quantitative Spectroscopy and Radiative Transfer*, vol. 205, pp. 127–134, 2018. DOI: 10.1016/j.jqsrt.2017.10.012

[82] Yinlong Sun, "Rendering biological iridescences with RGB-based renderers," *ACM Transactions on Graphics*, vol. 25, no. 1, pp. 100–129, January 2006. DOI: 10.1145/1122501.1122506

[83] Kouichi Tabuchi and Toshiyuki Kawai, "Volumetric modeling and rendering of opal considering absorption coefficient (in japanese)," *Proceedings of The 30th Biomedical Fuzzy Systems Association Annual Conference*, vol. 30, pp. 108–111, 2017. DOI: 10.24466/pacbfsa.30.0_108

[84] Spencer W. Thomas, "Dispersive refraction in ray tracing," *The Visual Computer*, vol. 2, pp. 3–8, January 1986. DOI: 10.1007/BF01890982

[85] Antoine Toisoul and Abhijeet Ghosh, "Practical acquisition and rendering of diffraction effects in surface reflectance," *ACM Transactions on Graphics*, vol. 36, no. 5, pp. 166:1–166:16, July 2017. DOI: 10.1145/3012001

[86] K. E. Torrance and E. M. Sparrow, "Theory for off-specular reflection from roughened surfaces," *Journal of the Optical Society of America*, vol. 57, no. 9, pp. 1105–1114, September 1967. DOI: 10.1364/JOSA.57.001105

[87] Eric Veach and Leonidas J. Guibas, "Metropolis light transport," in *Proceedings of the 24th Annual Conference on Computer Graphics and Interactive Techniques*, ser. SIGGRAPH '97, pp. 65–76, 1997. DOI: 10.1145/258734.258775

[88] Alastair J. Walker, "New fast method for generating discrete random numbers with arbitrary frequency distributions," *Electronics Letters*, vol. 10, pp. 127–128, April 1974. DOI: 10.1049/el:19740097

[89] Andrea Weidlich and Alexander Wilkie, "Modeling aventurescent gems with procedural textures," in *Proceedings of the 24th Spring Conference on Computer Graphics*, ser. SCCG '08, pp. 51–58, April 2008. DOI: 10.1145/1921264.1921278

[90] ——, "Realistic rendering of birefringency in uniaxial crystals," *ACM Transactions on Graphics*, vol. 27, no. 1, pp. 6:1–6:12, March 2008. DOI: 10.1145/1330511.1330517

[91] ——, "Rendering the effect of labradoescence," in *Proceedings of Graphics Interface 2009*, ser. GI '09, pp. 79–85, May 2009. DOI: 10.5555/1555880.1555903

[92] Stephen H. Westin, James R. Arvo, and Kenneth E. Torrance, "Predicting reflectance functions from complex surfaces," *ACM SIGGRAPH Computer Graphics*, vol. 26, no. 2, pp. 255–264, July 1992. URL: https://doi.org/10.1145/142920.134075. DOI: 10.1145/142920.134075

[93] Alexander Wilkie, Sunwan Nawaz, Marc Droske, Andrea Weidlich, and Johannes Hanika, "Hero wavelength spectral sampling," *Computer Graphics Forum*, vol. 33, no. 4, pp. 123–131, July 2014. DOI: 10.1111/cgf.12419

[94] Lawrence B. Wolff and David J. Kurlander, "Ray tracing with polarization parameters," *IEEE Computer Graphics and Applications*, vol. 10, no. 6, pp. 44–55, 1990. DOI: 10.1109/38.62695

[95] Andrew Wood, Brendan Mccane, and Scott King, "Ray tracing arbitrary objects on the GPU," *Image and Vision Computing—IVC*, January 2004.

[96] E. R. Woodcock, T. Murphy, P. J. Hemmings, and T. C. Longworth, "Techniques used in the GEM code for monte carlo neutronics calculations in reactors and other systems of complex geometry," in *Proceedings of the Conference on Applications of Computing Methods to Reactor Problems*, pp. 557–579, May 1965.

[97] Fu-kun Wu and Chang-wen Zheng, "A comprehensive geometrical optics application for wave rendering," *Graphical Models*, vol. 75, no. 6, pp. 318–327, November 2013. DOI: 10.1016/j.gmod.2013.07.004

[98] Xuanyu Wu, Kenji Tojo, and Nobuyuki Umetani, "Free-form floor plan design using differentiable Voronoi diagram," in *Pacific Graphics Conference Papers and Posters*, vol. 43, no. 7, August 2024. DOI: 10.2312/pg.20241296

[99] Mengqi (Mandy) Xia, Bruce Walter, and Steve Marschner, "Iridescent water droplets beyond Mie scattering," *Computer Graphics Forum*, vol. 42, no. 4, p. e14893, 2023. DOI: 10.1111/cgf.14893

[100] Shigeki Yokoi, Kosuke Kurashige, and Jun-ichiro Toriwaki, “Rendering gems with aterism or chatoyancy,” *The Visual Computer*, vol. 2, no. 5, pp. 307–312, September 1986. DOI: 10.1007/BF02020431

[101] Greg Zaal and Rob Tuytel, *Poly Haven*, November 2020, Accessed on February 12, 2025. URL: https://polyhaven.com/

[102] Shuang Zhao, Fujun Luan, and Kavita Bala, “Fitting procedural yarn models for realistic cloth rendering,” *ACM Transactions on Graphics*, vol. 35, no. 4, pp. 51:1–51:11, July 2016. DOI: 10.1145/2897824.2925932

Appendix

A.1 Voronoi Diagrams with Various Distances

Voronoi diagrams can be constructed with various characteristics by modifying the definition of distance. In this section, Voronoi diagrams in the Manhattan metric and multiplicatively weighted Voronoi diagrams are introduced. Although these types of Voronoi diagrams are not utilized in this study, they may be applicable in other other procedural modeling contexts.

A.1.1 Voronoi Diagrams in the Manhattan Metric

Voronoi diagram is generated by defining $\delta(\boldsymbol{x}, \boldsymbol{p})$ in **Eq. (4.1)** as the Euclidean distance. This can be replaced by the Manhattan distance $\delta_h(\boldsymbol{x}, \boldsymbol{p})$:

$$\delta_h(\boldsymbol{x}, \boldsymbol{p}) = \sum_{k=1}^{n} |x_k - p_k|,$$

to construct a Voronoi diagram in the Manhattan metric, where $\boldsymbol{x} = (x_1, x_2, ..., x_k)$ and $\boldsymbol{p} = (p_1, p_2, ..., p_k)$. The distance field created by the Manhattan distance and the corresponding Voronoi diagram is shown in **Fig. A.1**.

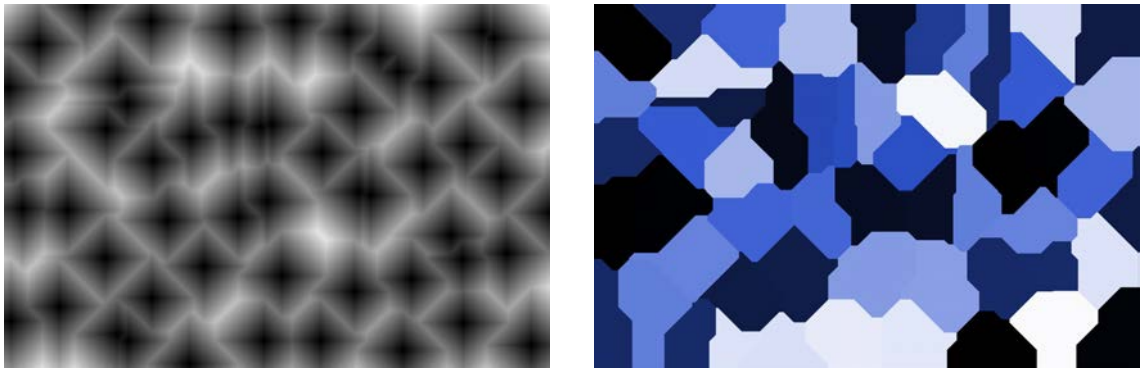

(a) Distance field from sites (b) Voronoi diagram in Manhattan metric

Fig. A.1 Voronoi diagram in the Manhattan metric, which can be drawn by changing the distance function of the Voronoi diagram to the Manhattan distance

A.1.2 Multiplicatively Weighted Voronoi Diagram

The multiplicatively weighted Voronoi diagram is obtained by replacing $\delta(\boldsymbol{x}, \boldsymbol{p})$ in **Eq. (4.1)** with :

$$\delta_m(x, p) = w(p)\delta(x, p),$$

where $w(p)$ represents the weight assigned to each site. **Figure A.2** illustrates the distance field created by applying multiplicative weights and the corresponding Voronoi diagram. **Figure A.3** demonstrates the process of constructing a multiplicatively weighted Voronoi diagram using the wavefront method. Intuitively, the multiplicative weights serve as parameters that control the spreading of the Voronoi regions.

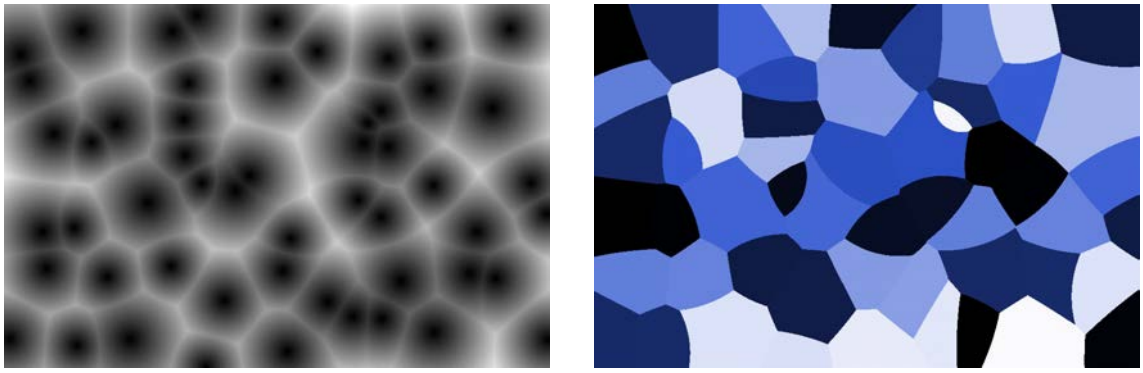

(a) Distance field from sites (b) Multiplicatively weighted Voronoi diagram

Fig. A.2 Visualization of a distance field using multiplicative weighted distance and corresponding 2D Voronoi diagram. For multiplicative weighted Voronoi diagrams, the boundary is known to be represented by a circle

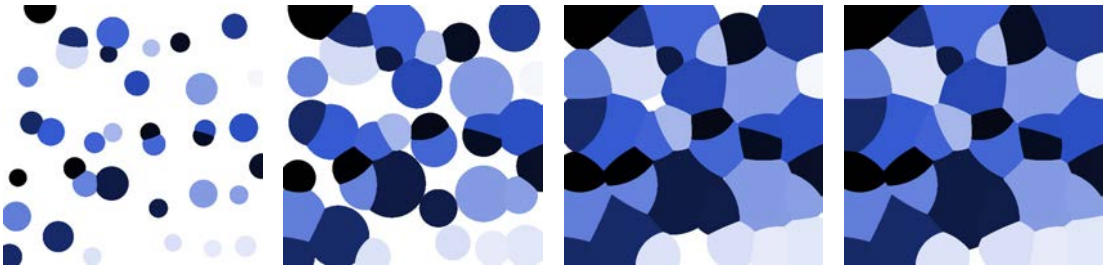

(a) (b) (c) (d)

Fig. A.3 The process of constituting a multiplicatively weighted Voronoi diagram using the wavefront method. Wavefronts are expanded in the order of (a) to (d). With multiplicative weights, all wavefronts begin expanding simultaneously. However, the expansion speed of each wavefront varies with the weight

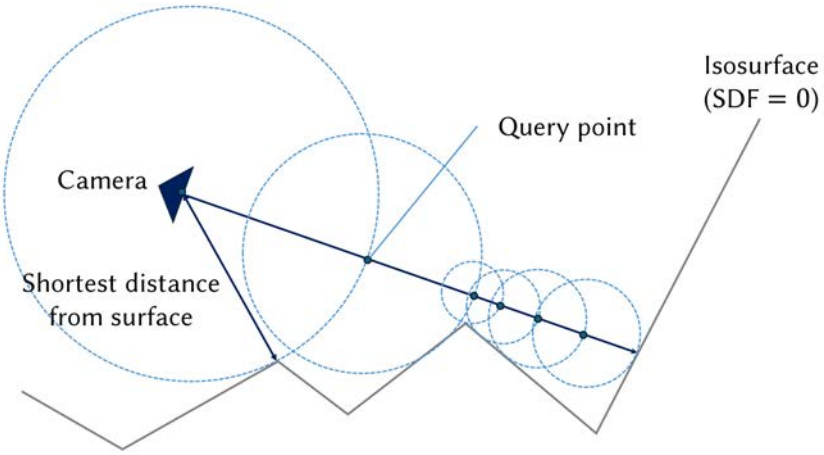

Fig. A.4 The process of reaching an isosurface with Signed Distance Field (SDF) equals zero at the tip of a ray in sphere tracing. The SDF is queried at the location of the ray tip, and the ray is advanced by the distance specified by the SDF value. This operation is repeated, with the length of each ray segment adapting based on the SDF value. As the process continues, the ray tip converges on the surface where the SDF indicates 0

A.2 Sphere Tracing

Ray marching involves decomposing a ray into smaller segments and sampling some function at each point along the ray while ray traversal. For example, NeRF [60] queries an MLP for color and density at each sampled point.

Sphere tracing is a variant of ray marching that uses signed distance field (SDF) to obtain the intersection of a ray with a surface, where SDF value at the surface is 0. The ray is divided into small segments, and the distance at each point is used to adjust the step size for the next ray segment. As the ray progressed, its tip converges to the point where SDF is 0. Compared to methods where rays are advanced by fixed-length steps, sphere tracing allows for more efficient extraction of isosurfaces. A schematic diagram of sphere tracing is shown in **Fig. A.4**. While sphere tracing follows this basic procedure, ongoing researches[49, 3] are focused on improving its accuracy and efficiency.

A.3 The Monte Carlo Integration and Importance Sampling

In Monte Carlo path tracing, the Monte Carlo method is employed to approximate solutions to the rendering equations. For this reason, a brief introduction to the computation of Monte Carlo integrals will be provided. Additionally, focused sampling techniques,

which aims to improve the efficiency of the Monte Carlo integral computation, will be discussed.

A.3.1 The Monte Carlo Method

Let $p_X(x)$ be the probability density function (PDF) of a real-valued random variable X. The expected value of X, denoted $\mathrm{E}[X]$, is given as follows:

$$\mathrm{E}[X] = \int_{-\infty}^{+\infty} x p_X(x) dx,$$

and the valiance $\mathrm{V}[X]$ is obtained as:

$$\mathrm{V}[X] = \mathrm{E}[(X-\mu)^2],$$
$$\mu = \mathrm{E}[X].$$

For any function $f(x)$, the expectation of $f(X)$ is given by:

$$\mathrm{E}[f(X)] = \int_{-\infty}^{+\infty} f(x) p_X(x) dx. \tag{A.1}$$

Using K values $\left\{x^{(1)}, x^{(2)}, ..., x^{(K)}\right\}$ sampled according to $p_X(x)$, the following equation holds:

$$\lim_{K\to\infty} \frac{1}{K} \sum_{k=1}^{K} f(x^{(k)}) = \mathrm{E}[f(X)], \tag{A.2}$$

because using independent identically distributed (i.i.d.) random variables $\{X^{(1)}, X^{(2)}, ..., X^{(K)}\}$, the following equation holds:

$$\begin{aligned} \mathrm{E}\left[\frac{1}{K}\sum_{k=1}^{K} f\left(X^{(k)}\right)\right] &= \frac{1}{K}\sum_{k=1}^{K} \mathrm{E}\left[f\left(X^{(k)}\right)\right] \\ &= \mathrm{E}\left[f(X)\right]. \end{aligned}$$

Additionally, as K approaches ∞, the variance of the sample average converges to zero. Specifically, the variance of the sample average is:

$$\begin{aligned} \mathrm{V}\left[\frac{1}{K}\sum_{k=1}^{K} f\left(X^{(k)}\right)\right] &= \frac{\mathrm{V}\left[\sum_{k=1}^{K} f\left(X^{(k)}\right)\right]}{K^2} \\ &= \frac{\sum_{k=1}^{K} \mathrm{V}\left[f\left(X^{(k)}\right)\right]}{K^2} \\ &= \frac{K\mathrm{V}\left[f(X)\right]}{K^2} \\ &= \frac{\mathrm{E}\left[f^2(X)\right] - \mathrm{E}\left[f(X)\right]^2}{K}. \end{aligned}$$

The variance thus decreases as $1/K$, and the error associated with the approximation of the expectation decreases at a rate of $1/\sqrt{K}$.

As an example, consider the pdf $p_X(x)$ of a uniform random variable over the interval $[a, b)$, given by:

$$p_X(x) = \frac{1}{b-a}, \; x \in [a, b).$$

Using **Eq. (A.1)**, the expected value of a function $f(X)$ can be computed as:

$$\begin{aligned} \mathrm{E}[f(X)] &= \int_{-\infty}^{+\infty} f(x) p_X(x) dx \\ &= \int_a^b f(x) \cdot \frac{1}{b-a} dx. \end{aligned}$$

For specific values of $a = 0$, $b = \pi$, and $f(x) = \sin(x)$, this becomes:

$$\begin{aligned} \mathrm{E}[f(X)] &= \int_0^{\pi} \sin(x) \cdot \frac{1}{\pi - 0} dx \\ &= \frac{2}{\pi} \\ &\simeq 0.6367.... \end{aligned} \tag{A.3}$$

To verify the result, a Monte Carlo integration can be computed, and the value obtained is shown in **Fig. A.5**. The plot illustrates that the Monte Carlo estimate converges to the analytical result given in **Eq. (A.3)**.

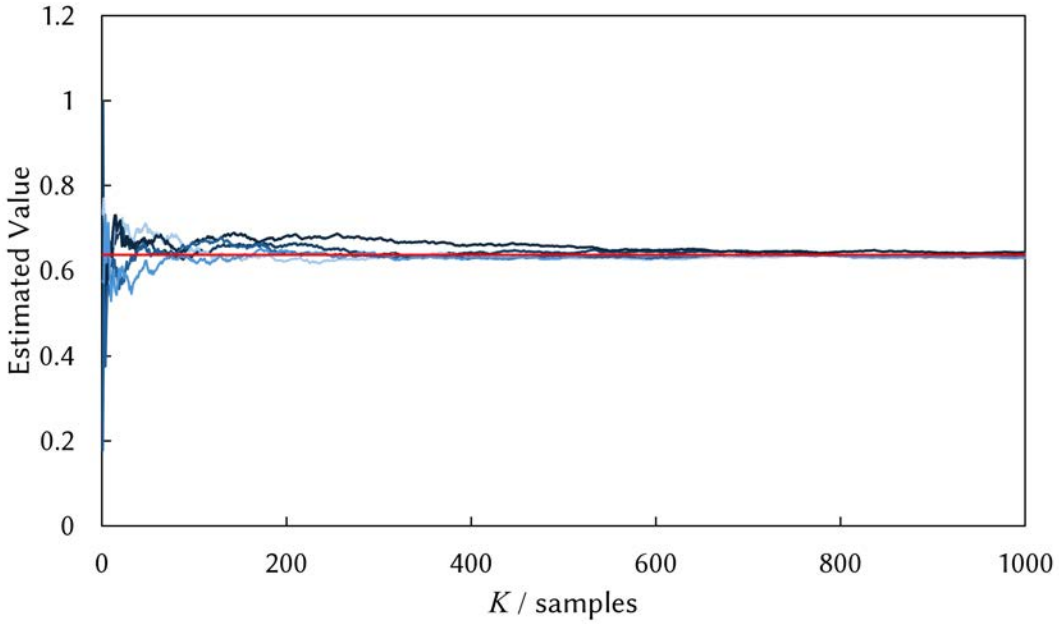

Fig. A.5 Monte Carlo estimation of the expected value using uniform random numbers. The estimates obtained using five random number sequences with distinct seed values are shown in blue, while the expected value is shown in red. As the number of samples K increases, the estimates converge to the expected values

A.3.2 The Monte Carlo Integration

Consider the integral of a function $f(x)$ in the range $a \leq x < b$. Using the pdf $p_X(x)$ defined in this range, and applying **Eqs. (A.1)** and **(A.2)**, the integral can be expressed as:

$$\begin{aligned}\int_a^b f(x)dx &= \int_a^b \frac{f(x)}{p_X(x)} p_X(x)dx \\ &= \mathrm{E}\left[\frac{f(X)}{p_X(x)}\right] \\ &= \lim_{K\to\infty} \frac{1}{K} \sum_{k=1}^{K} \frac{f\left(x^{(k)}\right)}{p_X\left(x^{(k)}\right)}.\end{aligned} \tag{A.4}$$

In this case, it is known that the expected value of $f(X)/p_X(x)$ can be found, provided that $p_X(x) > 0$ for all x where $f(x) > 0$.

As an example, consider the integration of $f(x) = \cos(x)$ over the range $-\pi/2 \leq x < \pi/2$. The exact integral value is 2. The corresponding equation is:

$$\begin{aligned}\int_{-\frac{\pi}{2}}^{\frac{\pi}{2}} \cos(x)dx &= \lim_{K\to\infty} \frac{1}{K} \sum_{k=1}^{K} \cos\left(x^{(k)}\right) \cdot \frac{\frac{\pi}{2} - \left(-\frac{\pi}{2}\right)}{1} \\ &= \lim_{K\to\infty} \frac{\pi}{K} \sum_{k=1}^{K} \cos\left(x^{(k)}\right).\end{aligned}$$

When computed using uniform random numbers from $-\pi/2$ to $\pi/2$, the estimated result converges to 2, as shown in **Fig. A.6**.

A.3.3 Importance Sampling

Using the same technique as described in **Sec. A.3.2**, consider integrating $f(x) = e^x$ over the range $0 \leq x < 3$. The exact integral evaluates to $e^3 - 1 \simeq 19.06$. To achieve efficient convergence of this estimation, note that for $f(x) = e^x$, the contribution to the integral increases as x approaches 3. Therefore, to reduce variance and speed up convergence, it is beneficial to sample regions where the integrand contributes more significantly. This can be achieved by sampling with a pdf $p_X(x)$ that is proportional to $f(x)$, as outlined in **Eq. (A.4)**. This technique, known as importance sampling, aims to sample more densely in regions where the integrand is larger.

Any function can be utilized for importance sampling, provided it satisfies the requirements of a PDF. In CG, particularly in local illumination models such as BRDFs, it is often challenging to construct a pdf that is perfectly proportional to an integrand. As a result, a pdf is commonly designed using a function that allows straightforward application

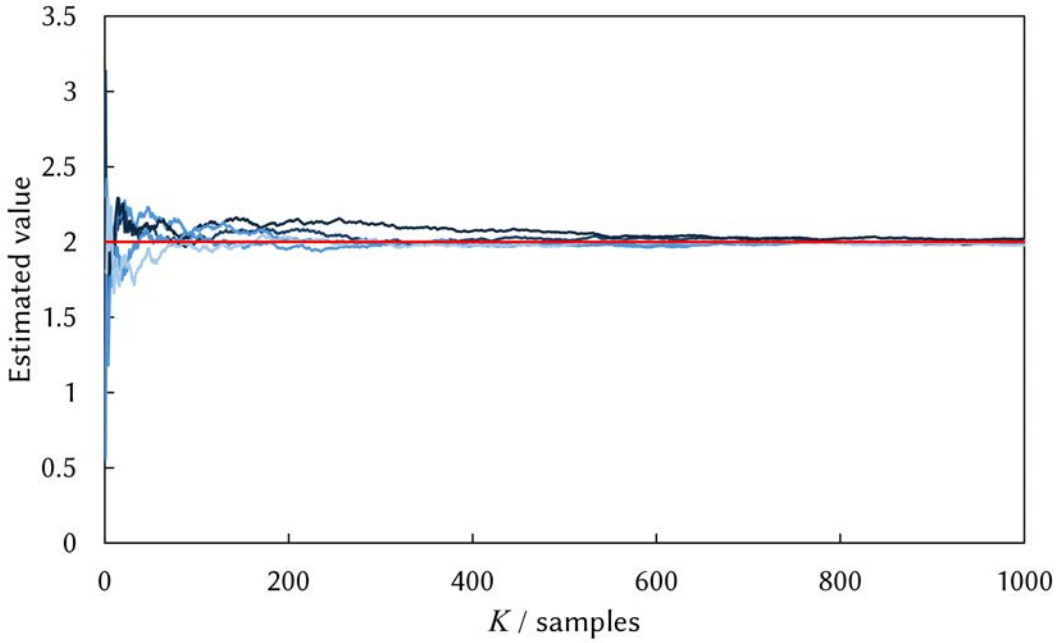

Fig. A.6 The results of performing Monte Carlo integration using uniform random numbers, with estimates obtained from five random number sequences, with different seed values shown in blue and the expected value depicted in red. As the number of samples K increases, the estimates converge to the expected values

of the inverse transform method, as described in the following section. While $f(x) = e^x$ allows for the derivation of an exact proportional pdf, here, a simplified approximation is considered. Specifically, the pdf will be based on the function:

$$f(x) = 2^x,\ 0 \leq x < 3.$$

To perform focused sampling using this pdf, two conditions must be met:

1. $f(x)$ must satisfy the conditions of a valid pdf,
2. $f(x)$ must be possible to sample according to this pdf.

To satisfy the first condition, the integral of the pdf over its domain must equal 1. The pdf $f_X(x)$ can be expressed as

$$f_X(x) = C\,2^x,$$

where C is the normalization factor. The normalization condition requires that:

$$\int_0^3 C\,2^x = 1.$$

The integral is calculated as:

$$C\int_0^3 2^x = C\left[\frac{2^x}{\ln 2}\right]_0^3 = \frac{C}{\ln 2}(8-1) = C\frac{7}{\ln 2}.$$

Solving for C yields:

$$C = \frac{\ln 2}{7}.$$

Thus, the normalized pdf is fully defined:

$$f_X(x) = \frac{\ln 2}{7} 2^x,$$
$$0 \leq x < 3.$$

Next, To make sampling feasible along $f_X(x)$, the inverse transform method is employed. Since pseudorandom numbers generated on a computer are typically uniform random numbers, this method leverages the inverse function of the cumulative distribution function (CDF) to transform a uniformly distributed random variable into one that follows the desired PDF.

First, The CDF $F(x)$ is obtained by integrating the PDF $f_X(x)$ from 0 to x:

$$F(x) = \int_0^x \frac{\ln 2}{7} 2^t \, dt = \frac{2^x - 1}{7},$$
$$0 \leq x < 3.$$

Thus, the inverse function $F^{-1}(x)$ is:

$$F^{-1}(x) = \log_2(7x + 1),$$
$$0 \leq x < 1.$$

Using $F^{-1}(x)$ and a uniform random number $\xi \in [0, 1)$, sampling along $f_X(x)$ can be performed:

$$\int_0^3 2^x dx = \lim_{K \to \infty} \frac{1}{K} \sum_{k=1}^{K} \frac{f\left(F^{-1}(\xi)\right)}{p_X\left(F^{-1}(\xi)\right)}. \tag{A.5}$$

Figure A.7 illustrates the results of focused sampling using **Eq. (A.5)** compared to uniform random number sampling. Even with only 100 samples, importance sampling achieved convergence to the expected value.

A.4 Errors Between RGB and Spectral Rendering with Increasing Number of Bounces

In this experiment, the color changes resulting from an increasing number of bounces in reflection computations were compared between RGB space and spectral space. Using Python's *colour* package [13], five colors were selected from the color checkers available in the package. The selected colors were "Yellow," "Red," "Purplish blue," "Bluish

green," and "Magenta." These colors were sampled at 5 nm intervals within the wavelength range of 380 nm to 780 nm. The spectral distributions of these colors are depicted in **Fig. A.8**.

Each color was multiplied by the number of bounces in both spectral and RGB space. The changes in color were analyzed by comparing two cases: one where the multiplication was calculated in spectral space and the result converted to RGB values through the XYZ color system, and another where the multiplication was performed in RGB space after the initial conversion of the colors to RGB values.

The results of these calculations are shown in **Fig. A.9**. Upon comparison, it was observed that the error for all colors increased as the number of reflections grew. This result suggests that in scenes involving a high number of ray bounces, significant differences can arise between spectral rendering and RGB rendering.

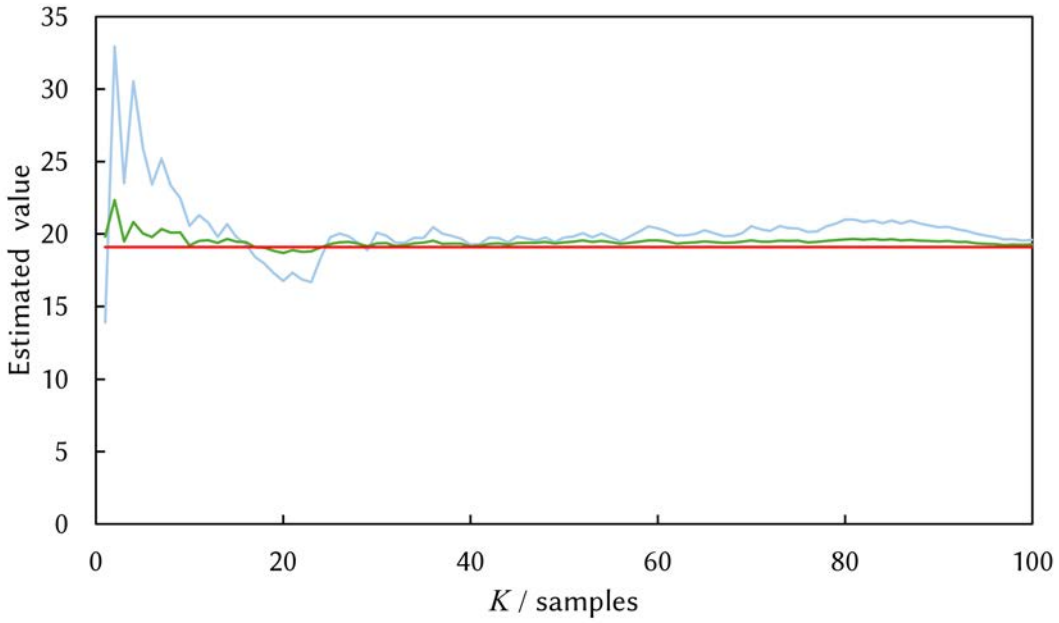

Fig. A.7 Result of Monte Carlo integration with importance sampling. Estimates with importance sampling are shown in yellow-green, estimates with uniform random numbers are shown in light blue, and the expected value is shown in red. The variance is effectively reduced by the focused sampling.

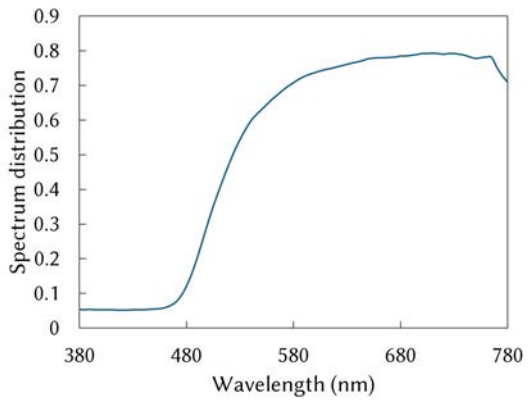

(a) Yellow

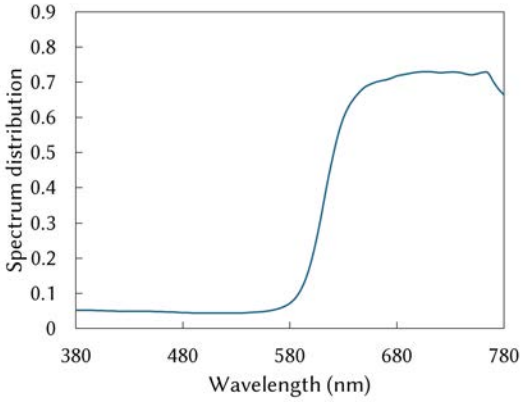

(b) Red

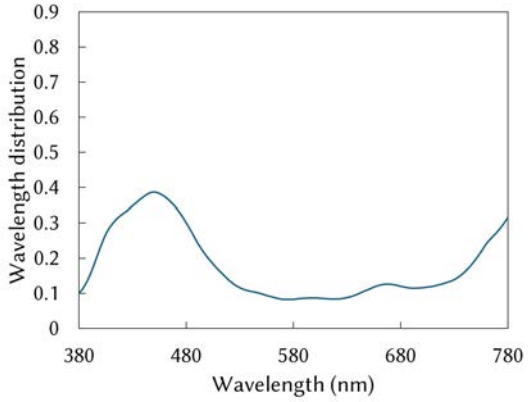

(c) Purplish blue

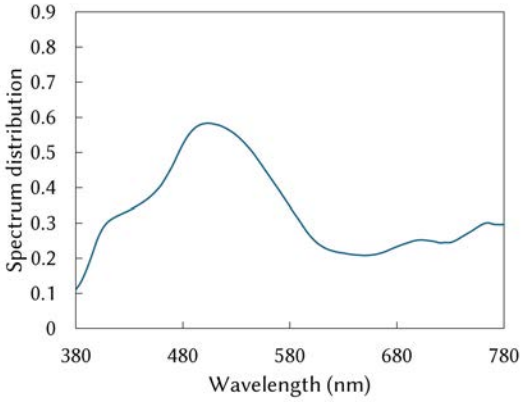

(d) Bluish green

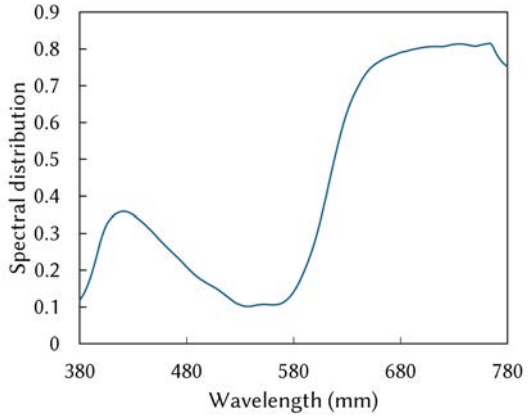

(e) Purplish blue

Fig. A.8 Spectral distribution of each color used in the experiment, obtained from the *Colour* library

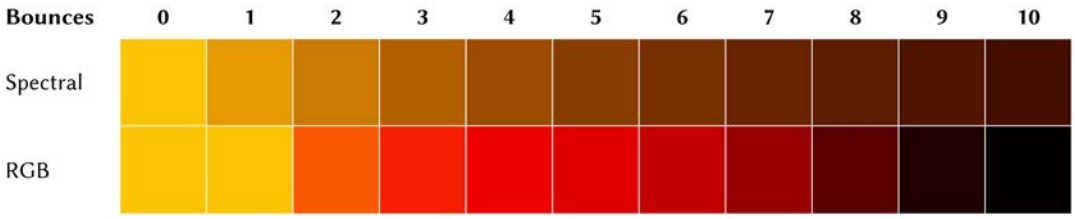

(a) Yellow

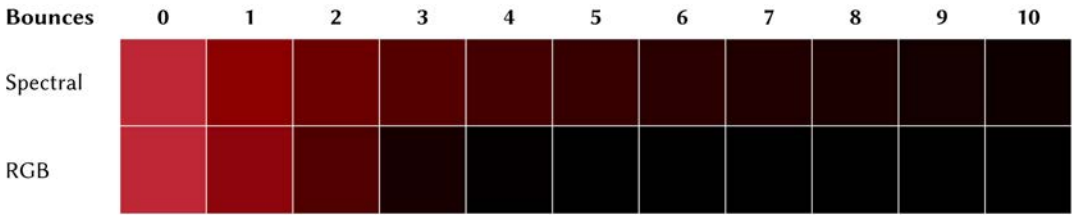

(b) Red

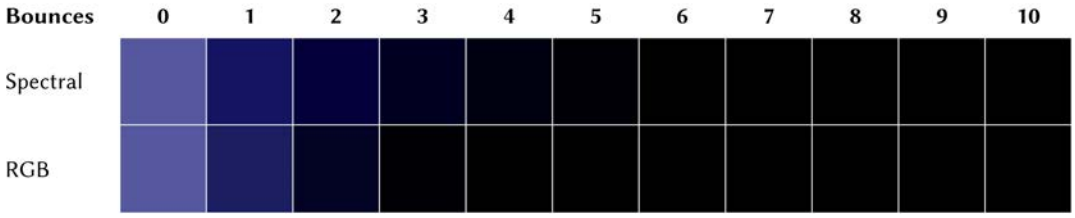

(c) Purplish blue

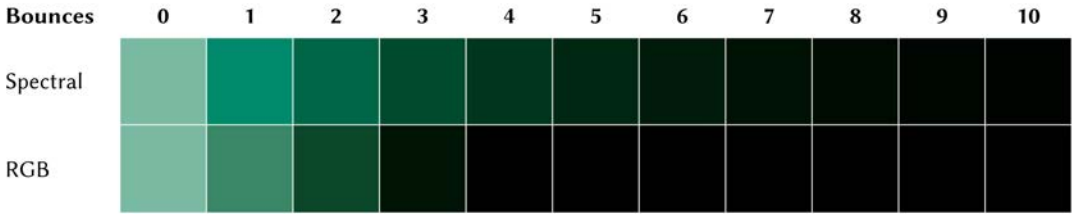

(d) Bluish green

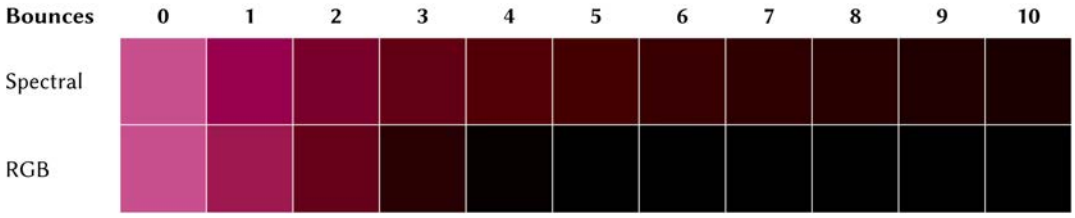

(e) Magenta

Fig. A.9 Results of color multiplication in spectral and RGB space. As the number of multiplications increases, there is an error between the two colors. For scenes with a large number of ray bounces, there can be a significant difference between spectral and RGB rendering results